To the Graduate Council:

I am submitting herewith a dissertation written by James Robert Brewster entitled "Singularities in Wave Fields and their Application to Materials Evaluation." I have examined the final copy of this dissertation for form and content and recommend that it be accepted in partial fulfillment of the requirements for the degree of Doctor of Philosophy, with a major in Materials Science.

K H G. Ashbee

Kenneth H. G. Ashbee, Major Professor

We have read this dissertation
and recommend its acceptance:

D. H. Lowndes

Charlie R. Brooks

Marion L. Hanna

Accepted for the Council:

Vice Provost
and Dean of the Graduate School

Singularities in Wave Fields and their Application to Materials Characterization

A Dissertation

Presented for the

Doctor of Philosophy

Degree

The University of Tennessee, Knoxville

James Robert Brewster

December 1991

DEDICATION

This dissertation is gratefully dedicated to the memory of David William Brewster.

ACKNOWLEDGEMENTS

I wish to thank all those without who my doctorate would not of been possible:

Dr. Ken Ashbee for giving me the opportunity to study in the United States and for encouraging me to follow my personal research goals. Professor J. F. Nye whose crisp intellect is at the origin of my interest on wavefield singularities. Ron Johnson, Mike Rodgers and Doug Fielding for building and maintaining by equipment so well. My fellow graduate students, Zheng Rong (Ron) Xu, Steve and Debora Joslin for acting as sounding boards for my ideas, helping me learn unfamiliar experimental techniques and helping me pass my qualifying exam. All the overworked and underpaid teachers who gave me my 21 years of formal education. Last, but by no means least, my family including Laju S. Khemlani for their constant encouragement and support.

ABSTRACT

Applications of two kinds of wave field singularities, namely, dislocations and caustics, were investigated.

Dislocations are singularities in the phase of a wave and were applied to the characterization, using pulse-echo ultrasound, of surface roughness, metallic microstructure and pitting corrosion.

Caustics exist in the short wavelength limit where the wave field can accurately be described by bundles of rays. Caustics are singular planes in such sets of rays. The application of caustics to ultrasonic imaging, three dimensional microscopy and the measurement of small displacements was investigated.

The ultrasonic experiments were performed in water immersion at a frequency of 20 MHz.

TABLE OF CONTENTS

CHAPTER		PAGE
1.	INTRODUCTION	1
2	DISLOCATIONS	4
3	CAUSTICS	23
4	DISLOCATIONS AND THE MEASUREMENT OF SURFACE ROUGHNESS	30
	Introduction	30
	Experimental Procedure	32
	Results	35
	Mathematical Model	39
	Discussion	43
5	ULTRASONIC DISLOCATIONS AND METALLIC MICROSTRUCTURES	46
	Introduction	46
	Experimental Procedure	48
	Results	51
	Discussion	61

6 ULTRASONIC DISLOCATIONS AND THE GROWTH OF CORROSION PITS 70

Introduction 70

Experimental Procedure 72

Results 75

Analysis 88

Discussion 92

7 CAUSTICS AND ULTRASONIC IMAGING 94

Introduction 94

Experimental Procedure 97

Results 99

Discussion 116

8 THE APPLICATION OF CAUSTICS TO MICROSCOPY 120

Introduction 120

The Inversion Algorithm 127

Discussion 138

9 OPTICAL CAUSTICS AND THE MEASUREMENT OF SMALL DISPLACEMENTS 142

Introduction 142

Experimental Procedure 148

Results 151

Discussion 163

10 CONCLUSION 167

LIST OF REFERENCES 168

APPENDICES 172

APPENDIX A. COMPUTER PROGRAM REFERENCED IN CHAPTER 4 173

APPENDIX B. COMPUTER PROGRAM REFERENCED IN CHAPTER 7 178

APPENDIX C. COMPUTER PROGRAMS REFERENCED IN CHAPTER 7 180

VITA 191

LIST OF FIGURES

Figure		Page
2.1	A phasor	5
2.2	A generic edge dislocation	8
2.3	Phase contours of the diffraction by a conducting half-plane	10
2.4	Cotidal lines in the North Sea	11
2.5	A transducer above an reflecting surface	13
2.6	Comparison between wave forms received from rough and smooth surfaces	14
2.7	Evolution of wave form as a dislocation is traversed	16
2.8	Wave crest map showing dislocation	17
2.9	Wave form superimposed into wave crest map	18
2.10	The first differential of the wave form	19
2.11	A three dimensional wave crest map showing a dislocation	21
3.1	Rays focussed by a perfect and by a real lens	24
3.2	A two dimensional caustic	25
3.3.	The Airy diffraction profile	29
4.1	Schematic diagram of the ultrasonic transducer being scanned above a rough surface	31

4.2 The amplitude profile across the beam of the transducer 36

4.3 The relationship between dislocation density and particle density for various grades of sand paper 37

4.4 Dislocations generated by 120 grade sand paper 38

4.5 Schematic illustration of the mathematical model used 40

4.6 Theoretically predicted dislocation densities 44

5.1 Schematic diagram of an ultrasonic transducer scanning the microstructure of a metal 47

5.2 Brass, before anneal, horizontal plane, x320 53

5.3 Brass, before anneal, vertical plane, x320 54

5.4 Brass, after anneal, horizontal plane, x320 55

5.5 Brass, after anneal, vertical plane, x320 56

5.6 Steel, before anneal, horizontal plane, x160 57

5.7 Steel, before anneal, vertical plane, x160 58

5.8 Steel, after anneal, horizontal plane, x80 59

5.9 Steel, after anneal, vertical plane, x80 60

5.10 The relationship between grain size and dislocation density 62

5.11 The dislocation density above the "as received" aluminum as a function of time of anneal 63

5.12 The dislocation anisotropy above the "as received" aluminum as a function of time of anneal 64

5.13 The dislocation density above the rolled aluminum as a function of time of anneal 65

5.14 The dislocation anisotropy above the rolled aluminum as a function of time of anneal 66

6.1 Schematic diagram of the experimental arrangement 71

6.2 The evolution of nine loop diameters when placed in solution A 76

6.3 The relationship between loop diameter and time of flight 77

6.4 The variation of the average time of flight with time..... 78

6.5 The evolution of the average loop diameter when placed in solution A 79

6.6 The evolution of the average loop diameter when placed in solution B 80

6.7 The evolution of the loop diameter when placed in solution C 82

6.8 The loop growth rate as a function of concentration 83

6.9 The relationship between the loop diameter and the distance from the sample, measured for several different pits 84

6.10 The relationship between loop diameter and pit diameter 85

6.11 The relationship between loop diameter and pit depth 86

6.12. The relative changes in pit dimensions after 15 days immersion on solution C 87

7.1 Ray diagram showing the formation of a caustic by reflection from a cylindrical dish 95

7.2 Schematic diagram of the imaging system 96

7.3. Loci of the maxima and half-maxima in the signal from the caustic 101

7.4 The variation in the width of the caustic along its length 102

7.5 The variation of the peak signal amplitude along the length of the caustic 103

7.6 The amplitude profile across the caustic 104

7.7 The time of flight as a function of x 106

7.8 Ultrasonic image of object A 108

7.9 Ultrasonic image of object A from a perpendicular elevation 109

7.10 Object A 110

7.11 Object A viewed from a perpendicular elevation 111

7.12 Plan view of object A 112

7.13 Ultrasonic image of object B 114

7.14. Object B 115

7.15 Ultrasonic image of object C 117

7.16 Object C 118

8.1 Caustics formed by the transmission of light through a replica of a fracture surface 121

8.2 A vertical ray being reflected by a general surface 123

8.3 A caustic surface being sectioned by the image plane of a microscope 126

8.4 The surface used to test the inversion algorithm 131

8.5 Sections through the caustic surface 132

8.6 Sections through the caustic surface 133

8.7 The accuracy of the rays as a function of the goodness of fit 135

8.8 The accuracy of the rays as a function of A 136

8.9 The accuracy of the rays as a function of A after the elimination process 137

8.10 The error in the predicted slope as a function of the predicted gradient 139

8.11 The distribution of the points at which the slope has been determined 140

9.1 A ray being reflected from a surface, s(x) 143

9.2 Schematic diagram of the optical system employed 146

9.3 Measurement of the diameter of the caustic by transverse movement of the objective lens of the telescope 150

9.4 A typical section through a caustic 152

9.5 Location of the geometric caustic by extrapolating from the locations of the peaks and troughs of the diffraction pattern 154

9.6 The diameter of the caustic as a function of the applied force 155

9.7 Residual plot 156

9.8 Plot of the residuals expressed in terms of the central displacement 158

9.9 Increasing the precision by introducing an extra member between the load cell and the specimen 159

9.10 Diameter of the caustic as a function of the applied force when using the stiffened system 160

9.11 Residual plot expressed in terms of the central displacement for the stiffened system 161

9.12 Residuals from a parabolic fit to the data 162

9.13 Diameter of the caustic as a function of the applied force when using the 2mm hole 164

9.14 Residual plot expressed in terms of the central displacement for the 2mm hole 165

CHAPTER 1

INTRODUCTION

The aim of this dissertation is to demonstrate applications of singularities in linear waves to materials science and related fields.

In this context, a singularity can be defined as a surface, line or point that possesses properties that distinguish it from the space that surrounds it. An illustration of this definition is the state boundaries that represent singular lines in the United States. Points on them are distinguished from the surrounding land by the fact that they are neither in one state nor the other. Deeper aspects of these structures are also indicated by this example. There are numerous singular points where three states meet, an example of higher order singularities within singularities. There is also one point where four states meet. This is a "non-typical" singularity because it is unstable with respect to small changes in the state boundaries, as opposed to the "typical", and stable, three state points. This property that defines a "typical" singularity is known as "structural stability". Among physicists concerned with the theory of waves, what philosophers term a "paradigm shift" is taking place [KUHN 1962]. This takes the form of a move away from the study of the exact solutions of, relatively simple, special cases towards the realization that waves are geometrical entities whose most important features are their singularities [BERRY 1981]. Although often complex, these structures can be separated from the infinite

number of possible forms by the demands of structural stability. The concept of characterizing a complicated system in terms of singularities is not at all alien to materials scientists; without mention of any of the countless billions of atoms that constitute a piece of metal, one can account for almost all of its properties in terms of crystal dislocations and the boundaries, edges and corners of its grains.

To the more worldly scientist or engineer, the value of wave field singularities lies in the fact that they constitute well-defined entities within an otherwise featureless space. This facilitates the characterization of the wave field and thus the specimen responsible for it. Once found, the wave field could be solved to yield the specific properties of the specimen but, in line with the new paradigm, it is better to attempt to obtain general properties of the specimen from the statistics of the fields singularities. A particularly useful aspect of these singularities is that their position can be precisely determined, allowing sensitive measurement of small changes in the wave field.

The application of two types of singularity namely, dislocations and caustics, will be explored in this thesis. Dislocations, so named because of their morphological similarity to dislocations in crystals, are singularities in the phase of a wave. Here the study of dislocations has been limited to ultrasound because direct measurement of phase is required to detect them. Caustics are singularities in bundles of rays.

After a more detailed exposition of the theory of these two singularities, examples will be presented of how dislocations can be applied to roughness measurement, microstructural characterization and measuring the rate of corrosion pit growth. Experiments evaluating the application of caustics to ultrasonic imaging, microscopy and the measurement of small displacements will also be presented.

CHAPTER 2

DISLOCATIONS

Dislocations are singularities in the phase of a wave, specifically regions of space at which the phase is indeterminate.

In the case of a monochromatic, continuous wave field, an unambiguous definition of phase, and therefore of dislocations is relatively easy to establish. Any such field can be uniquely described by:

$$\Psi(\mathbf{r},t) = \rho(\mathbf{r})\cdot\cos(\omega t+\varphi(\mathbf{r})) \qquad 2.1$$

where $\Psi(\mathbf{r},t)$ is the measured amplitude of the wave and $\rho(\mathbf{r})$ and $\varphi(\mathbf{r})$ are functions of position known as the amplitude and phase respectively. The form of this equation leads one to represent the wave in complex notation:

$$\Psi(\mathbf{r},t) = \mathrm{Re}\{\rho(\mathbf{r})\cdot e^{i(\omega t+\varphi)}\} \qquad 2.2$$

Where $i=\sqrt{-1}$. This implies that the amplitude and phase of the wave at any point in space can be represented by a single point on an Argand diagram known as a phasor (figure 2.1). As the position of the observation point is varied, the phasor will move about the Argand diagram. At certain locations in space the phasor is at the origin and, therefore, the phase angle, φ, is indeterminate. The set of points on which this is true is the dislocation. In order to find the dimensionality of this set, that is the number of parameters

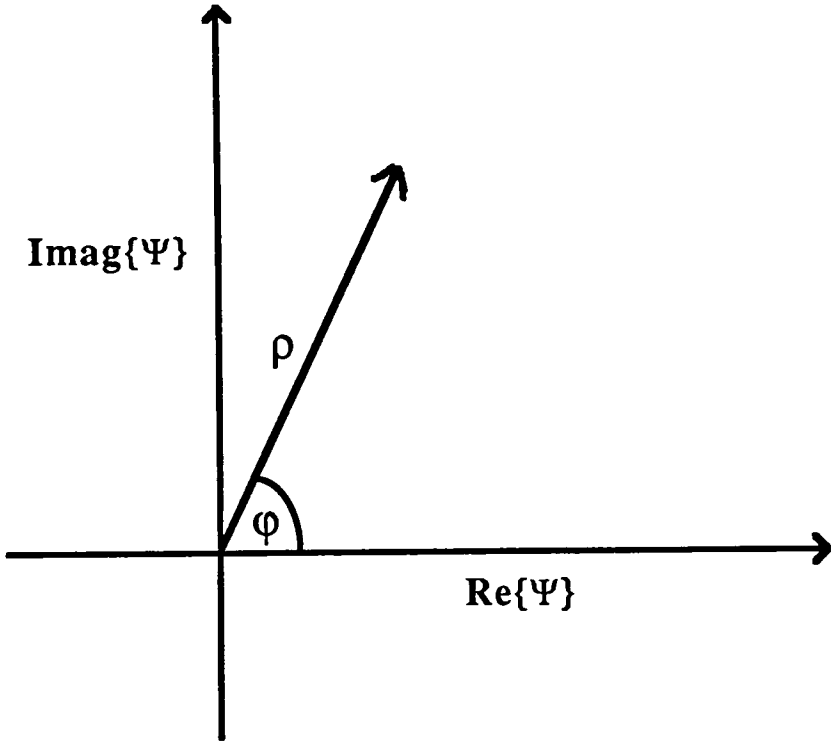


Figure 2.1. A phasor.

required to label points within it, we make use of the fact that at a dislocation:

$$\mathrm{Re}\{\rho(\mathbf{r})\cdot e^{i(\omega t+\varphi)}\} = 0 \qquad 2.3$$

and

$$\mathrm{Im}\{\rho(\mathbf{r})\cdot e^{i(\omega t+\varphi)}\} = 0 \qquad 2.4$$

As the time dependance can be factored out, we have two equations and the three spatial variables. Therefore, there is one variable left and the singularity is a line. As the intensity is zero on these lines they are normally referred to as null lines.

Now one must apply the concept of structural stability as described in the introduction. If one can find a solution to the wave equation that contains a dislocation and show that this feature is structurally stable, then its morphology will be typical of the general wave field. Going back to the previous analogy with state boundaries, if three state points can be shown to be structurally stable, then this feature will be typical of countries divided into provinces in a similar way. The basic theory of wave field dislocations was postulated by Nye and Berry [NYE, BERRY 1974]. They presented a generic pure edge dislocation given by the wave function:

$$\Psi = A\cdot(kx+i\beta\cdot k\cdot\zeta)\cdot e^{ik\zeta} \qquad 2.5$$

$$\zeta = z-ct \qquad 2.6$$

where A and β are real constants and k is the wave number. From this, the phase is given by:

$$\rho(x,t) = k*\zeta+\arctan\{\beta\zeta/x\} \qquad 2.7$$

The ambiguity in the inverse tangent function is removed by requiring that the sine of the angle have the same sign as $\beta k\zeta$. The contours of phase, which are in fact wavefronts, show an indeterminate point at the origin (figure 2.2). This dislocation runs along the y-axis. Away from the origin, the wavefronts become evenly spaced, parallel straight lines, indicating a plane wave travelling in the z-direction. If one inspects the $\rho=0$ contours the analogy with crystallographic dislocations becomes clear. The contours of the plane wave resemble the evenly spaced planes of an undistorted lattice and, just like a plane of atoms ending at a dislocation, the wave front terminates at the y-axis.

By direct analogy with the Burger's vector, the "dislocation strength" of the above singularity is measured to be 2π. It can be shown that dislocations with higher strengths are not structurally stable but disassociate into dislocations of lower order, as if they were crystal dislocations reducing their elastic energy. A similar generic form has been found for the screw dislocation and also, dislocations that move relative to their host wave train, that is, glide. In order to illustrate how dislocations occur in real wave fields, two examples, first presented by Berry are given [BERRY 1981].

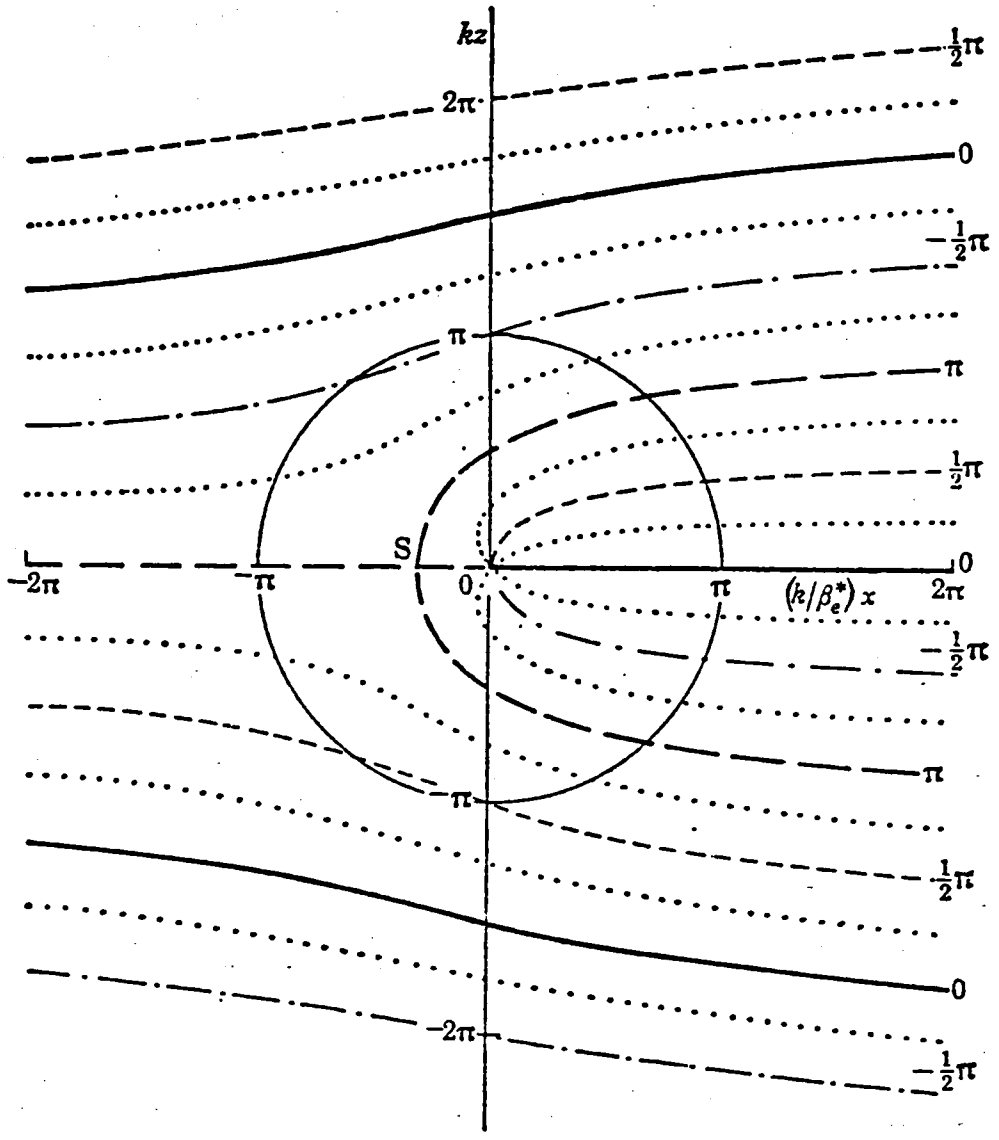


Figure 2.2. A generic edge dislocation.

Figure 2.3 depicts wavefronts calculated from Sommerfield's exact solution of the diffraction of a plane electromagnetic wave by a conducting half plane [BRAUNBEK and LAUKIEN 1952]. Three dislocations are visible. This example serves as a reminder that even though the morphology is structurally stable, the actual appearance of the wavefronts can be distorted from one that resembles that of a dislocation in a crystal. Inspection of figure 2.3 shows that wavefronts discontinuously end at the null points.

A fascinating example of phase contours containing dislocations is found in ocean science. Figure 2.4 depicts cotidal lines in the North Sea, that separates the east coast of Britain from the northern European continent. These lines connect points on which high tide occurs at the same times each day and thus, are the phase contours of a monochromatic wave field. Two dislocation points can be seen on this map. These points where first described in 1836 by Whewell [WHEWELL 1836] and are referred to by oceanographers as "amphidromic points". Each high tide sweeps down from the north with part of the wave turning east around the curve of Scandinavia. The rest of the wave rotates around the more northerly of the two dislocations meeting the eastern branch twelve hours, that is one wave period, later. At the amphidromic points there is no tide.

If one moves away from such monochromatic, steady state wave fields to consider pulses of radiation, the definition of phase becomes more arbitrary and difficult. In their 1974 paper, Nye and

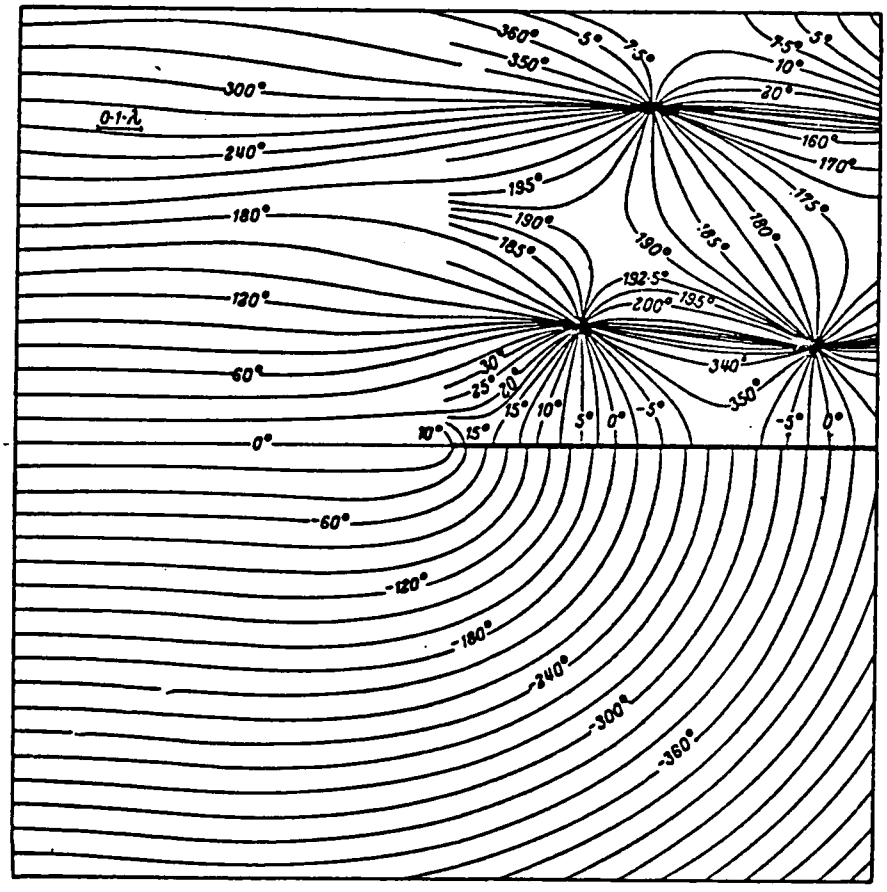


Figure 2.3. Phase contours of the diffraction by a conducting half-plane.

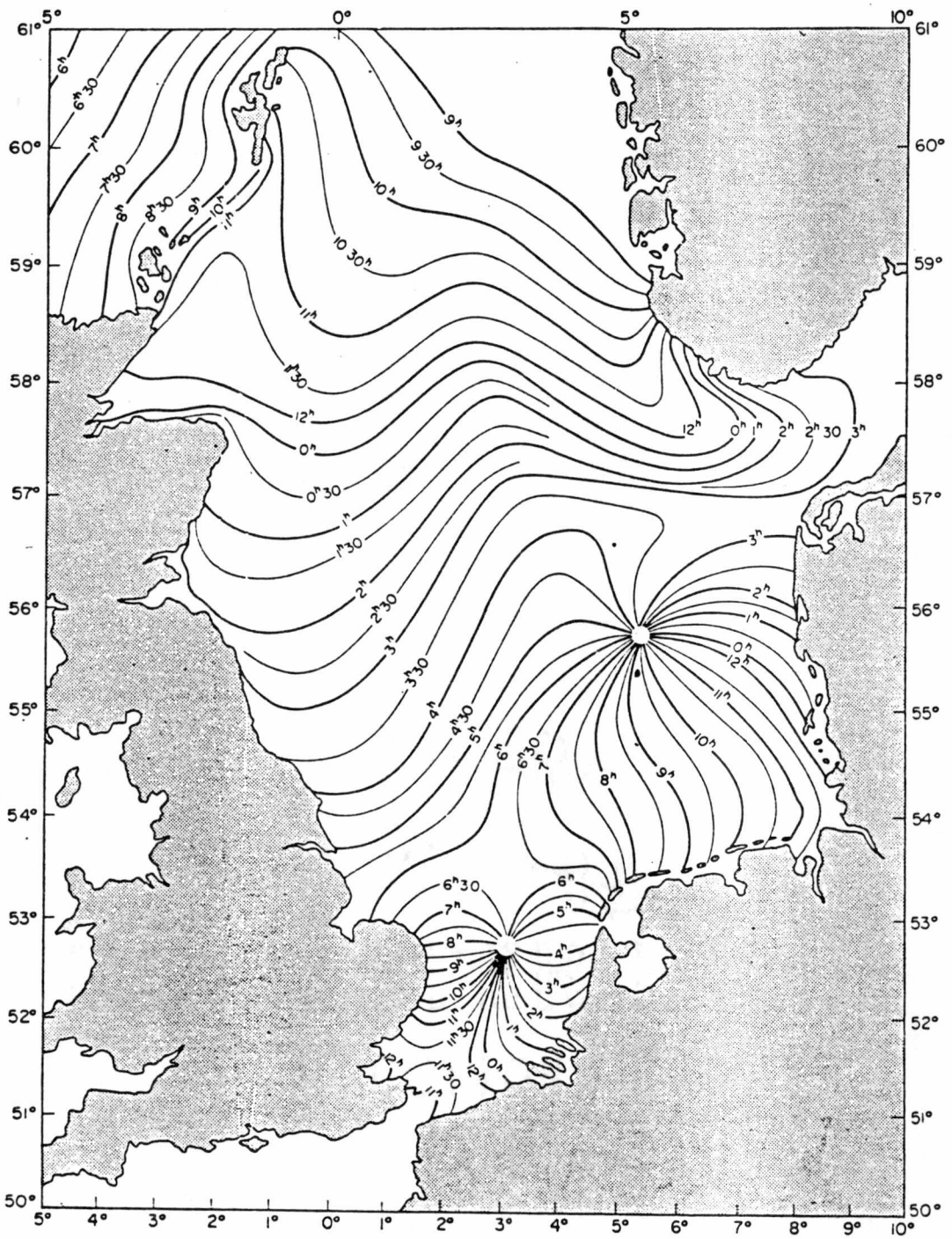


Figure 2.4. Cotidal lines in the North Sea.

Berry considered the "quasi-monochromatic" approach of describing pulses as being waves like those described by equation 2.1 yet modulated by a time dependent envelope function. This approach has been used to model the dislocation loops in the field of an ultrasonic transducer [WRIGHT and BERRY 1984]. In order to facilitate the observation of dislocations in ultrasound on an oscilloscope screen, a different definition of phase will be used here [Wright 1979].

In order to define the location of a dislocation one does not need to know the value of phase at every point. Knowledge of only one phase contour, the wave crest, is necessary. The simplest definition of a wave crest is that it is the locus of points at which the wave amplitude is a maximum at a given instant. A dislocation marks the edge of such a wave crest surface.

Consider a point source of ultrasonic pulses transmitting to an uneven reflecting surface. As is quite a usual feature of ultrasonic equipment, the same transducer detects any reflected sound and the signal is displayed on an oscilloscope. The transducer can be translated about the X-Y plane and its position, P(x,y), measured (figure 2.5). Figure 2.6 shows the basic pulse shape, as would be obtained by recording the signal reflected from a smooth surface. As also illustrated in figure 2.6, the echo from a rough surface is an aggregate of signals, reflected from different points, returning at different times the pulse is longer and more complicated.

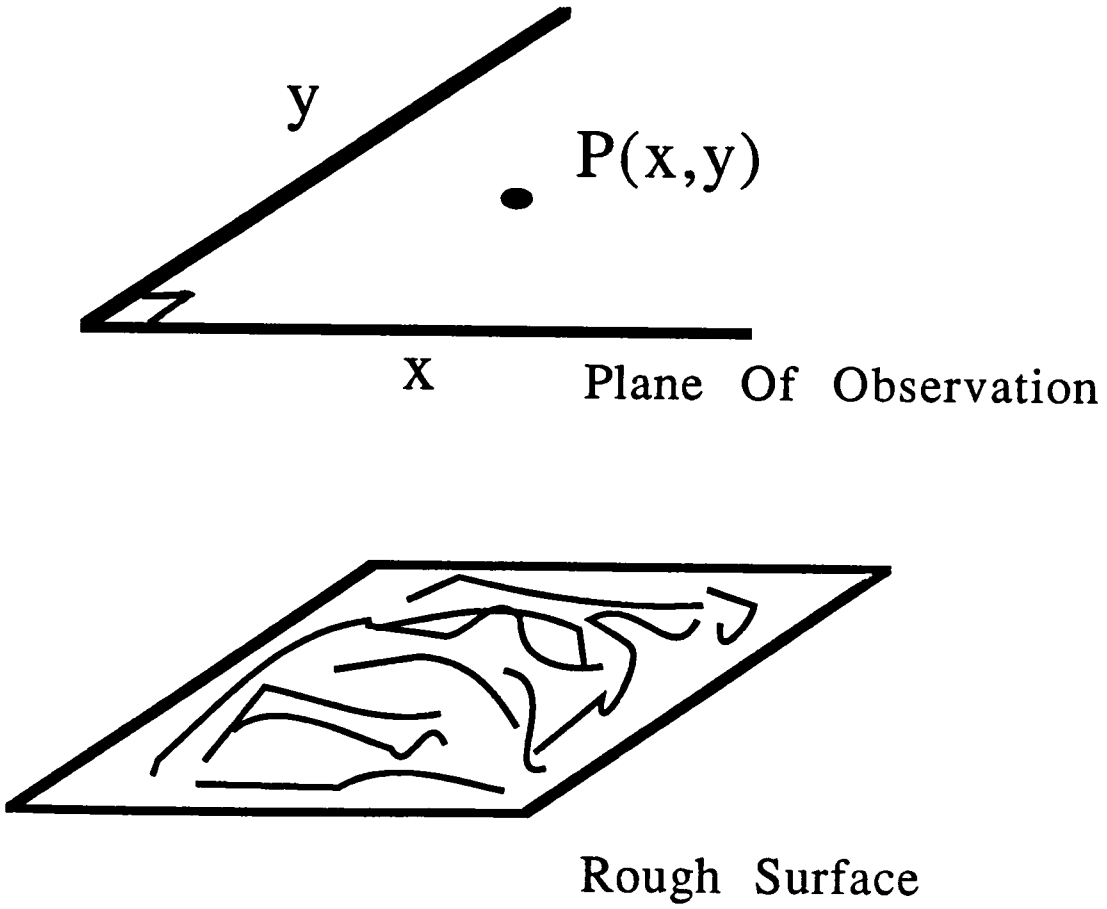


Figure 2.5. A transducer above a reflecting surface.

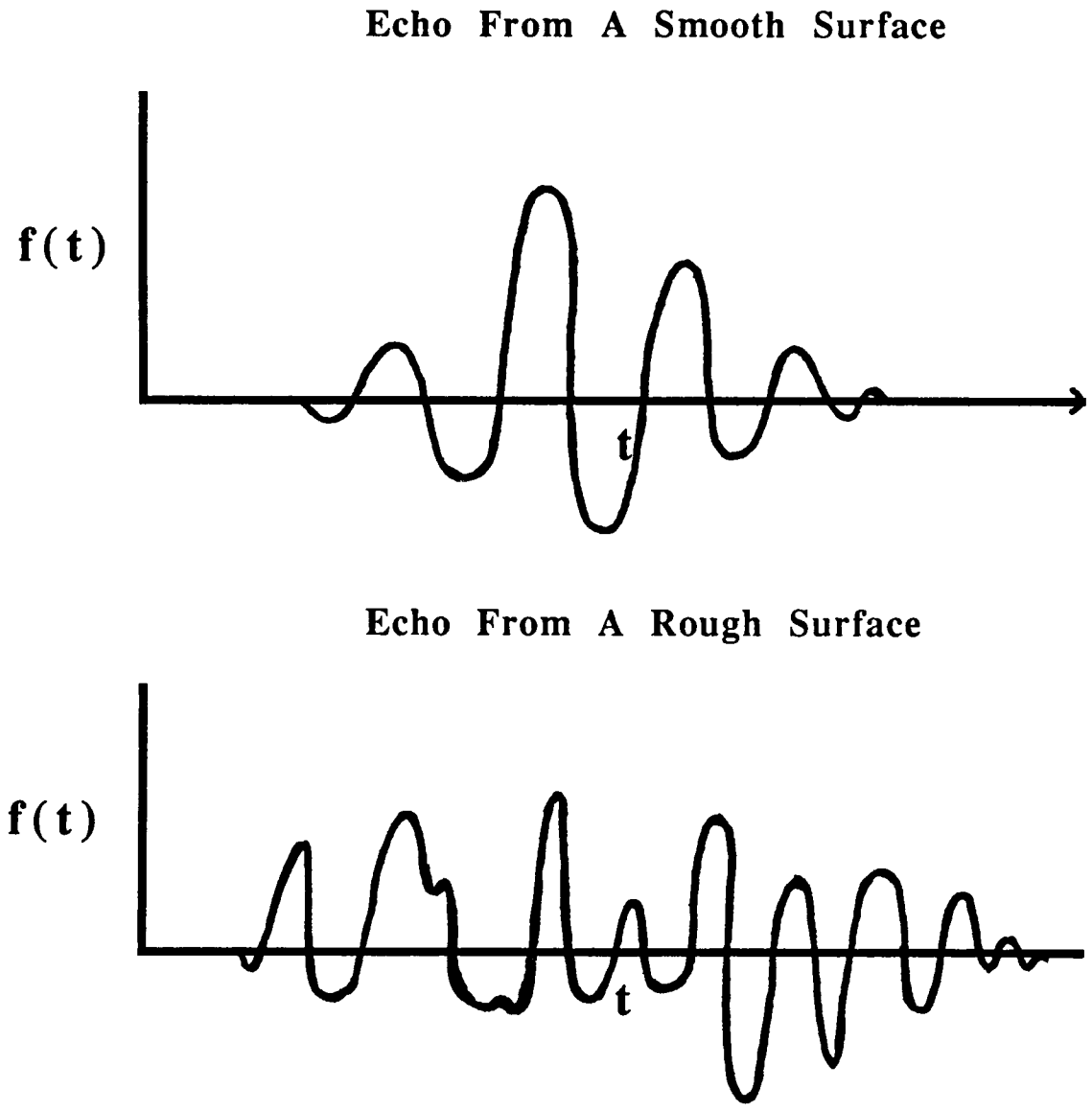


Figure 2.6. Comparison between wave forms received from rough and smooth surfaces.

The transducer is scanned along an arbitrary line, here taken to be the x-axis, and the returning signal, f(t), is recorded as a function of position. Figure 2.7 shows a sequence of such signals that involves the disappearance of a wave crest. In order to relate these signals to the phase contour diagrams presented above, consider a plot of the arrival time of each wave crest, as a function of transducer position, X (figure 2.8). This figure is a two dimensional phase contour diagram with the exception that only one contour level is known. The dislocation point is readily identified as the point, in time and space, (Δ,τ), where the wave crest disappears. The relationship between this dislocation and what is actually observed in practice can be seen by superimposing the oscilloscope trace onto the phase contour diagram at various values of X (figure 2.9).

With this definition of phase, the dislocation can be defined in terms of differentials of f(t). Figure 2.10 illustrates the behavior of the first differential of f(t), $f'(t)$ in the vicinity of (Δ,τ). As the transducer approaches the dislocation, the roots of $f'(t)=0$, that represent a crest and a trough respectively, move closer together. Beyond the dislocation $f'(t)$ has zeros. When the transducer is exactly on the dislocation point, $f'(t)=0$ has two coincident roots which implies that the first and second differentials of f(t) are simultaneously zero. Restating; a dislocation can be defined as the set of points at which there exists a point in time in the signal received at which its first two differentials, with respect to time,

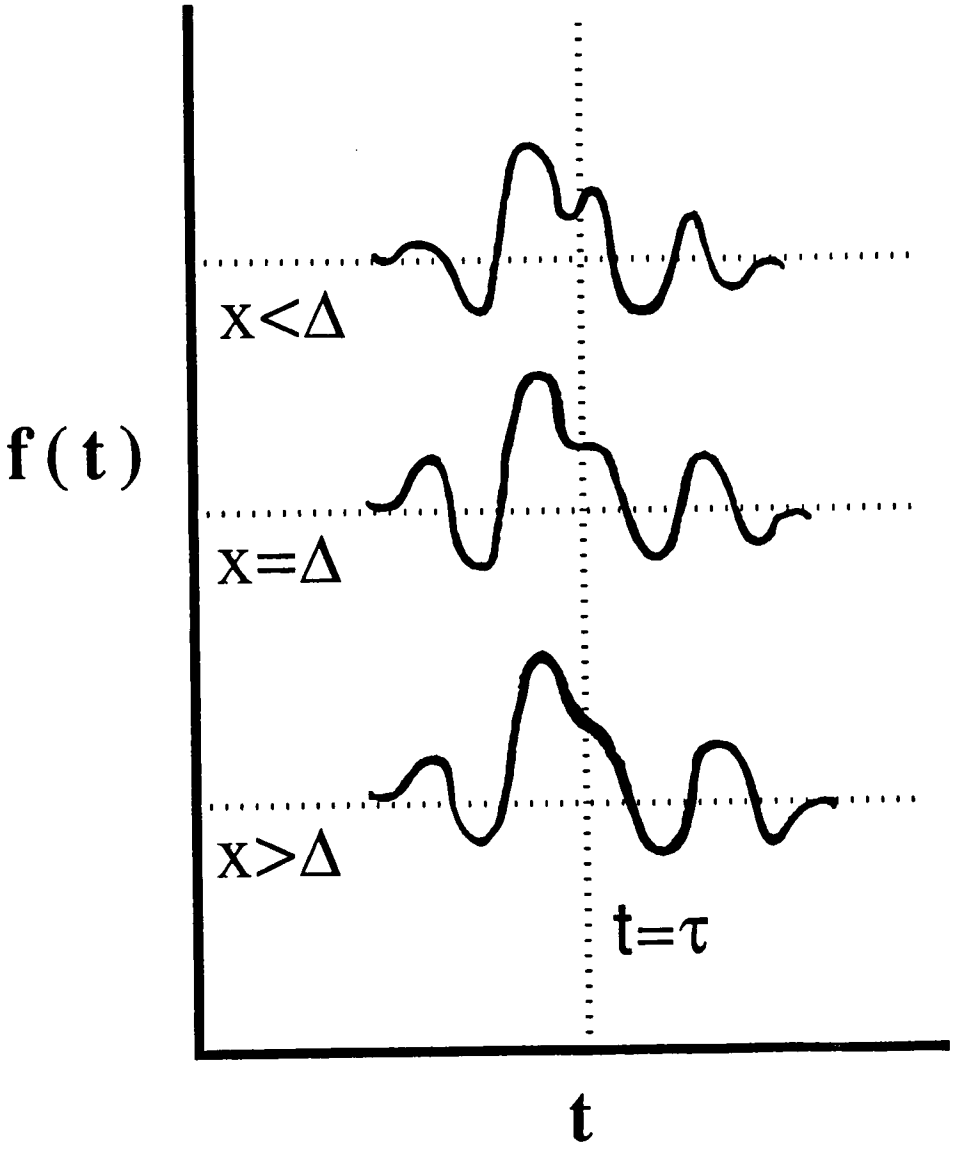


Figure 2.7. Evolution of wave form as a dislocation is traversed.

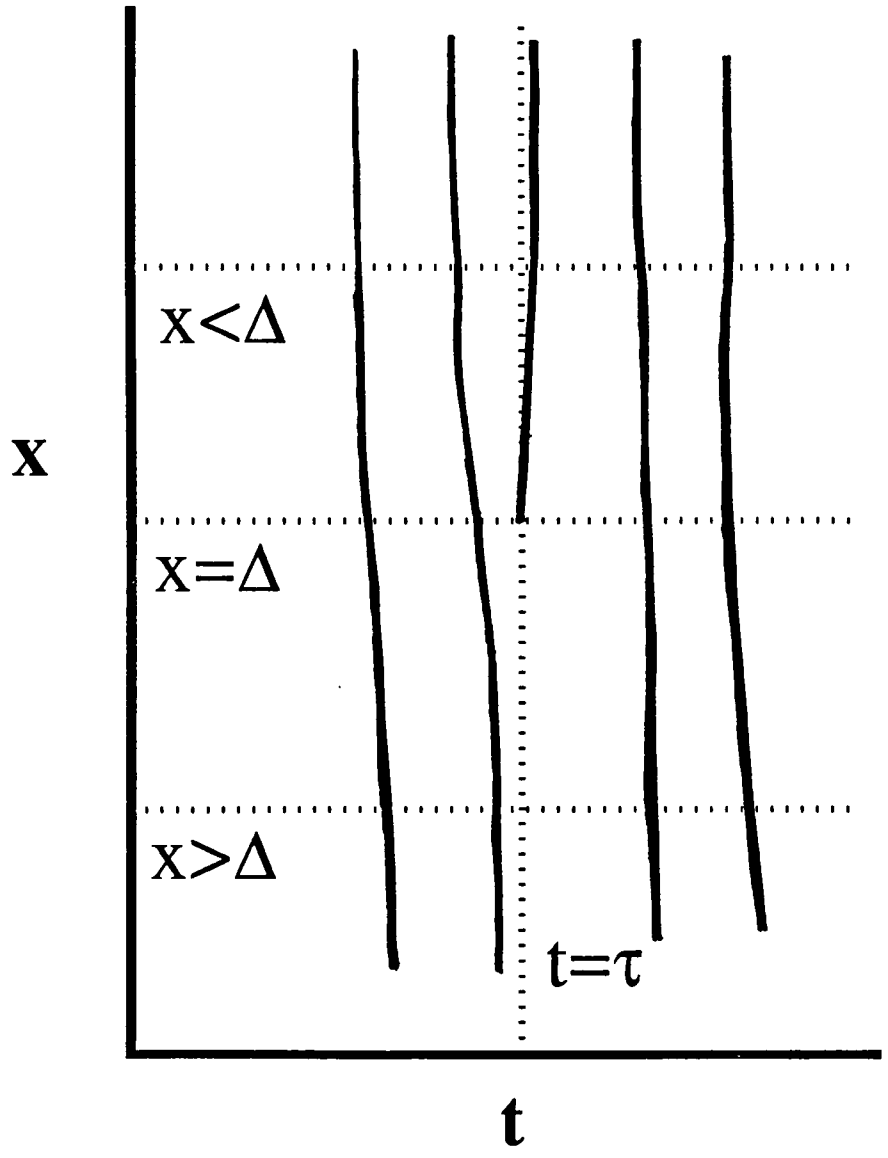


Figure 2.8. Wave crest map showing dislocation.

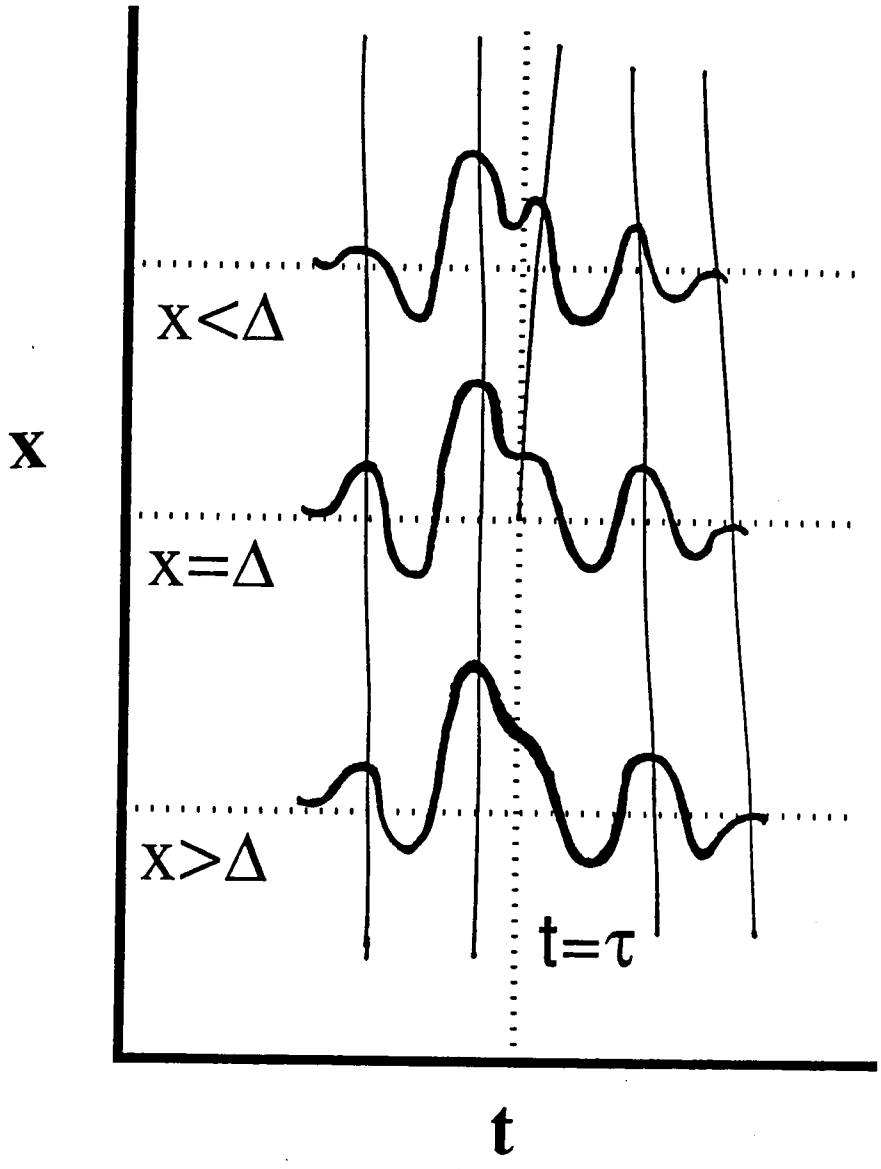


Figure 2.9. Wave form superimposed into wave crest map.

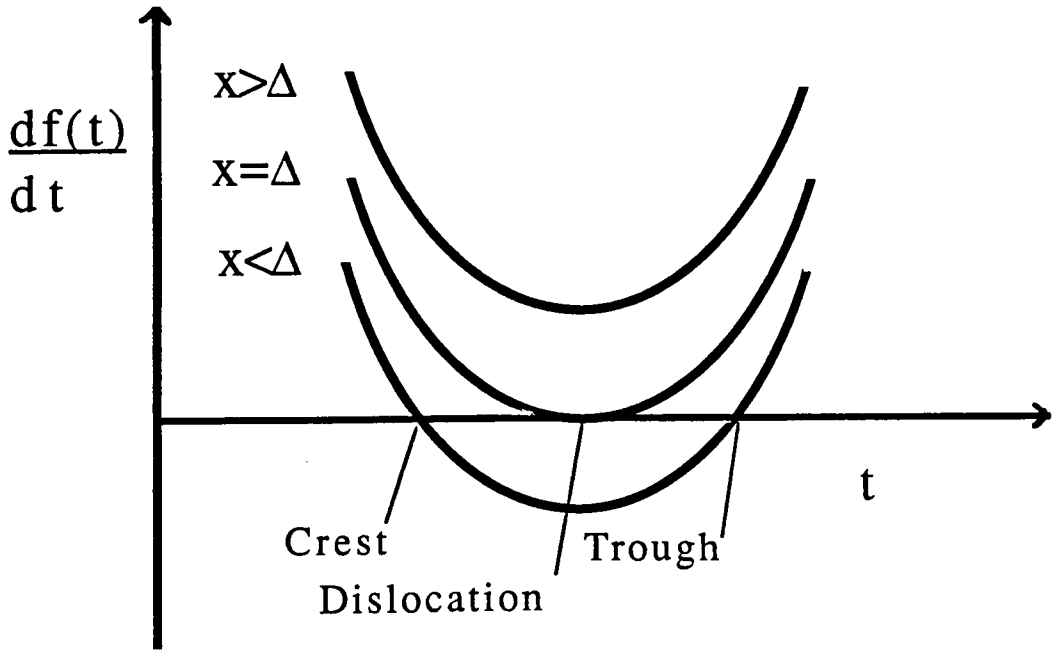


Figure 2.10. The first differential of the wave form.

are zero simultaneously. When observed on an oscilloscope screen, a dislocation manifests itself as a horizontal point of inflection.

If the transducer is scanned in both the X and Y directions, the wave crests in the three dimensional analogue of figure 2.8 will be surfaces and dislocation lines will be the their edges (figure 2.11). This diagram can be related to the actual spatial wave field at any given instant by assuming the wave passes normal to the plane of observation without changing form and setting $Z=c \cdot t$ where is the speed of sound. This is approximately true so as long as only small intervals of time are considered.

There is absolutely no requirement that, in order to be of practical use, dislocations should faithfully represent something real in the wave field. Indeed, all receivers have finite dimensions leaving observation of the real wave field at a point impossible. The dislocation is more usefully thought of as existing in an abstract "parameter space" in which the wave crests form surfaces when their time of arrival is plotted against two arbitrary parameters that characterize the position of the transducer. If the receiver can be considered to be small and, as above, if these parameters are its coordinates on a plane, then this idea of the wave crest surfaces conforms closely to reality. On the other hand, the coordinates of the space in which the dislocation lie could be transducer orientation, rotation or even temperature, in which case the dislocation is more abstract but no less useful. Following the same line of argument, the characteristics of the transducer or of the

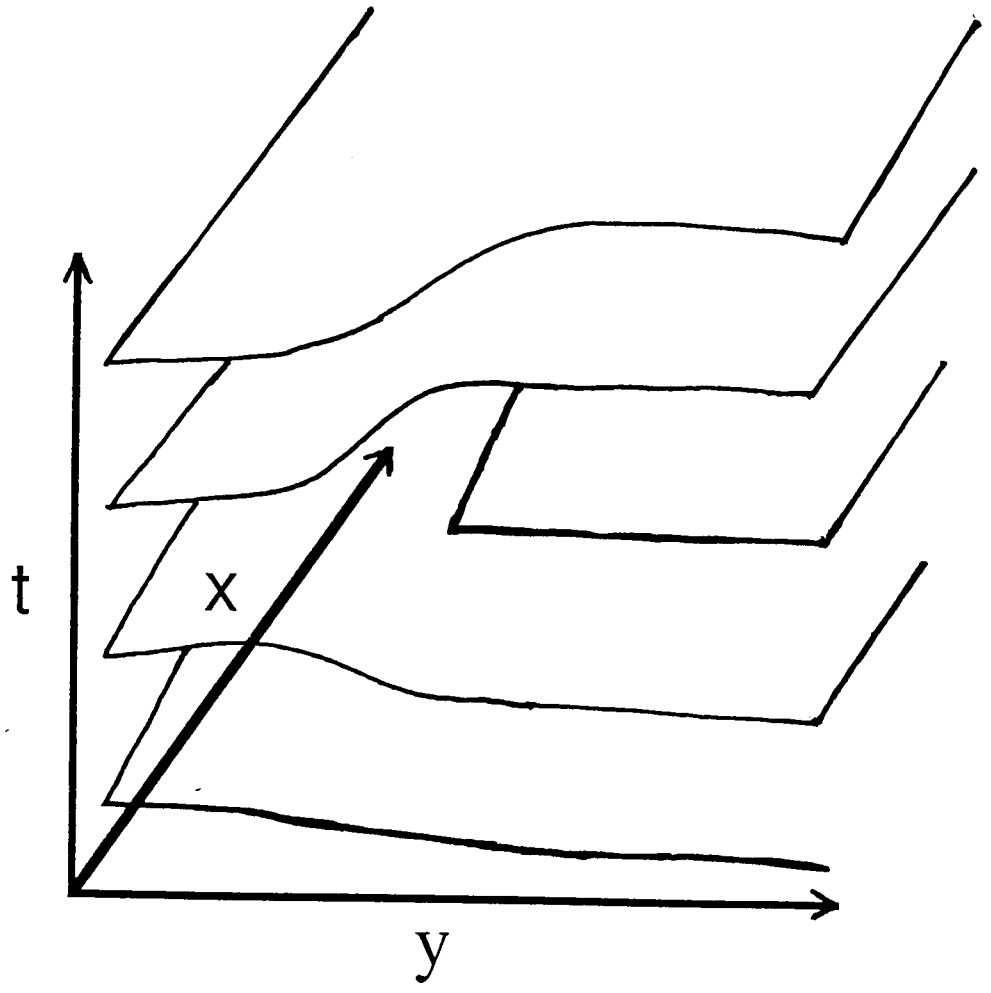


Figure 2.11. A Three dimensional wave crest map showing a dislocation.

receiving electronics do not need to be taken into account as long as they remain constant throughout the experiment.

It would be possible to use three parameters, in addition to time, to describe the wave. In this case the wave crests will be volumes and the dislocations will be surfaces lying in a four dimensional space. Any order of system is possible but there seems to be little worth in going beyond three dimensions.

Dislocations in radio waves were applied by Walford *et al* in a geophysical radar experiment [WALFORD, HOLFORD and OAKBERG 1977]. The aim of their work was to measure the speed of flow of an antarctic glacier by observation of echoes from the rock below it. This was done by marking the position on the surface of the ice of dislocations in this signal. Making use of the fact that dislocations form such well defined markers in the wave field, they were able to measure their location to within one tenth of a wavelength. Under the assumption that the dislocations remain stationary relative to the bedrock they were able to monitor the movement of the glacier over a period of months. These experiments provided the impetus for Nye and Berry's theoretical description of dislocation morphologies.

CHAPTER 3

CAUSTICS

Whereas dislocations are features of a wave field when examined on the sub-wavelength scale, caustics occur in situations in which the wave length is too small to be of importance. In this "shortwave limit", the full apparatus of the wave function is not needed for an accurate description of the wave. It can be replaced by the concept of rays which are the trajectories along which energy flows and which are perpendicular to the wavefronts of the phase picture. Rays can not exist in isolation but occur in bundles or families. Caustics are the characteristic singularities of such groups of rays.

Consider a perfect lens bringing a parallel beam of light rays to a point focus (figure 3.1). If this instrument has been abused in such a way that it becomes distorted, the light rays will no longer be focussed to a point but will "miss each other" enveloping a surface, a section of which is shown in the lower illustration of 3.1. This surface is a caustic.

A simple two dimensional case, in which the caustic is a line, serves to illustrate several of their properties (figure 3.2):

i) Each ray is tangential to the caustic.

ii) Neighboring rays meet at the caustic.

iii) The caustic forms a boundary between the space illuminated by the ray bundle and that in shadow.

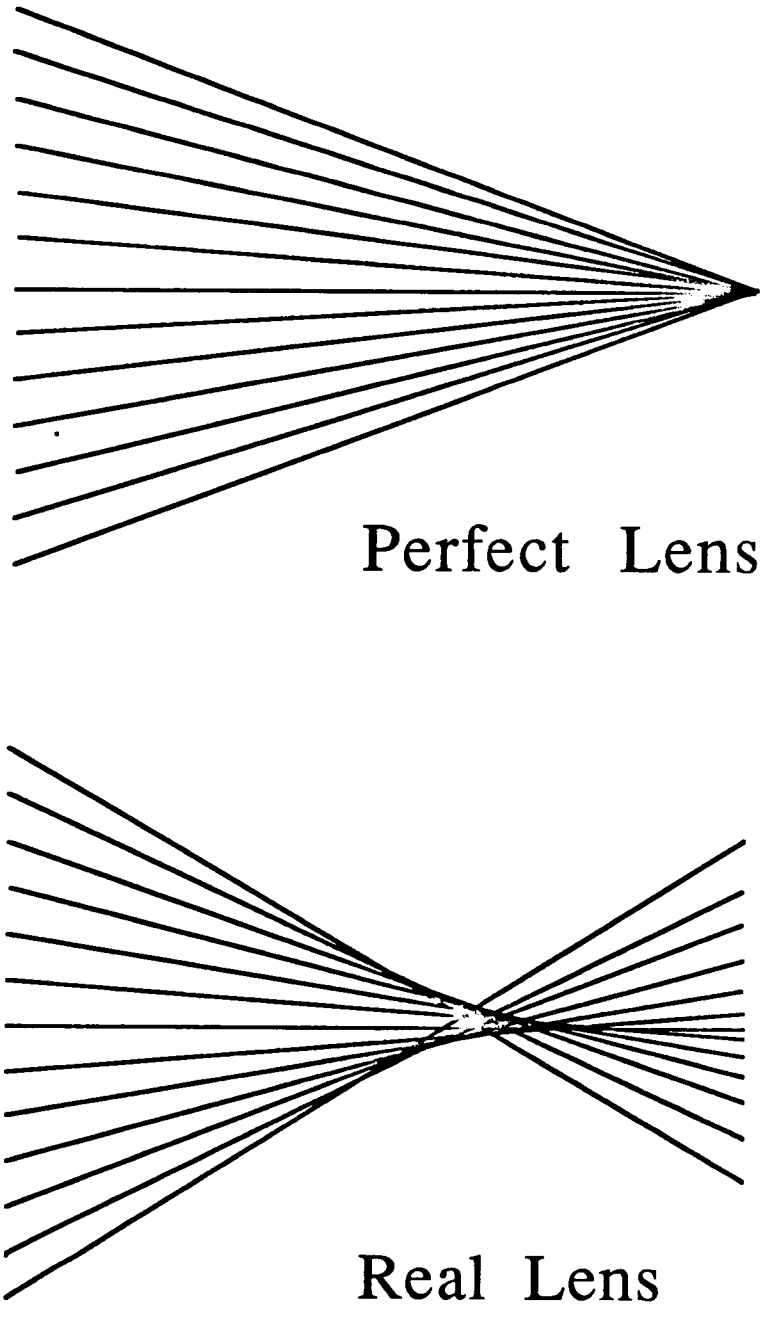


Figure 3.1. Rays focussed by a perfect and by a real lens.

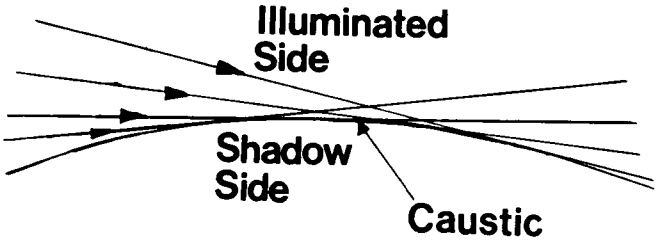


Figure 3.2. A two dimensional caustic.

iv) The density of rays and thus the intensity is high near the caustic.

By consideration of the conservation of energy, it can be shown that the intensity is in fact infinite exactly on the caustic in the ray approximation [LANDAU and LIFTSHITZ 1951] . This unphysical result is mitigated when the finite wavelength is taken into account. Each of properties i) and ii) can be used as the definition of a caustic. Each ray in a three dimensional bundle is surrounded by a set of nearest neighbors and will only meet one of these each time it passes tangential to a caustic.

As a consequence of the structural instability of the point focus demonstrated above, caustics are the pervasive focussing phenomena in the natural world. They account for observations as diverse as the rainbow [DESCARTES 1637], the twinkling of stars [WOOD 1911] and lattice of light observed when sunlight, refracted by the wavy surface of the water, is projected onto the bottom of a swimming pool [BERRY 1980].

In the early Nineteen Seventies it was found that a powerful new form of calculus, "catastrophe theory", can be applied to caustics. The most important achievement of this was the proof that there are seven and only seven distinct morphologies of caustic that are structurally stable [POSTON and STEWART 1978].

As was implied above, the ray approximation breaks down near the caustic, necessitating that the finite wavelength be taken into account. An accurate theoretical treatment of this was given as

early as 1838 by G.B. Airy [Airy 1838]. Because their loci are geometrically related to that of the caustic, this diffraction problem can be solved by the application of Huygens' principle to the wavefronts in the vicinity of the caustic [LANDAU and LIFSHITZ 1951]. This bypasses the approximations implicit in Fresnel and Fraunhofer diffraction theory.

The result Airy derived is:

$$I(x) = \left(\frac{2k^2}{\rho}\right)^{\frac{1}{6}} \times \Phi\left(x \cdot \left[\frac{2k^2}{\rho}\right]^{\frac{1}{6}}\right) \qquad 3.1$$

Where, I, is the intensity of radiation as a function of the distance from the caustic x (defined such that points on the shadow side have positive x), ρ, is the radius of curvature of the caustic, k, is the wave number and $\Phi(t)$ is the Airy function defined by:

$$\Phi(t) = \frac{1}{\sqrt{\pi}} \int_0^{\infty} \cos\left(\frac{\zeta^3}{3} + \zeta t\right) dz \qquad 3.2$$

This integral appears in several other mathematical contexts and has been extensively tabulated in handbooks [ABRAMOWITZ and STEGUN 1964]. The Airy function has its first and largest maximum at t=-1.02, implying that the intensity is greatest at a distance inside the illuminated zone of:

$$x_{max} = -1.02 \times \left(\frac{\rho}{2k^2}\right)^{\frac{1}{3}} \qquad 3.3$$

Actually on the caustic of ray optics the intensity is 36% of this value. As x becomes more negative, the Airy function undergoes oscillations with a steadily decreasing period on the shadow side of the caustic the intensity exponentially disappears. This diffraction profile is graphed in figure 3.3. Note that the scale of this diffraction pattern increases only as the cube root of the radius of curvature. This implies that if a system is scaled up, the diffraction pattern becomes relatively finer. The extent to which Airy's theory, derived for continuous radiation, applies to pulses of sound is a necessary subject of investigation.

There is a body of work mainly due to Theocaris applying caustics to the mechanics of materials [THEOCARIS and GDOUTOS 1972]. The caustics formed by reflection from a surface are measured and compared to those calculated to occur if it undergoes its theoretical deformation. This has been used to test theories of plastic deformation at crack tips and to measure stress intensity factors.

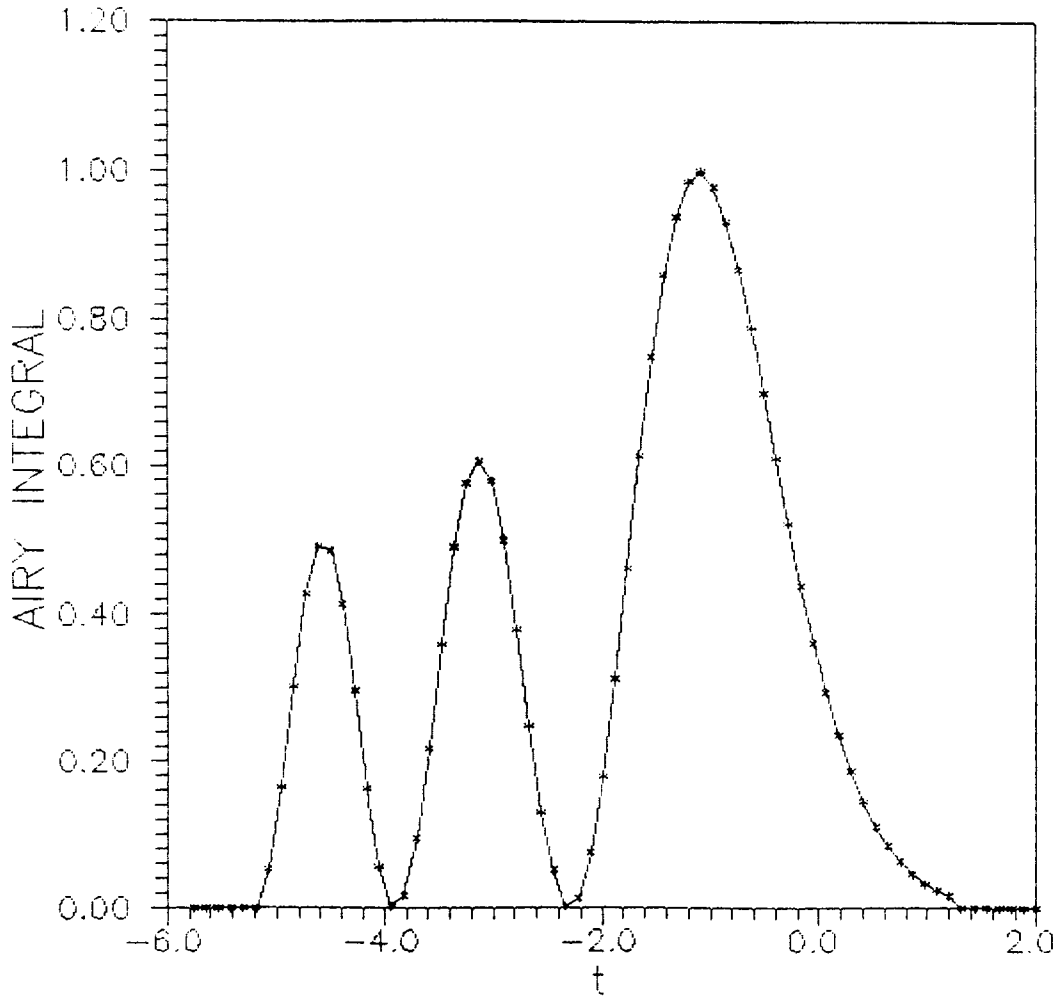


Figure 3.3. The Airy diffraction profile.

CHAPTER 4

DISLOCATIONS AND THE MEASUREMENT OF SURFACE ROUGHNESS

Introduction

Dislocations provide a measure of the level of disruption of the sound field. It would be of interest to relate this disturbance to properties of the object reflecting the sound such as, in this case, its surface roughness. This was done by measuring the ultrasonic dislocation density above various surfaces and determining its dependence on the surface roughness. An attempt was then made to account for these results using a computer model.

As they constitute a readily available set of surfaces of varying roughness, sand papers of various grades were used as reflecting surfaces. The dislocations were defined by the creation and destruction wave crests as described in chapter 2 and were observed by scanning the focal point of a focusing transducer above the surface, as is shown schematically in figure 4.1.

Surface roughness can be characterized by measuring the variation in the magnitude of the ultrasonic echo from the surface as a function of wavelength and angle of incidence [FITTING and ADLER 1981]. The dislocation technique has the advantage over this in that it can be used in situations where variation of the angle of incidence is not possible. Also the precise definition of the location of dislocations makes measurement of small changes in surface character possible.

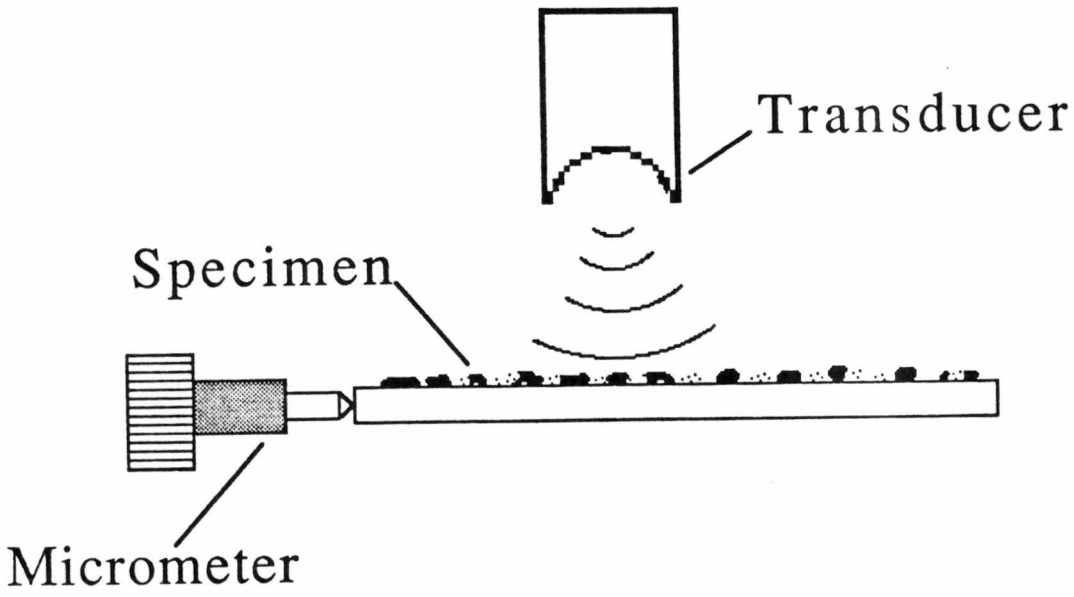


Figure 4.1. Schematic diagram of the ultrasonic transducer being scanned above a rough surface.

Experimental Procedure

Pulses of ultrasound were generated and received by a piezoelectric ultrasonic transducer manufactured by Panametrics Incorporated (model V317). This is a broadband transducer possessing a fixed, central frequency of 20 MHz and is spherically focussed with a focal length of 12.5 mm (.5 inches). A Panametrics model 5052PR pulser/receiver, configured in pulse echo mode, provided electrical impulses to the transducer then amplified and filtered the returning electrical impulses. Once processed in this way the signals were viewed on a Tektronix 2236, 100 MHz oscilloscope that was equipped with the ability to magnify a section of the time base for more detailed viewing.

As all the ultrasonic experiments described in subsequent chapters were performed using the above equipment in the configuration described, these pieces of this apparatus will be referred to as "the transducer", "the oscilloscope", *ecetra*.

The position of the specimen was manipulated using a X-Y micro-positioner by Oriel Corporation (serial number 16263). This is a translation stage, designed to be used on an optical bench, that allows the positioning of a platform, of nominal size 150*150 mm, with two perpendicular, independent translations. The relative coordinates of the platform, "X" and "Y", could be measured to the nearest μm via micrometers. This micro-positioner was utilized to some extent in all the experiments described.

The test specimens were samples of adhesive backed sand paper manufactured by 3M. The specimen was fixed to a parallel sided steel block which was mounted, using modelling clay, to the bottom of a beaker. The beaker was filled with water and fixed to the micropositioner placed to scan in a horizontal plane. The transducer was fixed into position in the water, aligned perpendicular to the surface. The distance of the transducer from the surface was such that the time of flight of the beginning of the first signal to arrive was 20 μs. At this height, the focal point of the transducer is about 2.2 mm above the surface. By ensuring that this remained so as X and Y were varied, the inclination of the sample was set parallel to the plane of the scan. The average time at which the maximum of the echo signal occurred, T, was found by quickly varying X and Y and observing the oscilloscope signal.

For a fixed value of Y, a section of the time base extending 0.05 μs on either side of T was searched for dislocations as X was increased. The dislocation was defined by the creation of a new wave crest as described in chapter 2. The number of dislocations was counted and the total distance traversed recorded. This was repeated for various values of Y until a statistically significant number of dislocations (on the order of 400) had been counted.

The number of dislocations per unit length was divided by the length of the observation window (0.1 μs) to yield a dislocation density of dimensions per unit length per unit time. This quantity was multiplied by the speed of sound in water (1485 m/s [WEAST

1986] which is more conveniently expressed here as 1.49 mm/μs) to convert it to a number density per unit area. As mentioned above the area in question is equivalent to a vertical plane parallel to the X-direction.

The procedure was repeated to obtain the dislocation density above sand paper grades 120, 240, 360 and 600.

In order to gain an over view of the dislocation structure the loci in X and Y of all the dislocations that could be found, within a 0.360 mm by 0.360 mm section of space, above the 120 grade paper were mapped.

Samples of each grade of paper were gold coated and photographed in a scanning election microscope. From the micrographs the density of particles on the surface was counted.

In order to make possible the construction of a computer model of the above system, the beam characteristics of the transducer were measured. A 1.6 mm diameter steel ball was scanned in front of the transducer along a line passing perpendicular to the axis of symmetry. The distance between the ball and the focal point was set to be the same as in the above experiments. The echo amplitude was plotted as a function of the displacement of the ball from the axis of the transducer.

Results

The beam profile of the transducer, at the distance relevant to this experiment, is shown in figure 4.2.

The relationship between wave field dislocation density and the density of sand particles for the four grades of sand paper is shown in figure 4.3. The error bars represent the random error attributable to the fact that one is counting discrete entities given by:

$$\sigma = \sqrt{N} \qquad 4.1$$

where N is the number of objects counted.

The nature of the dislocations above the 120 grade paper is illustrated by figure 4.4. The dislocations are a tangle of random yet continuous lines. The one dislocation that does appear to end within the area of the search did so because its time of flight changed until it entered a region of the signal too faint to be observed. One particularly interesting occurrence is to be found at coordinates, (50 μm, 250 μm) where a dislocation crosses over itself. This is possible because the time of arrival is rapidly changing, the observed "twist" is actually a longitudinal view of a helical piece of dislocation. Structure on a scale smaller than the 74 μm wavelength can readily be observed.

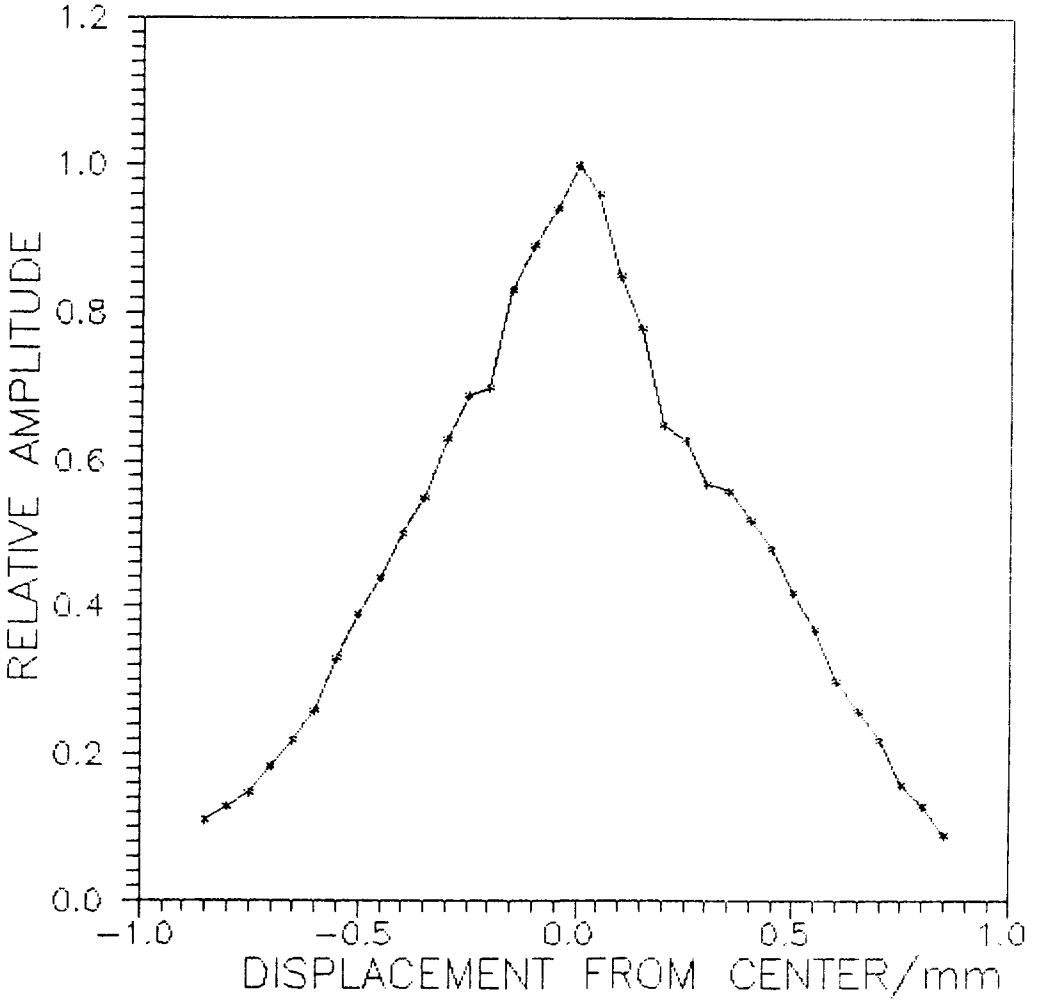


Figure 4.2. The amplitude profile across the beam of the transducer.

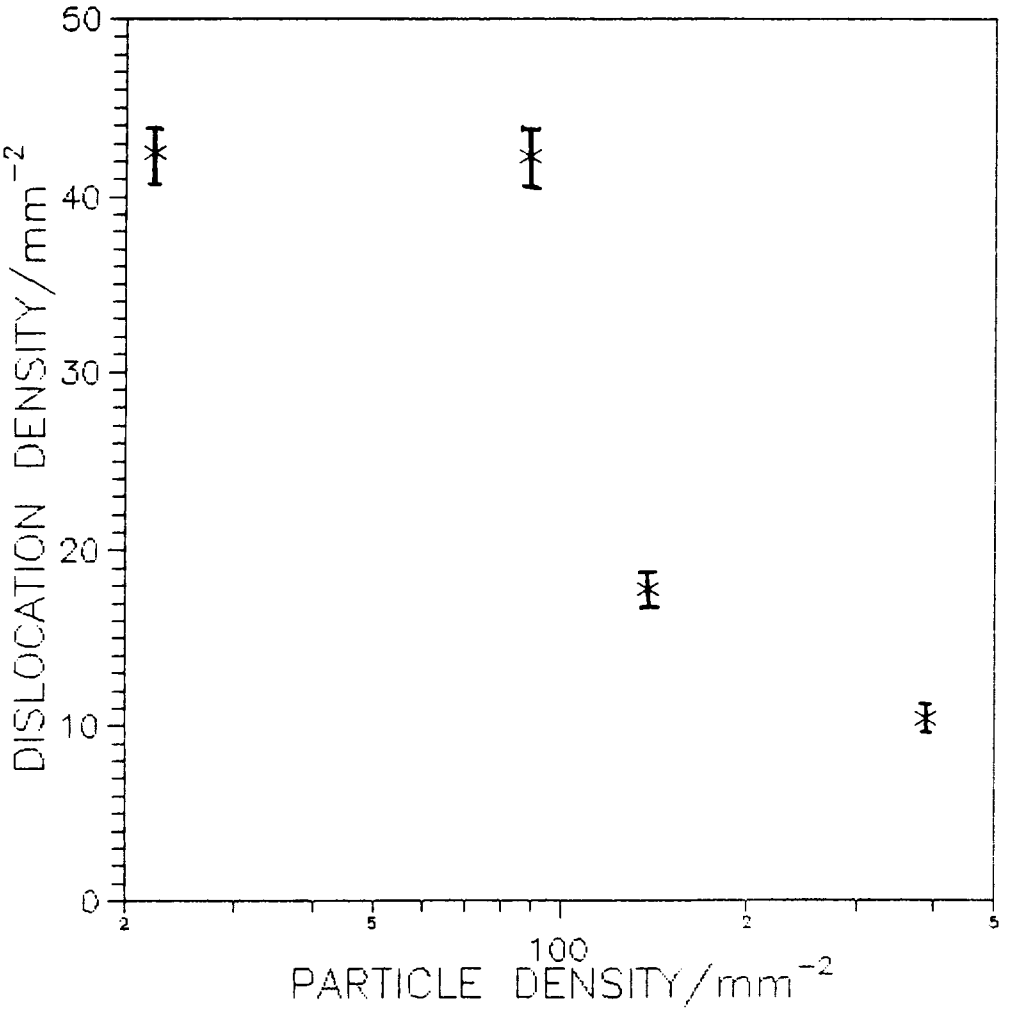


Figure 4.3. The relationship between dislocation density and particle density for various grades of sand paper.

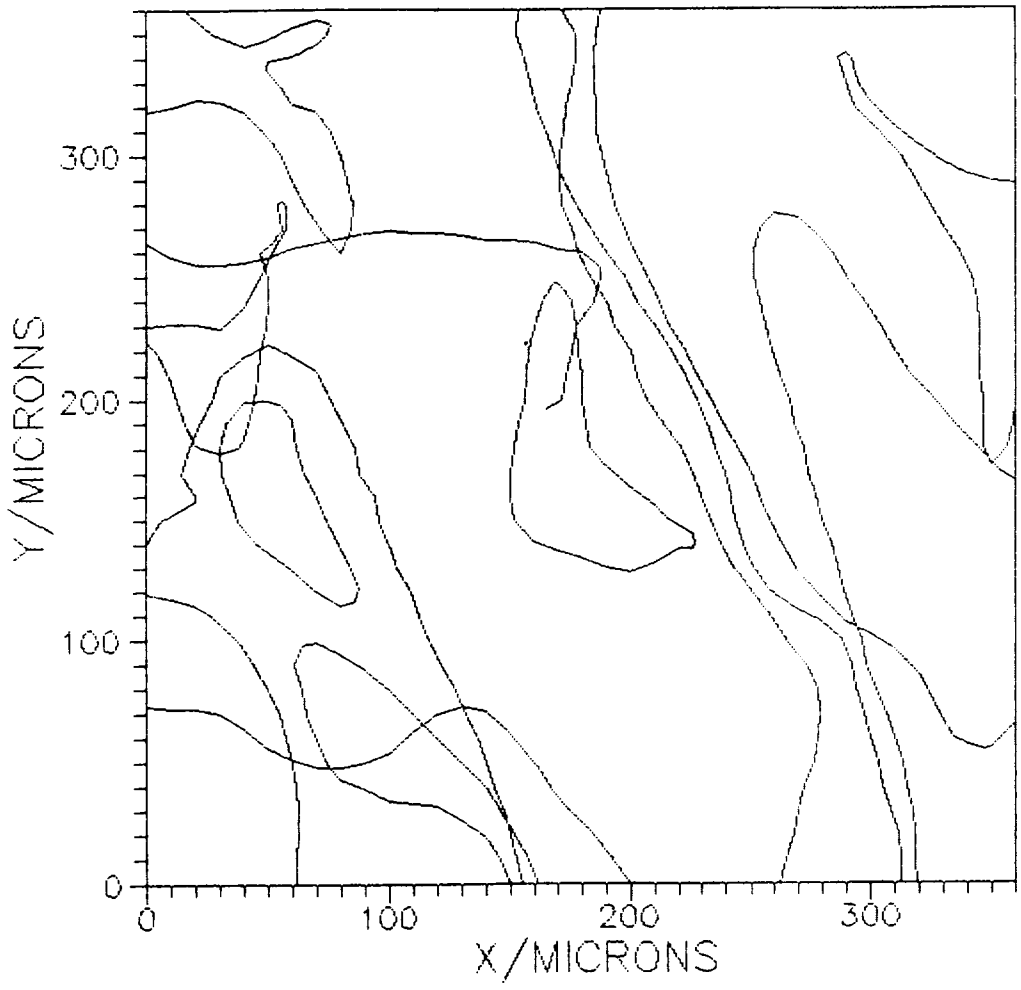


Figure 4.4. Dislocations generated by 120 grade sand paper.

Mathematical Model

The surface was modeled by a plane containing a certain density of randomly spaced, discrete reflecting points. Let the surface be the plane, z=0.

The pulse shape, f(t), was approximated by the function:

$$f(t) = e^{at^3} \cdot \sin(\omega t) \qquad 4.2$$

where: $a = 200{,}000$ if $t>0$

$a = -1800$ if $t<0$

The values of, a, were chosen to make the function resemble the pulse shape given in the specifications of the transducer provided by the manufacturer. The cubic time dependance in the exponential was chosen so that the function and its first two derivatives would be continuous at zero time.

The signal at a point above the surface, F(t), was assumed to be composed of a sum of contributions from each reflecting point. Each had the above form and, according to its the distance between the reflector and receiver, was scaled in amplitude and shifted in time. Figure 4.5 is a schematic diagram of this model showing some of the ray paths involved. Expressed mathematically:

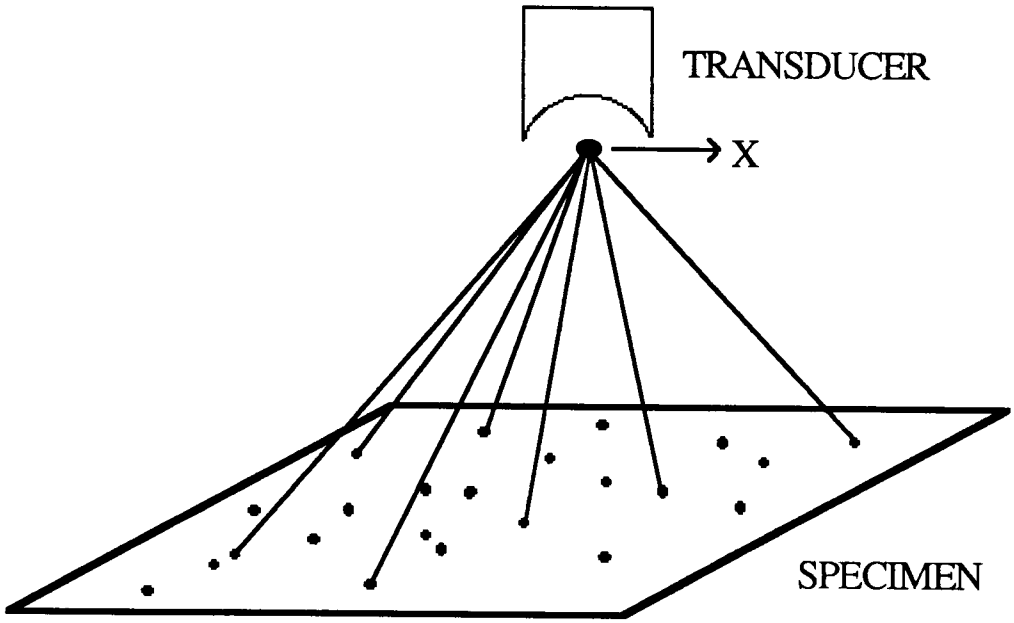


Figure 4.5. Schematic illustration of the mathematical model used.

$$F(t) = \sum_{i=1}^{N} \frac{A(S_i)}{D_i^2} \cdot f(t-\tau_i) \qquad 4.3$$

where N, is the number of reflecting points

t, is the time since the emission of the signal.

D_i, is the distance between the i^{th} reflector and the point of measurement.

τ_i, is the time of arrival of the signal from the i^{th} reflector which is given by:

$$\tau_i = \frac{2 \cdot D_i}{\text{speed of sound}} \qquad 4.4$$

$A(S_i)$, is the beam profile of the transducer expressed in terms of the perpendicular distance, S_i, between the reflector and the normal to the surface that passes through the surface. The beam was simulated by fitting a straight line to the experimental data presented in figure 4.2:

$$A(S_i) = 1 - \frac{S_i}{1.0 \text{ mm}} \qquad 4.5$$

The amplitude at a distance from a point source is inversely proportional to that distance. Since, it is the echo strength received back from that point that is being considered, the amplitude of each contribution varies as the inverse square of its distance.

A computer program was written that, having produced a random array of points of a given density, was able to return the value of the echo signal for a given position of the receiver and after a given time. A listing of this program is provided in appendix A. By replacing f(t) in equation 4.3 with the appropriate differential, the first two differentials of the signal were also found. The program was designed to search the x-t plane for dislocations. The value of y was kept equal to zero and that of z was held constant at a value corresponding to that used in the experimental work.

Starting at a given value of t, t_0, t was increased until a zero in the second differential of f(t), f(t)″ was found. This contour of f(t)″ was then followed in x-t space and each change in the sign of the first differential, f(t)′, noted. Whilst f(t)′ was positive, the total x-component of the contour was measured. The total number of zeros in f(t)′ was divided by this distance to yield a line density of dislocations. As there is one zero of f(t)″ per cycle, this quantity had to be divided by the wave length to yield the dislocation density per unit area in the vertical plane. In order to ensure a statistically unbiased measure of the dislocation density a limit of 50 μm was placed on the horizontal distance that could be scanned before

changing the surface and repeating the procedure. The path being followed was checked to ensure that it was not doubling back on itself.

The results of this simulation are shown, along with the experimental, data in figure 4.6. The values of λ given on the graph represent the time, measured in wave cycles, beyond that of the earliest possible arrival of a reflection. It can be seen the dependance of the dislocation density on the particle density depends heavily on the portion of the signal being searched. At the front of the signal the dislocation density decreases as the surface becomes more smooth at a rate similar to that observed experimentally. At higher values of λ the predicted dislocation density is constant to a level close to 50 per mm. The region of the pulse searched experimentally was a two cycle interval between, approximately, λ=1.5 and λ=3.5. Despite its simplicity, the model was successful in reproducing the observed dislocation density to within a factor of two.

Discussion

A relationship between the dislocation density in the reflected signal and the roughness of the reflecting surface has been demonstrated.

The accuracy of modeling the surface as a set of discrete, point-like reflectors is limited because the interaction between a sound wave and a surface is more complex. Local variations in

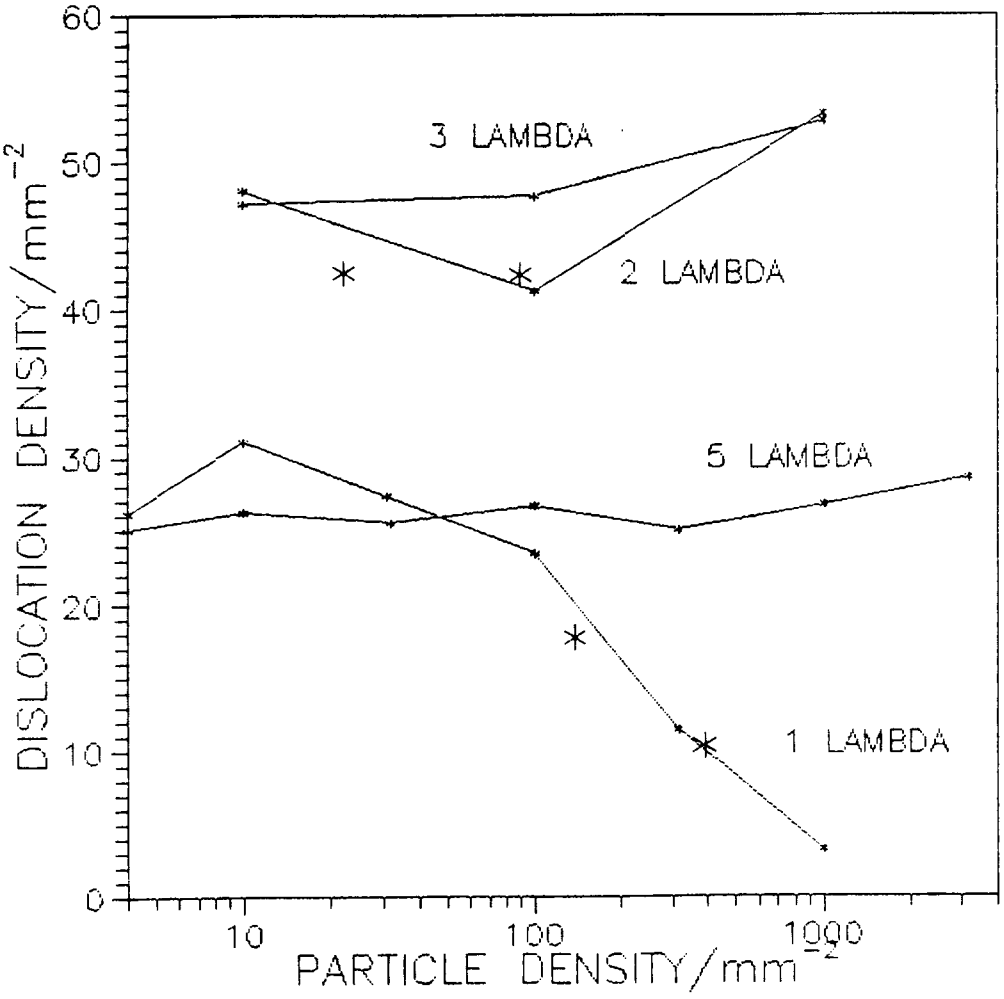


Figure 4.6. Theoretically predicted dislocation densities.

surface topology will produce a frequency dependance in the reflected signal which will alter the shape of the returning pulse. Surface waves will also be generated producing secondary reflections.

Although there are many techniques, ultrasonic and otherwise, of measuring surface roughness, it is the precision with which dislocations can be located that gives the above method a potential advantage. This makes possible detection of small changes in the characteristics of the surface. This could be a very useful diagnostic tool for monitoring, for example, the corrosion rate on the inner wall of a reaction vessel.

CHAPTER 5

ULTRASONIC DISLOCATIONS AND METALLIC MICROSTRUCTURES

Introduction

When a pulse of ultrasound is reflected from a metallic slab, in addition to strong reflections from any interfaces, a background "noise" of signals originating from the body of the specimen is observed. The purpose of the experiments presented in this chapter is to show that dislocations can be observed in this backscattered signal and that their statistics can be related to the microstructure of the metal. The microstructural feature pertaining to this phenomenon is likely to be the grain size which is of great practical importance to metallurgists.

It is a good approximation to assume that sound waves can only be scattered by features whose scale is greater than one tenth of a wavelength [KRAUTKRAMER and KRAUTKRAMER 1983]. Inside a typical metal the wavelength of the 20 MHz compression waves to be used is about 300 μm therefore, detail on a scale larger than 30 μm is amenable to study. This includes most metallic grain structures.

The dislocation density produced by the microstructure was measured using the apparatus shown schematically in figure 5.1. In a manner similar to that described in the previous chapter, the technique was to scan the transducer along a straight line counting the dislocations. A major difference being that in this case the focal point of the transducer is below the surface of the specimen. The

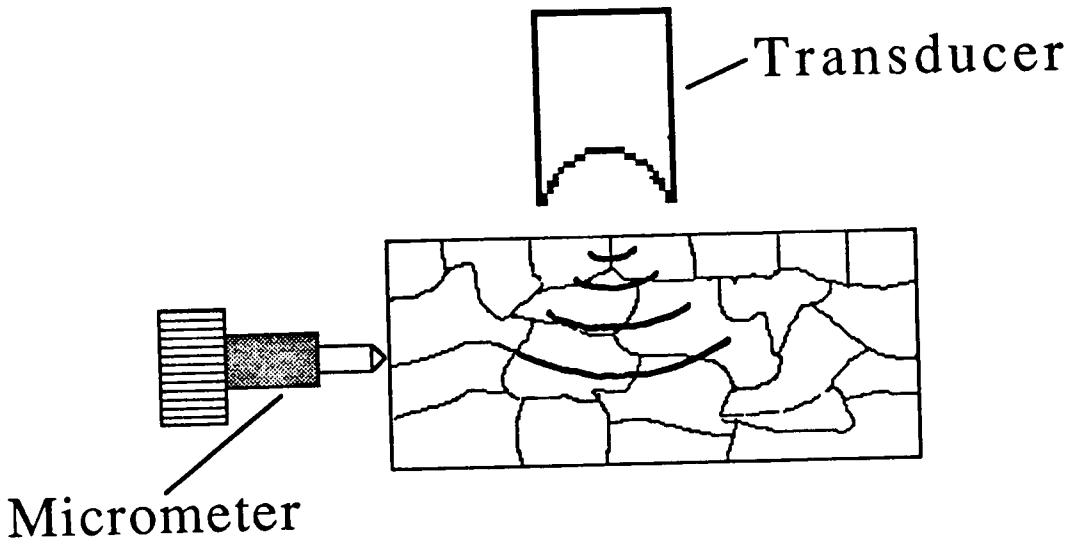


Figure 5.1. Schematic diagram of an ultrasonic transducer scanning the microstructure of a metal.

microstructure was the changed by an annealing operation and the dislocations reexamined. The actual microstructure was then examined by conventional optical microscopy.

Both surface roughness and grain size can be measured by ultrasonic spectroscopy. The specimen is characterized by comparison of the frequency spectrum of the pulse before and after interaction with the sample [PAPADAKIS 1968]. An advantage dislocations offer over such techniques is that one can choose to count dislocations over a narrow section of the time base and thus measure the microstructure at a particular depth. A large section of the pulse is required to take a meaningful Fourier transform thus forfeiting this depth information. Also, dislocations offer means of measuring anisotropy not possible with spectroscopic methods. As mentioned in previous chapters, the precise location of dislocations permits the measurement of small changes in microstructure.

Experimental Procedure

Before any measurements were made the samples were polished to a flat, 600-grit finish. They were then placed on the micro-positioning stage and immersed in front of the fixed transducer. As described in chapter four, the inclination of the specimen was adjusted until its surface was parallel to its plane of motion. The height of the transducer was adjusted until the beginning of the first echo from the front face of the sample

occurred at 9.0 μs. This corresponds to the focal point lying approximately 3 mm below the surface of the sample.

Again using the same procedure described in chapter four, the number of dislocations per unit length occurring inside a certain section of the time base was recorded along various parallel tracks. Several scans, each approximately 10 mm long, were made until a statistically significant number of dislocations had been counted. The "time window" used was between 10.8 and 11.0 μs which is equivalent to monitoring a slice of the specimen between 4.5 and 5 mm below the surface. In order to measure the isotropy of the acoustic dislocation field, scans were made both parallel and perpendicular to the rolling direction of the plate.

The brass specimen was a 12.7 mm thick plate of yellow brass. It was cold rolled until 7 mm thick and annealed for five hours at 600 °C. In every case mentioned in this chapter, the anneals were terminated by quenching with water. The dislocation density was measured along lines parallel and perpendicular to the rolling direction both in the as-rolled state and after the anneal. After polishing the surface was etched using an aqueous solution of CrO_3, nitric acid and sulfuric acid [ASM 1988] and optical micrographs taken of the grain structure.

The stainless steel specimen was in the form of a 12.7 mm thick plate. It was too hard to cold roll but was annealed for three days at 1050 °C in air. The dislocation density was measured along two perpendicular directions both before and after the anneal.

After polishing the specimen was etched with methanolic aqua regia [ASM 1988] solution to revel its grain structure.

The aluminum sample was a 6.8 mm thick rolled plate. The plate, as-received, was annealed for several different lengths of time at 400 °C. A portion of it was also cold rolled down to a thickness of 2.2 mm being annealed for several different times at the same temperature. At each stage the dislocation density was recorded both parallel and perpendicular to the rolling direction. In the case of the thinner aluminum samples the above protocol requires the analysis of a signal that has undergone several reflections from the walls of the specimen. Despite this, the time window was kept the same for the sake of consistency. Care was taken to mount the samples such that both interfaces were between metal and free water.

From the micrographs, the grain size was measured by counting the number of grain boundaries per unit length intersecting a straight line. The average grain diameter was taken to be the inverse of this quantity. In every case the test line was in the plane of the plate either parallel or perpendicular to the rolling direction.

Results

The average amplitude of the ultrasonic signal in the vicinity of the time base investigated was an order of magnitude smaller than that of echoes received from the specimen interfaces. Despite this, dislocations could be readily observed in the signal.

The results obtained from the brass specimen are shown in Table 5.1. The quantity named "R" refers to the ratio between the value of the property, either grain size or dislocation density, measured parallel to the rolling direction and perpendicular to the rolling direction. The numbers in parentheses represent an estimate of the standard error on that measurement. Figures 5.2 to 5.5 are optical micrographs of the brass specimen showing the change in microstructure on annealing. Recrystallization and grain growth processes are apparent; before the anneal the grains are elongated along the rolling direction, after the anneal they assume a flat faced equiaxed state and twins are visible.

Figures 5.6 to 5.9 are micrographs of the steel specimen showing that the anneal resulted in an approximately 3 fold increase in the grain size. The grains were flat sided slabs with many twins visible. The shape of the grains was not effected by the anneal. The grain size changed from 43± 2 μm to 145±6 μm. This was accompanied by an increase in the dislocation density from 44.7±1.3 to 52.2±1.4 per square millimeter. Because the rolling direction could not be identified, these quantities are averages over two mutually perpendicular directions in the plane of the plate.

	Grain size (μm)		R	Dislocation density (per square mm)		R
	Parallel	Perpendicular		Parallel	Perpendicular	
Before Anneal	54(4)	35(3)	1.54(0.25)	31.5(1.5)	33.5(1.5)	0.94(0.10)
After Anneal	69(5)	54(4)	1.28(0.19)	39.0(1.5)	42.2(1.5)	0.92(0.07)

Table 5.1. Summary of the results for brass.

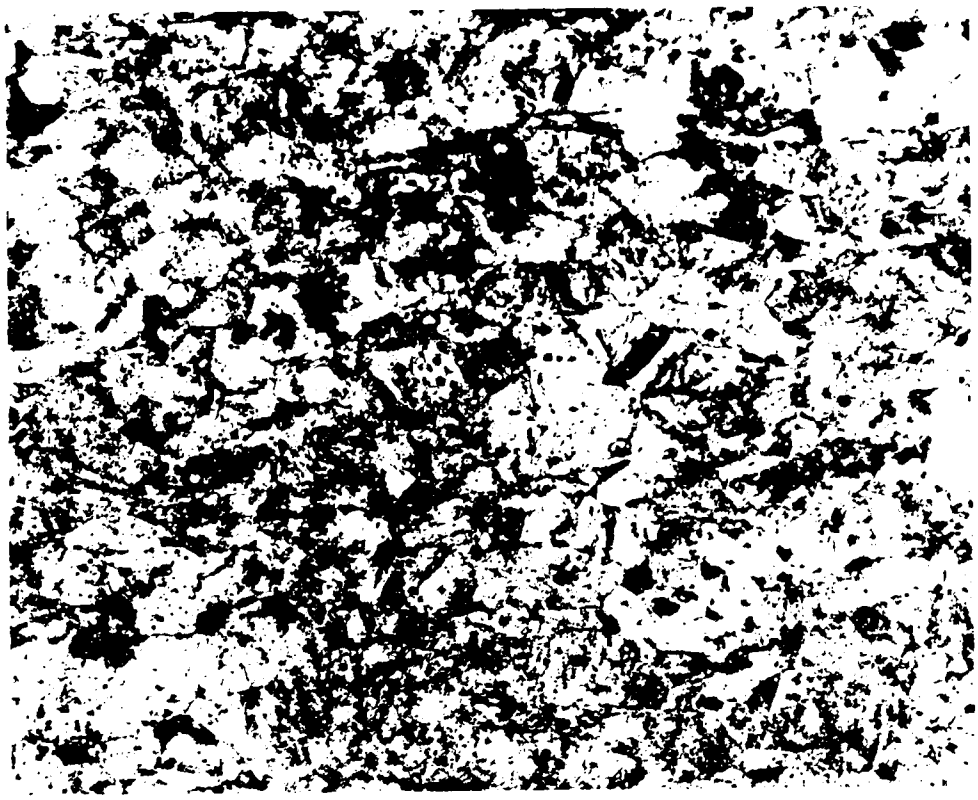


Figure 5.2 Brass, before anneal, horizontal plane, x320

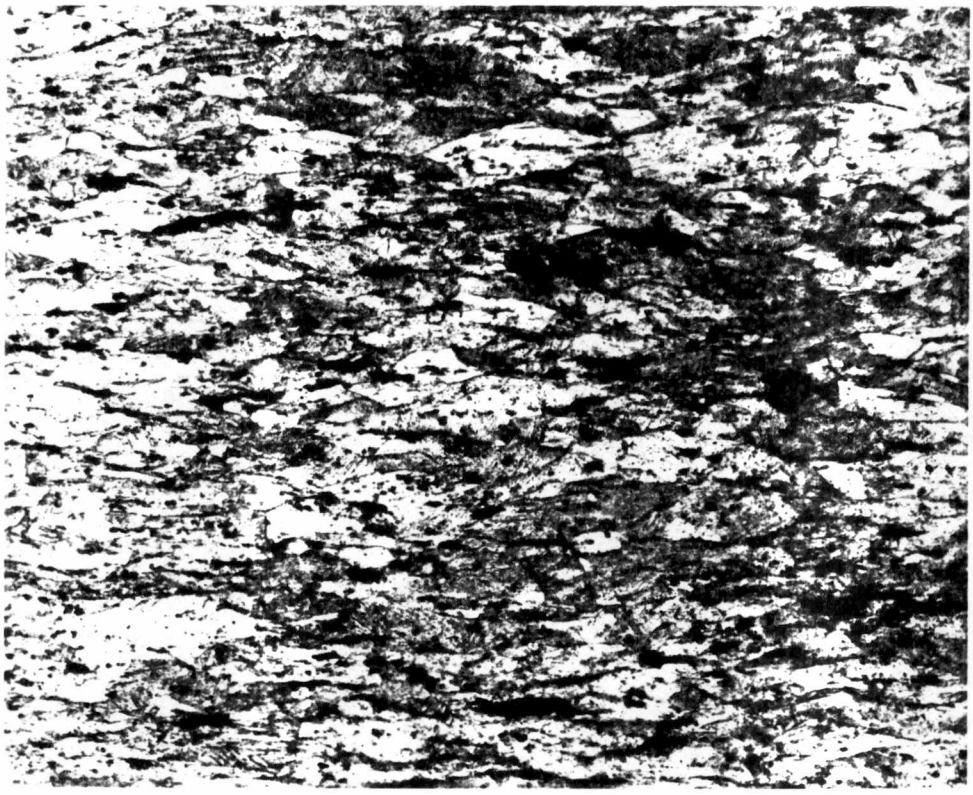


Figure 5.3. Brass, before anneal, vertical plane, x320

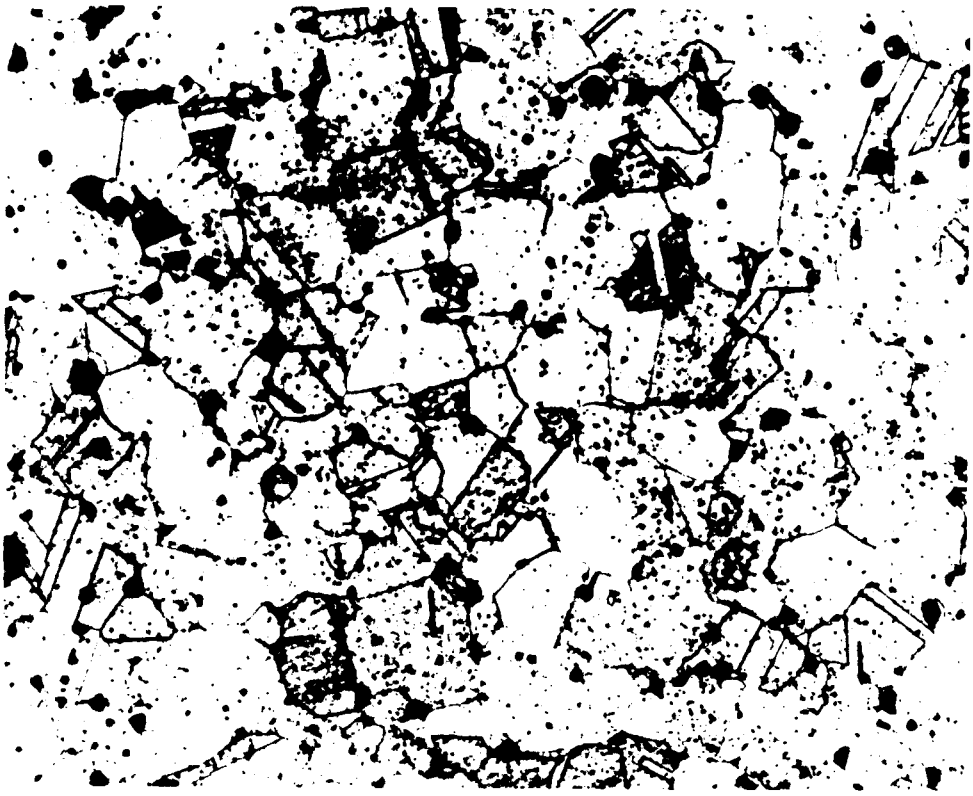


Figure 5.4. Brass, after anneal, horizontal plane, x320.



Figure 5.5. Brass, after anneal, vertical plane, x320.

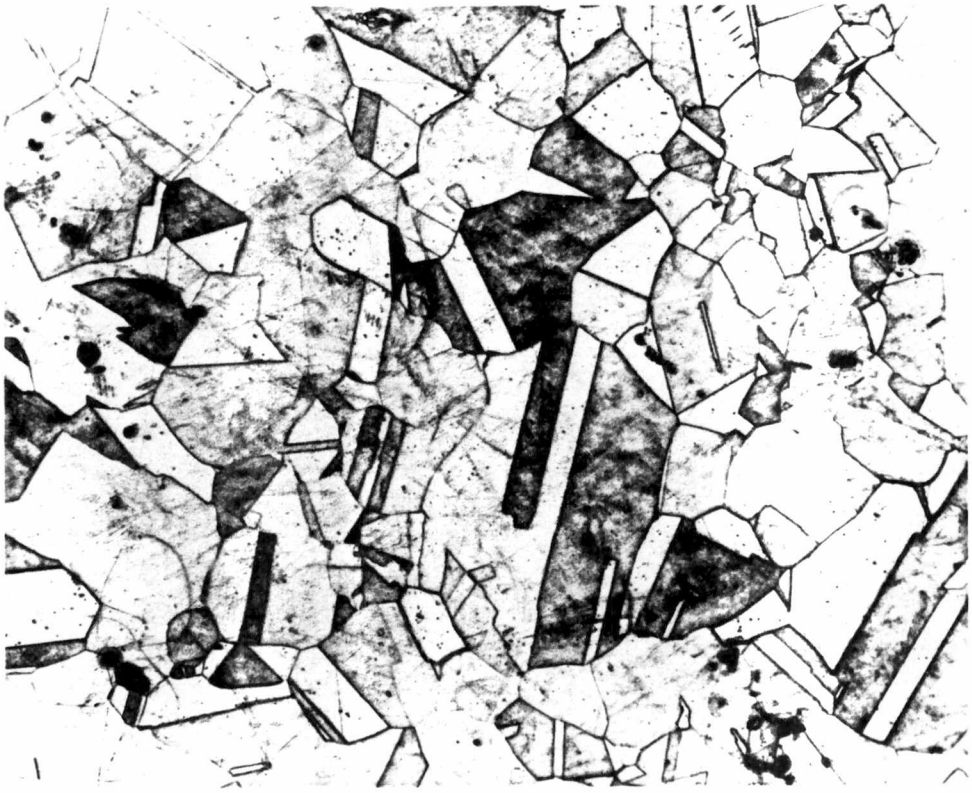


Figure 5.6. Steel, before anneal, horizontal plane, x160.

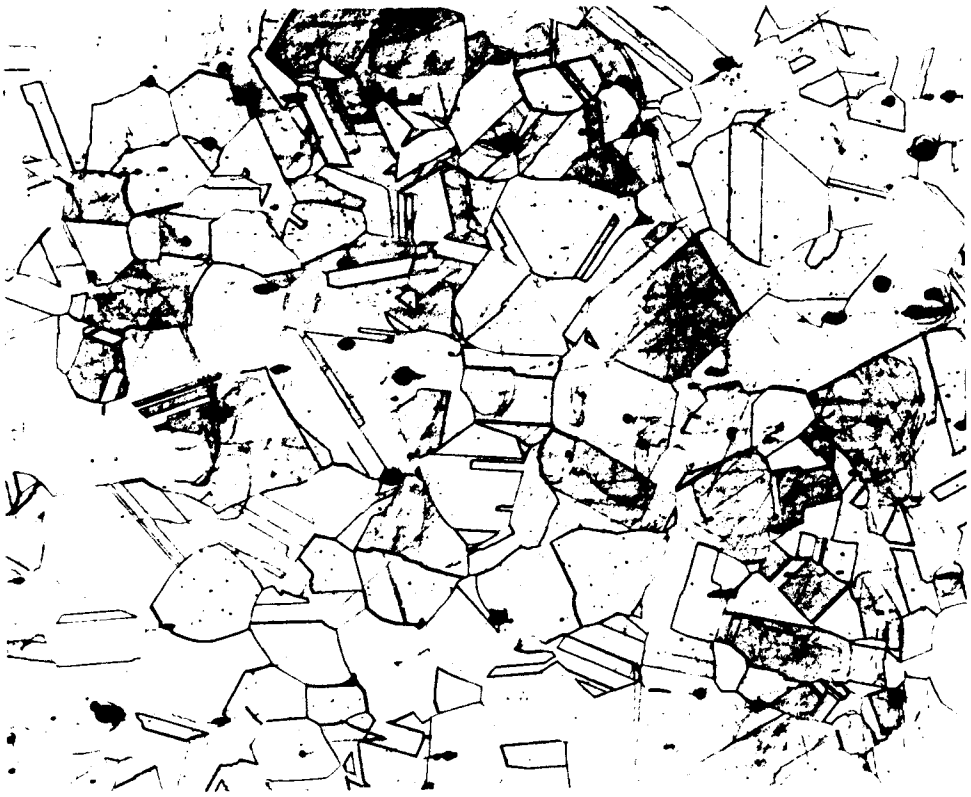


Figure 5.7. Steel, before anneal, vertical plane, x160.



Figure 5.8. Steel, after anneal, horizontal plane, x80.



Figure 5.9. Steel, after anneal, vertical plane, x80.

The relationship between grain size and dislocation density observed for these two metals is summarized in figure 5.10.

With the aluminum specimens, micrographs of sufficient quality for grain size measurement could not be obtained. Despite this, the behavior of the acoustic dislocation densities and anisotropies with annealing time is still informative. Figure 5.11 shows the dislocation density above the as-received aluminum, measured in both directions as a function of annealing time. In order to gain some insight into the progression of the microstructural changes, the hardness is shown on the same axes (the solid line without data point symbols). The variation of the anisotropy, "R", value defined above is given on figure 5.12. Note that R increases to unity at long annealing times. Figures 5.13 and 5.14 are a similar presentation of the data obtained from the further rolled aluminum. It is of interest that the first three points on figure 5.12 show a similar peak, in the first six hours of annealing, to that observed in figure 5.14 for the further rolled aluminum.

Discussion

The above results demonstrate that there is definitely a relationship between dislocations in the backscattered ultrasonic field and the microstructure of the specimen.

From figure 5.10 it can be seen that the dislocation density increases as the grain size increases. As each grain boundary is a

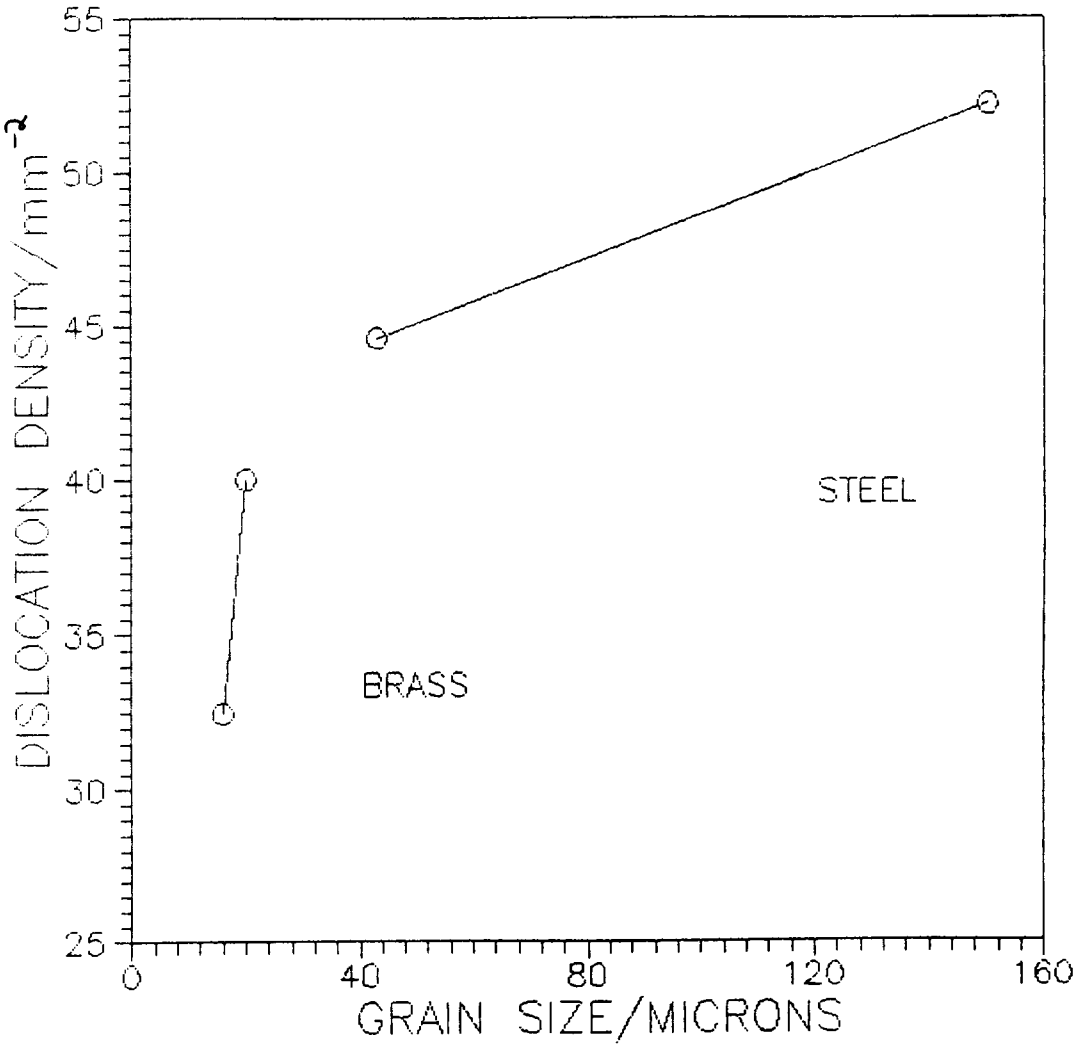


Figure 5.10. The relationship between grain size and dislocation density.

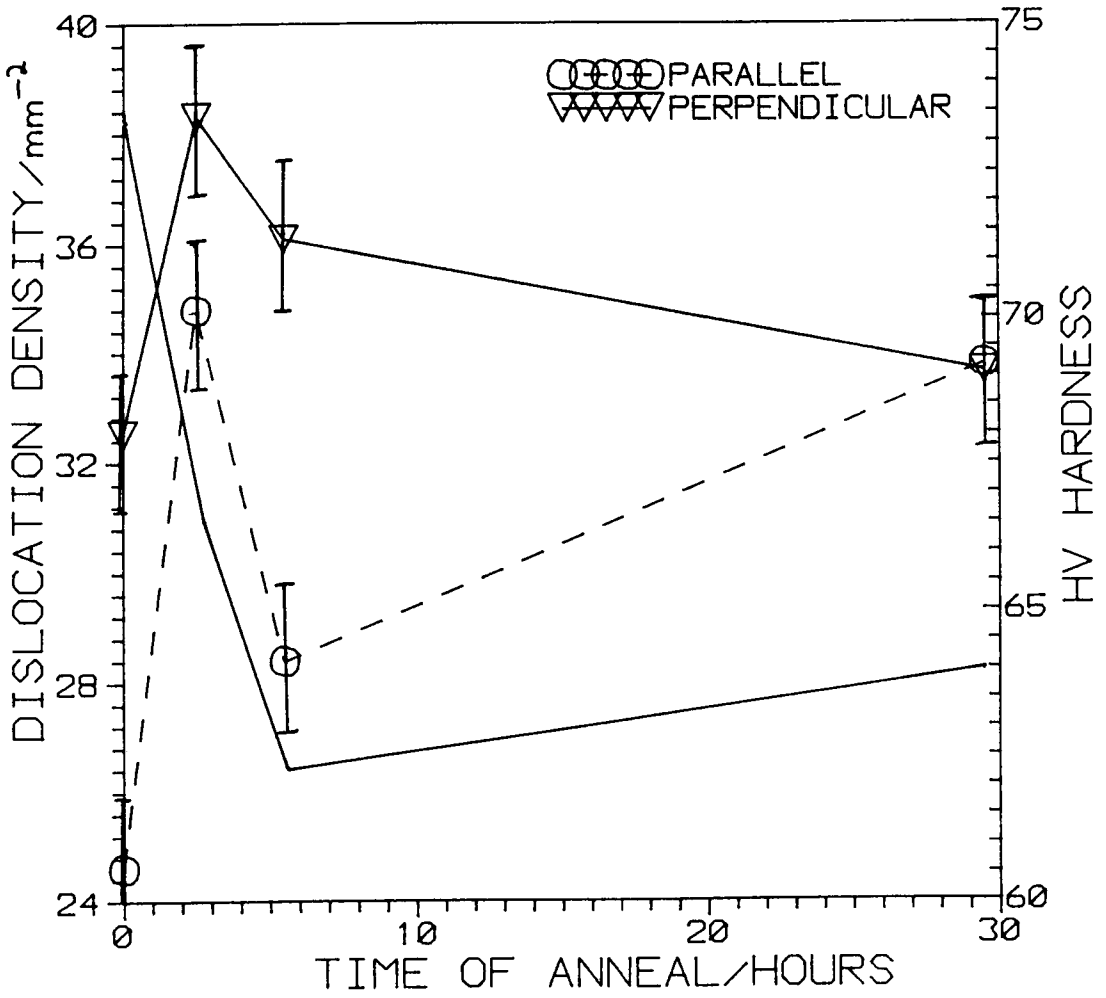


Figure 5.11. The dislocation density above the "as received" aluminum as a function of time of anneal.

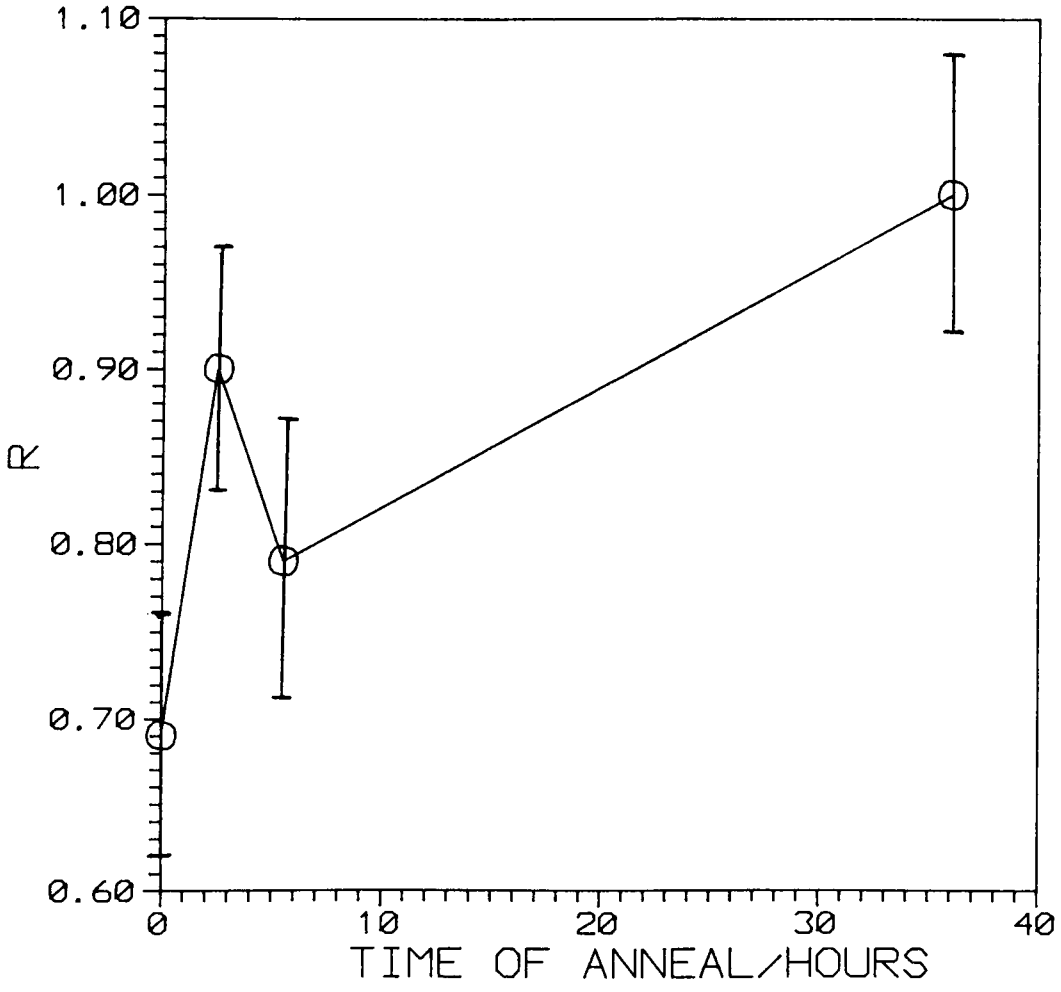


Figure 5.12. The dislocation anisotropy above the "as received" aluminum as a function of time of anneal.

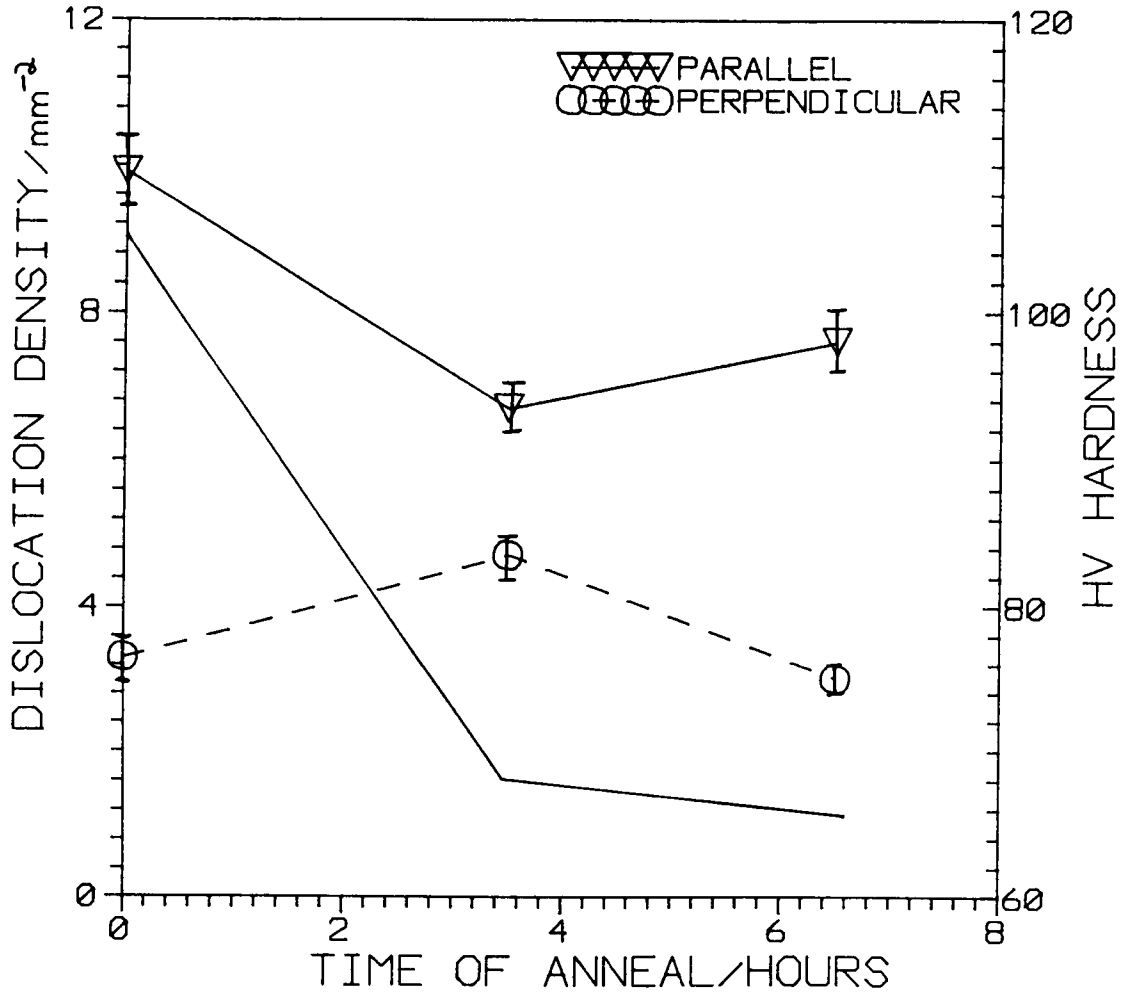


Figure 5.13. The dislocation density above the rolled aluminum as a function of time of anneal.

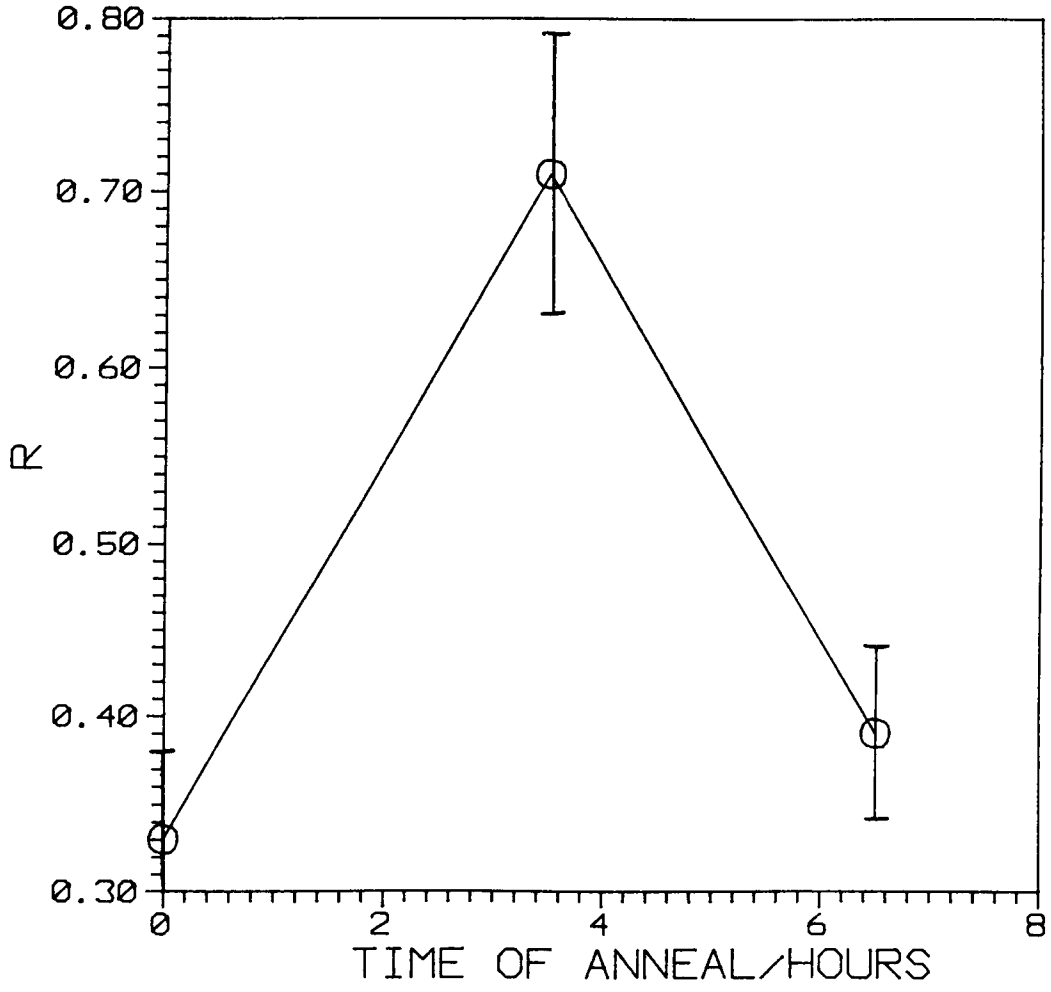


Figure 5.14. The dislocation anisotropy above the rolled aluminum as a function of time of anneal.

scatterer of sound, this is consistent with the experimental observation in the previous chapter that the dislocation density falls as the density of reflectors increases. Quantitative extrapolation of the results of chapter four is not justified because the grains constitute a three-dimensional array of scatterers which cannot be compared to a rough surface.

The change in the dislocation density per unit change in grain size is much smaller for the steel specimen than the brass. This could be due to either the intrinsic relationship between grain size and dislocation density or differences in the material properties. The properties expected to be relevant are similar in the two materials. Both have F.C.C. crystal structures and the velocities of longitudinal sound waves, 4.7 mm per μs in brass and 5.8 mm per μs in steel, are within 25% of each other. It is tempting to find the intrinsic relationship between the dislocation density and grain size by drawing a smooth curve through the data points of figure 5.10. If such extrapolation between metals could be justified, the dependence flattens off at large grain sizes. More data is required, particularly using samples of different metals but with similar grain sizes, to determine the true nature of the dependance.

The precision of the R-values found for brass (table 5.1) is too low for any quantitative statements to be made about the relationship between grain shape and dislocation anisotropy.

In the case of both brass and aluminum the dislocation density was less when measured parallel to the rolling direction

than when measured perpendicular to this. That is, all R values are less than unity. Statistically, this means that the average direction of each line segment of the tangle of dislocations is directed, to some extent towards the rolling direction. This anisotropy mimics the microstructure insomuch as grains and inclusions will be strung out into the rolling direction in a similar way. This contradicts the conclusion that a coarser microstructure generates a higher dislocation density. If measured along the rolling direction, the apparent grain size is larger yet the dislocation density is smaller. This illustrates the need for a theoretical model of the sound scattering.

As the aluminum, in its "as-received" state, is annealed its hardness falls over the first six hours (figure 5.11). This is evidence that the expected recovery and recrystallization processes have taken place. The overall dislocation density shows an increase over the 30 hour period which could, given the results for the other two metals, be associated with grain growth.

The dislocation densities measured above the more heavily rolled aluminum are around a factor of five lower than those for the as-received aluminum. The anisotropy of dislocations observed for this plate in the "as-rolled" condition is twice that observed for the as-received plate. Both these results can be explained by the production of a finer scale and more anisotropic structure by heavy rolling. Care must be taken in comparing data from the two aluminum samples because, making measurements at the standard

time of flight involved required a signal that had made multiple reflections from the faces of the thinner specimen.

Although the absolute dislocation densities behave quite differently in the two tests, their R values both show a similar peak within the first six hours of the anneal. This rise and fall in isotropy could be explained by a form of abnormal grain growth often observed in aluminum alloys [HATCH 1984]. Initially the recrystallized grains are small and equiaxed. But, the metal contains many inclusions laying in bands orientated towards the rolling direction. As the anneal continues, the growth of these new grains is impeded by these inclusions more strongly if their growth is normal to the rolling direction than if it is parallel to the rolling direction. This results in a reappearance of an anisotropic grain structure. As the new grains form, R is large but decreases as they grow along the rolling direction.

CHAPTER 6

ULTRASONIC DISLOCATIONS AND THE GROWTH OF CORROSION PITS

Introduction

In this research area the value of dislocations as well defined markers in a wave field can be exploited in a manner akin to the geophysical experiments of Walford *et al.* If dislocations are observed in the sound reflected from an object that is evolving over time, then the dislocation lines will move. As the location of dislocation lines can be measured with a precision an order of magnitude less than the wavelength, they offer a sensitive means of observing the temporal evolution of the system. It will be demonstrated that the growth of corrosion pits on a stainless steel surface can be measured in this way.

Consider a polished stainless steel specimen immersed in an aqueous solution of an electrolyte known to generate localized corrosion. The specimen is probed using pulses of sound from the transducer, set with its focal point above its surface, as is illustrated schematically in figure 6.1. If there is a corrosion pit on the surface, interference between waves reflected from various parts of the pit and those reflected from the smooth surface will generate dislocations in the returning signal. Because the situation possesses cylindrical symmetry these dislocations should be circular loops. As the pit grows the dimensions of the dislocation loops should change.

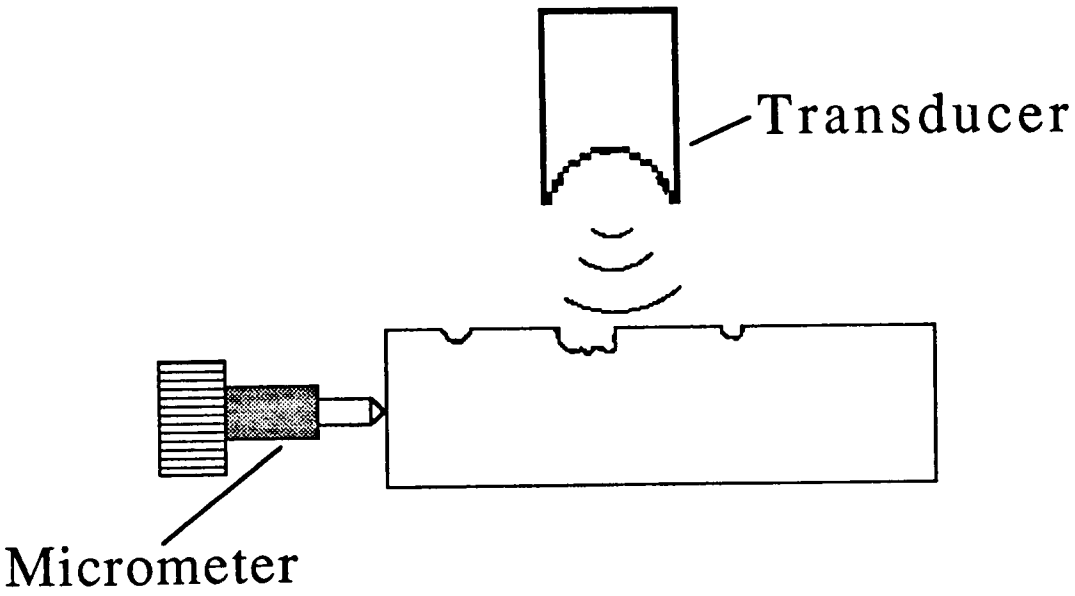


Figure 6.1. Schematic diagram of the experimental arrangement.

The experimental procedure was to immerse a specimen containing pits in various concentrations of iron(III)chloride and then observe the time evolution of the dislocation loops above them.

Experimental Procedure

A stainless steel coupon that had a polished surface containing corrosion pits, produced during and electrochemical experiment, was donated by Dr. In-Seop Lee. This specimen was glued to the bottom of a beaker into which was placed in a solution of .8% ferric chloride in distilled water (Solution A). The beaker and immersed sample were then attached to the X-Y translation stage and the 20 MHz ultrasonic transducer scanned above the specimen surface. The transducer was operated in pulse/echo mode and the returning signals observed on the oscilloscope. The height of the transducer was adjusted such that the beginning of the echo signal was 18 μs after the pulse. This corresponds to the focal point of the transducer being 0.7 mm above the specimen surface. By observation of the time of flight of the echo signal the inclination of the specimen was carefully adjusted until its surface was parallel to the plane of motion of the stage. Once set up correctly, neither the transducer nor the specimen were moved.

The X-Y plane was systematically searched for dislocations in the echo signal. Once a dislocation was found its locus was plotted, the "X" and "Y" coordinates being defined by the readings on the

micrometers. If reasonably circular, that is, its largest diameter was no greater than twice the smallest diameter, the center coordinates of the loop were recorded. This was done until nine such dislocation loops were found. Once the center point of the loop was known, its diameter could be measured by moving out from the center and measuring the diameter in both the X and Y directions. The average of these diameters was taken. The precision with which the dislocations could be located was limited only by the one micron resolution of the micrometers.

The specimen was left in solution, at room temperature, and the nine dislocation diameters were measured at about four hour intervals. In order to protect the transducer from the corrosion, enough solution was removed from the beaker in between readings that it was above the surface of the liquid. This liquid was stored separately and then returned to the beaker when it was time to measure the loop diameters. Any changes in the dimensions of the dislocation loops were monitored in this way over period of several days.

This procedure was repeated using solutions of 2.6% and 5.3% ferric chloride (solutions B and C, respectively).

The effect of fluctuations in the speed of sound, and thus, variations in the wavelength on the observed loop diameters was taken into account by performing a control experiment. The ferric chloride was replaced by sodium hydroxide solutions of varying concentrations and the loop diameters were measured. The speed of

sound increases with concentration allowing the wavelength to be varied even though the transducer produces a pulse at a fixed central frequency. For each concentration the loop diameter was measured and plotted as a function of signal time of flight which is inversely proportional to the sound velocity. Sodium hydroxide was chosen because it would not effect the sample. The relationship between sound velocity and time of flight was used to correct the data for the observed variations in the sound speed.

In order to establish a relationship between the dislocation loops and the actual dimensions of the pits the apparatus was set up with the addition of a micrometer adjustment of the transducer height. The loop diameter was measured as a function of time of flight (now varied by changing the distance of the transducer from the sample) for several pits. So that these pits could be identified a map was made of the pits on the sample using a travelling microscope arrangement and the pattern of pits, observed ultrasonically, searched for. Once identified, the widths of the pits were measured using an optical microscope and their depths measured by focussing onto the bottom of the pit and then onto the surface.

In order to measure the actual rate of pit growth the specimen was left, at room temperature, in the 5.3% ferric chloride solution for 15 days. The measurement of the depths and widths of the nine pits that had been identified was then repeated.

Results

The variation in time in the dimensions of the nine dislocation loops, when immersed in solution A, is shown as a function of time in figure 6.2. The dashed line represents the average of these loop diameters. It is important to notice that the typical loop size, 150 microns, is only twice the wavelength of 74 microns. The dislocations allow observations of variations on a scale at least an order of magnitude finer than the wavelength.

The result of the control experiment to determine the dependence of the dislocation loop diameter on the time of flight and thus the speed of sound are graphed in figure 6.3. The average slope calculated from these curves was 195 μm per μs. This figure was used to correct the diameter measurements of figure 6.2. Figure 6.4 shows the temporal variation in time of flight averaged over the nine pits. As indicated, the observed change in the speed of sound can be accounted for by a 0.5 Kelvin change in the temperature. Graph 6.3 was used to calculate loop diameter expected at a reference time of flight chosen to be 18 microseconds. The evolution of the average of this corrected loop diameter is graphed in figure 6.5. The observed rising trend is fits a straight line of gradient 0.06 microns per hour.

The experiment was repeated in solution B and the change in the similarly corrected loop diameter is given in figure 6.6. When comparing figure 6.5 to figure 6.6 one should note the four fold compression of the Y-axis and the compression of the time axis. The

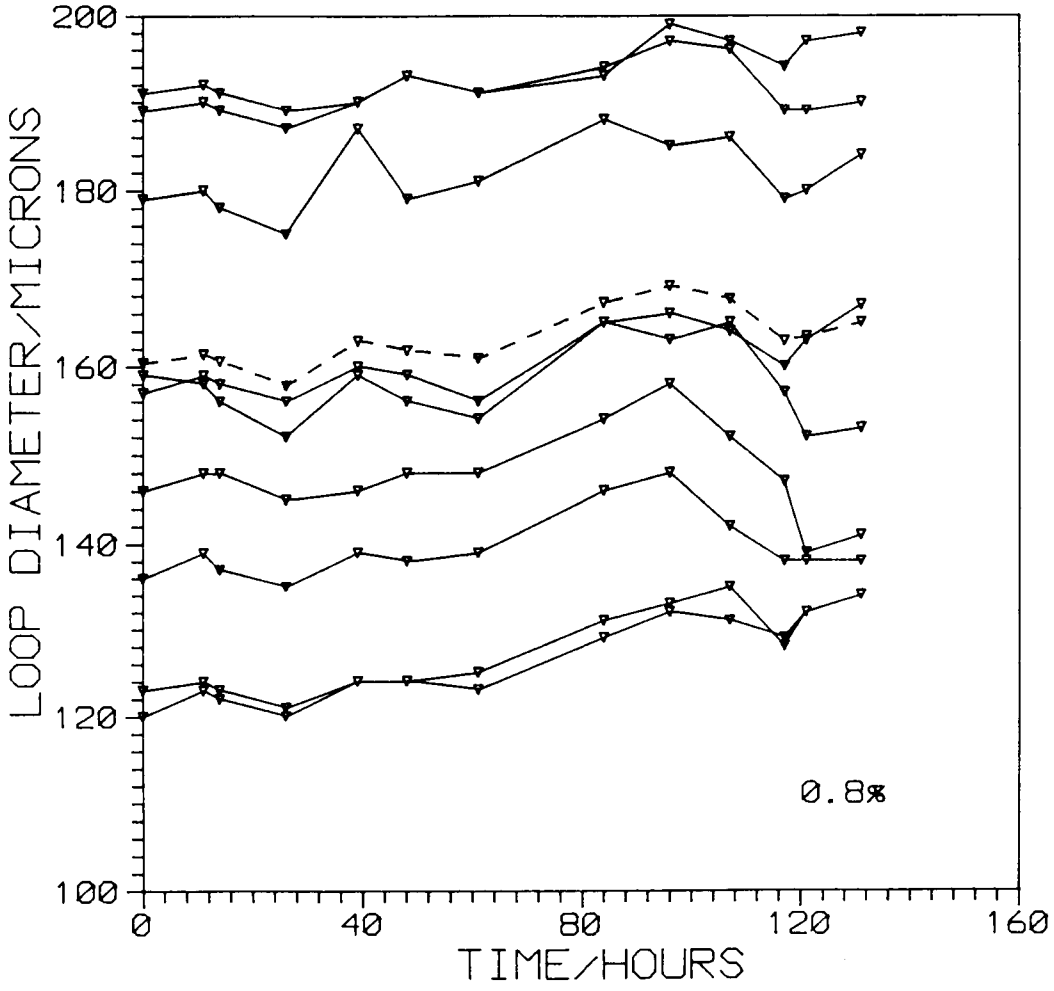


Figure 6.2. The evolution of nine loop diameters when placed in solution A.

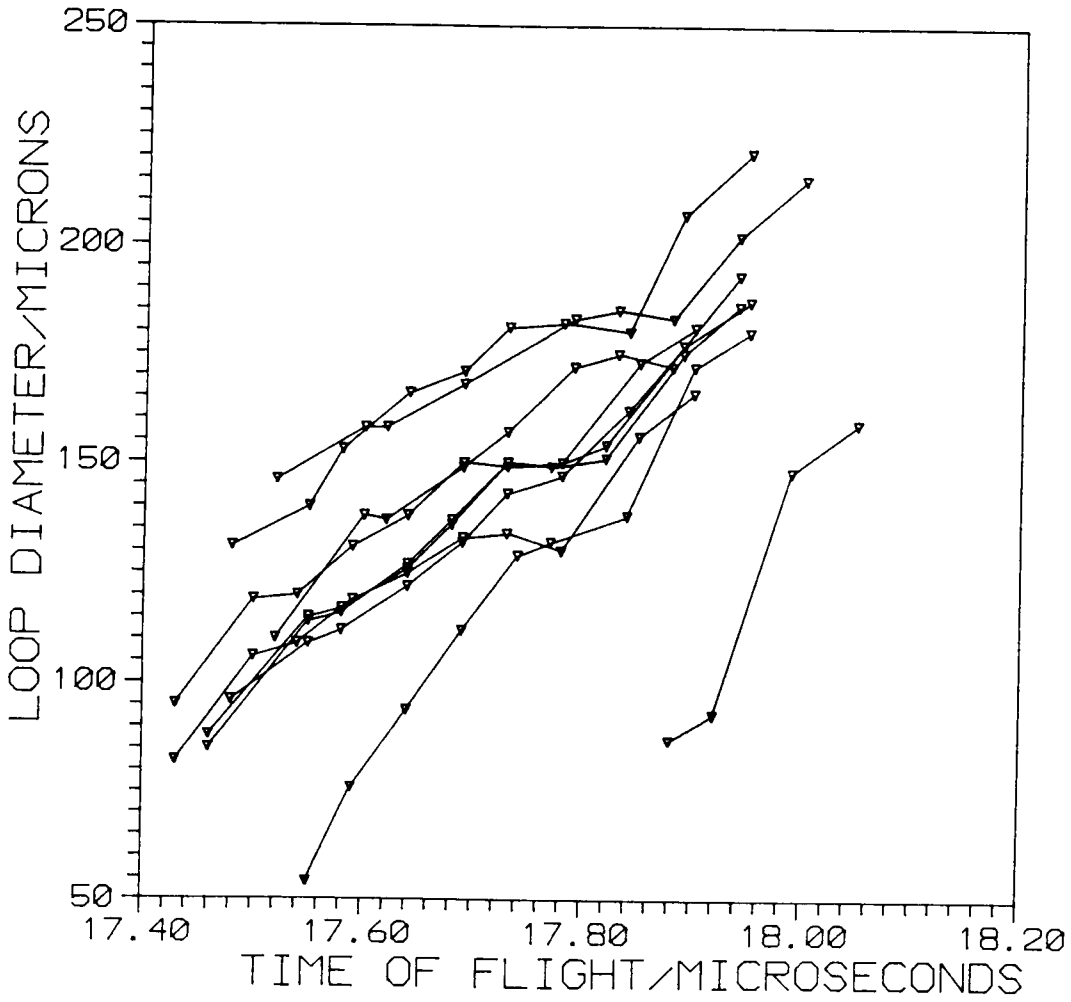


Figure 6.3. The relationship between loop diameter and time of flight.

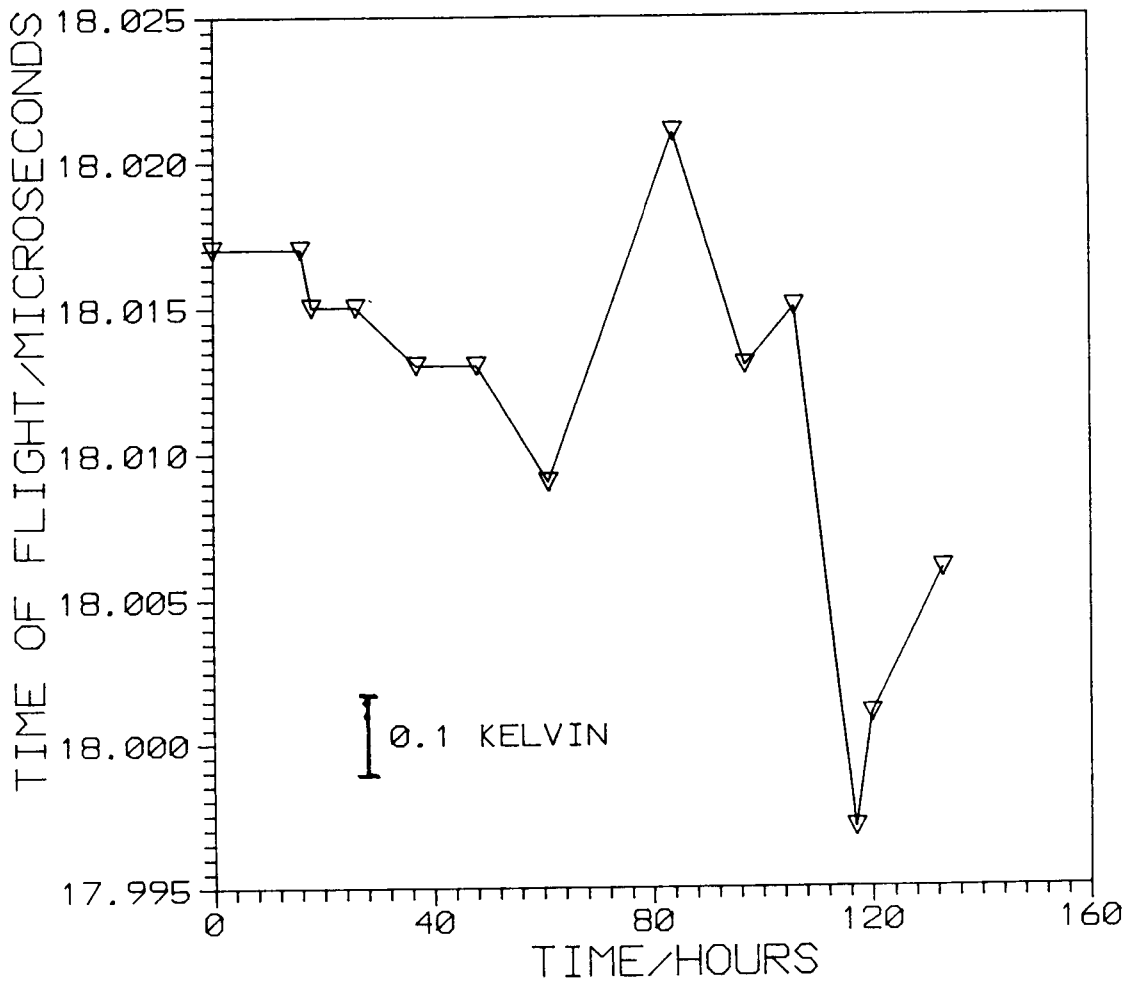


Figure 6.4. The variation of the average time of flight with time.

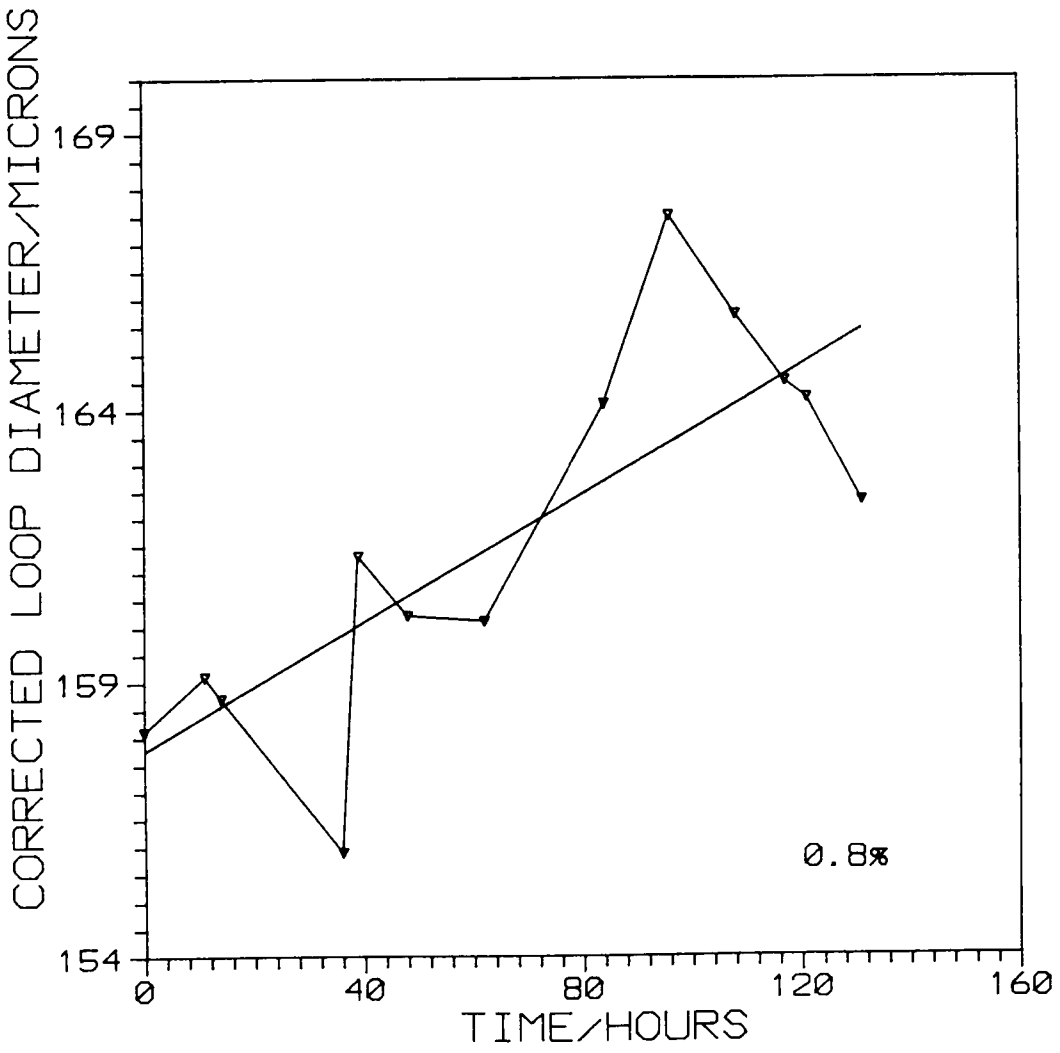


Figure 6.5. The evolution of the average loop diameter when placed in solution A.

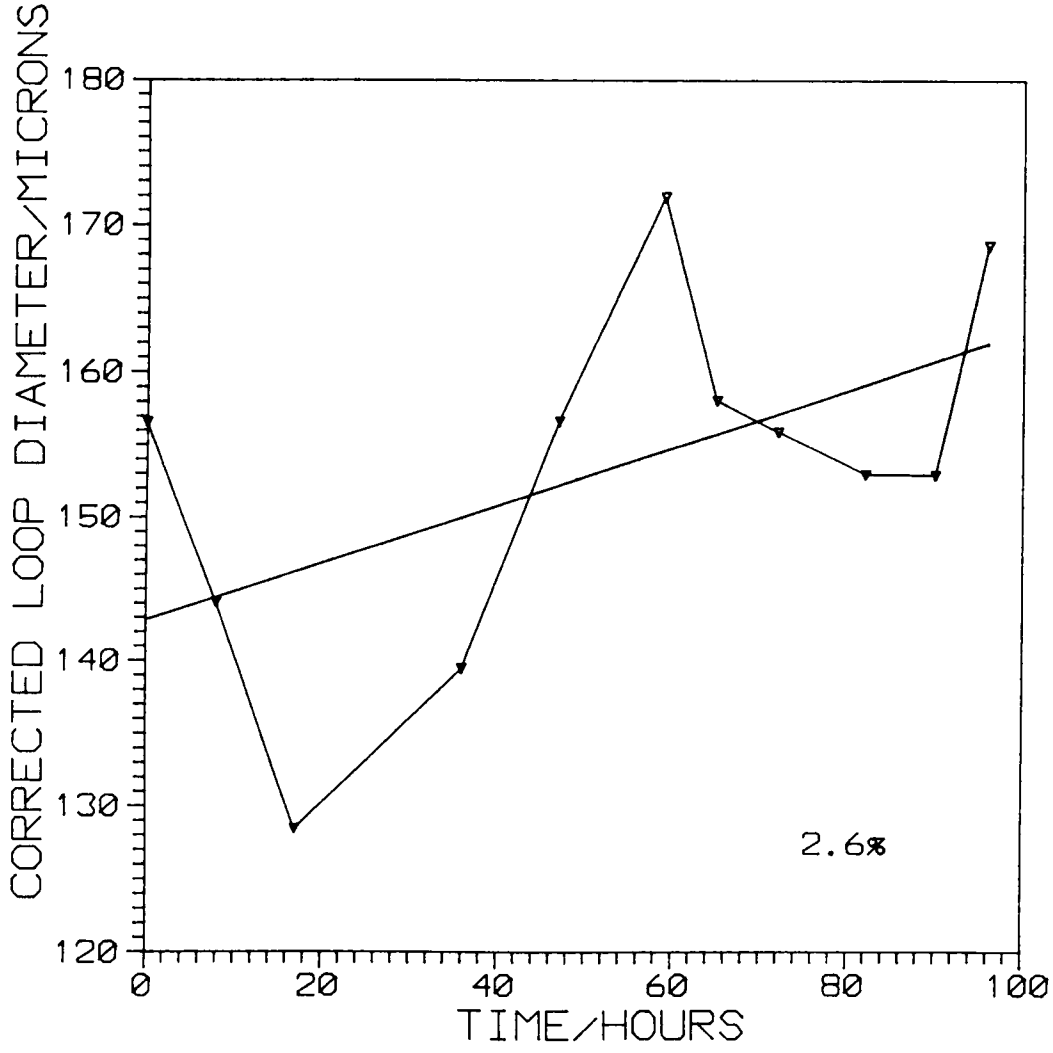


Figure 6.6. The evolution of the average loop diameter when placed in solution B.

straight line describing this data has a slope of 0.20 microns per hour.

In the more concentrated solution C, the loops expand as shown in figure 6.7. For comparison, the upper and lower dashed straight lines are those calculated to fit the solution A and solution B results respectively. The rate of increase in loop size measured in this case was .82 microns per hour. Figure 6.8 summarizes the above data. The extent of the error bars was estimated by plotting the extreme steepest and flattest lines that could fit the data in the loop diameter/time graphs.

The dependence of loop diameter on the distance of the transducer from the sample is shown on figure 6.9. The labels on the axes of figures 6.9 and 6.3 are identical but, in the case of 6.9, the change in time of flight is due to changes in the distance to the specimen, not changes in the speed of sound.

Figures 6.10 and 6.11 show the relationship between the loop diameter and the pit diameter and pit depth for nine different pits. No clear correlation between either of these quantities and the loop diameter can be seen. This is an indication of how difficult it is to construct a theory of the sound field produced by irregularly shaped corrosion pits.

The relative change in the diameters and depths of the nine test pits after 15 days in 5.6% ferric chloride is shown in figure 6.12. The horizontal axis of this graph serves merely to separate the data points and has no significance.

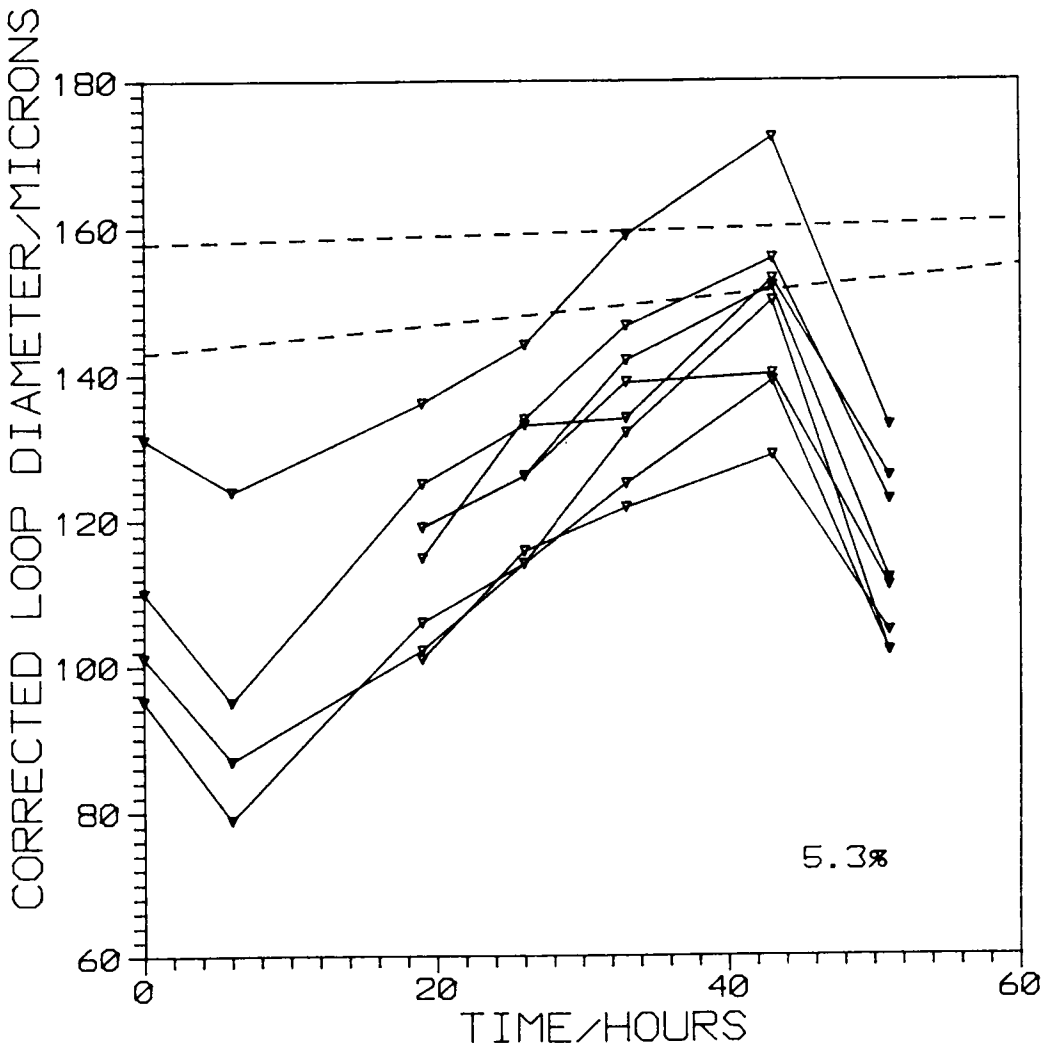


Figure 6.7. The evolution of the loop diameter when placed in solution C.

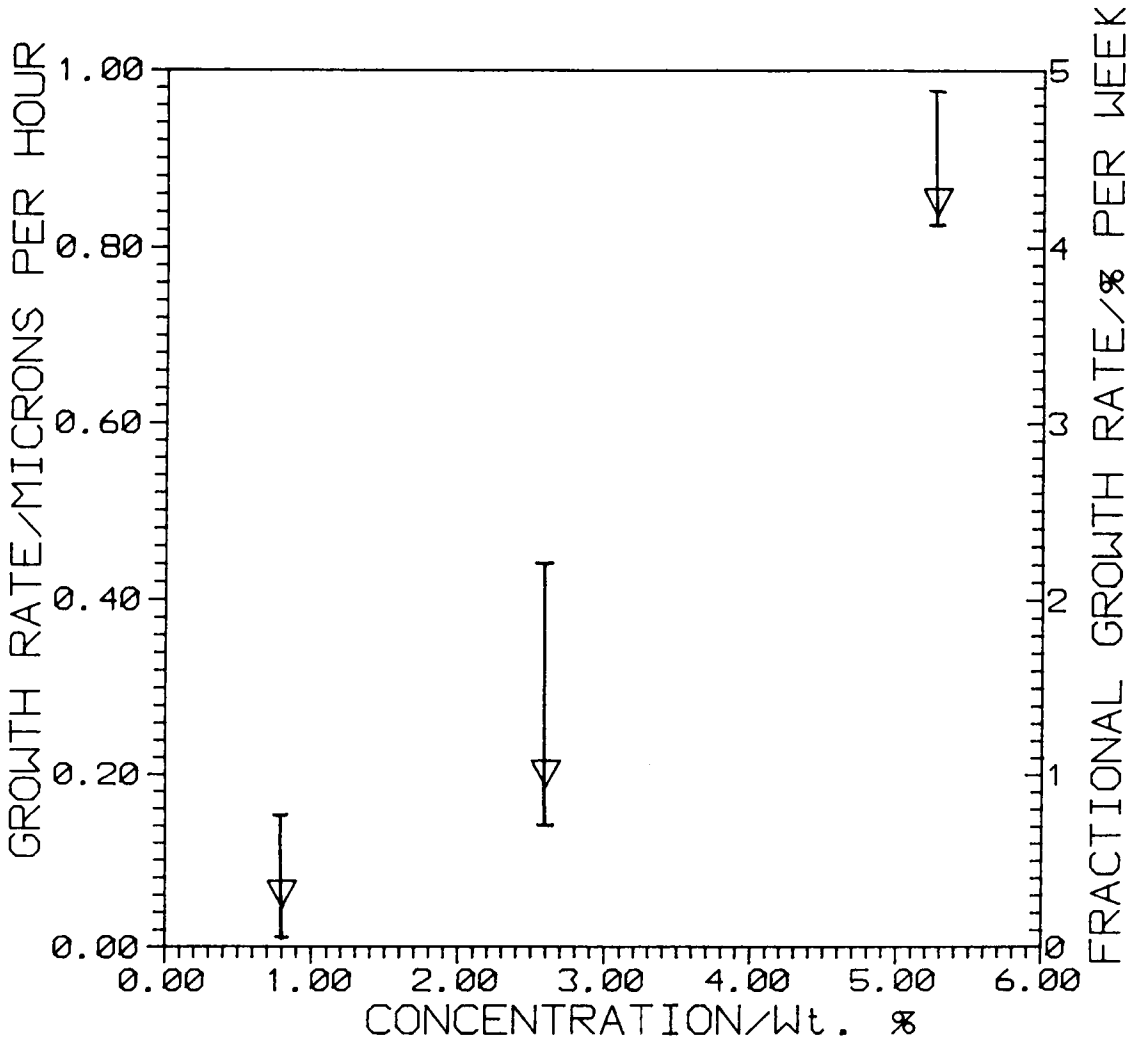


Figure 6.8. The loop growth rate as a function of concentration.

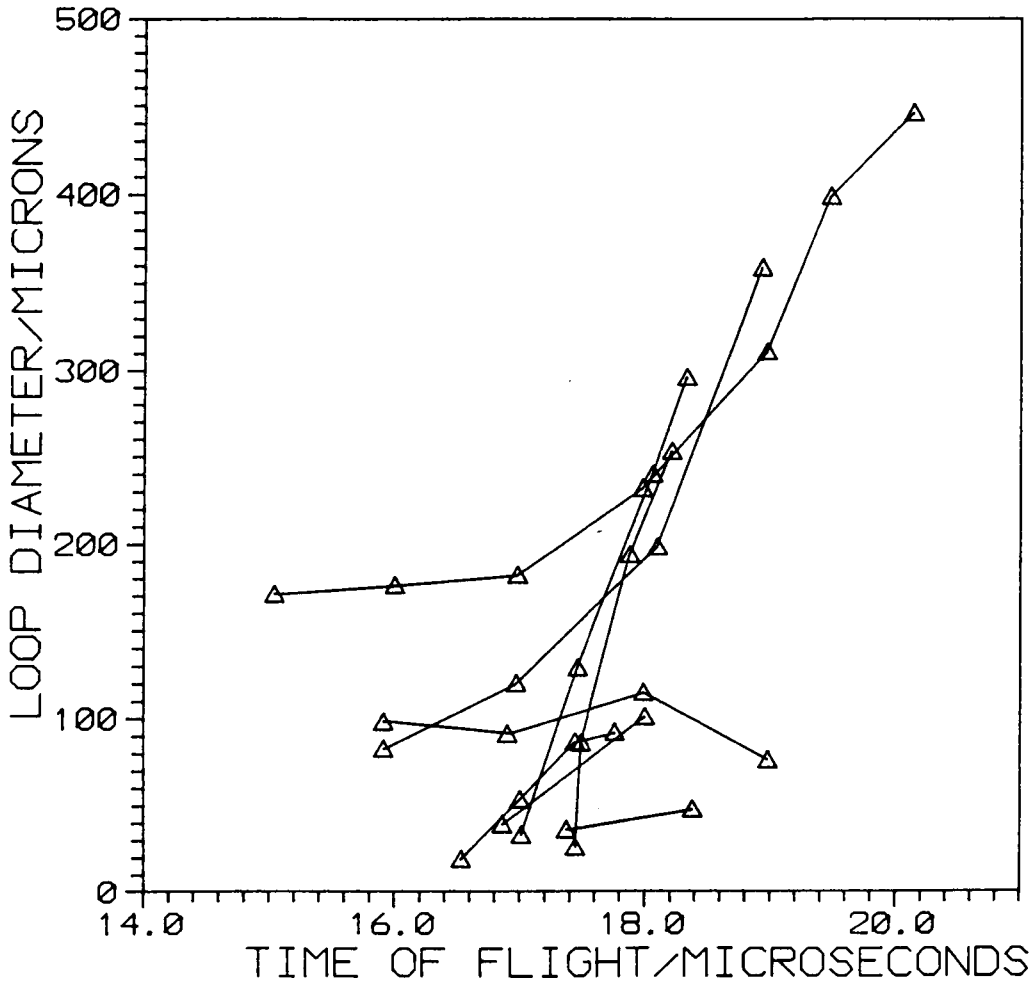


Figure 6.9. The relationship between the loop diameter and the distance from the sample, measured for several different pits.

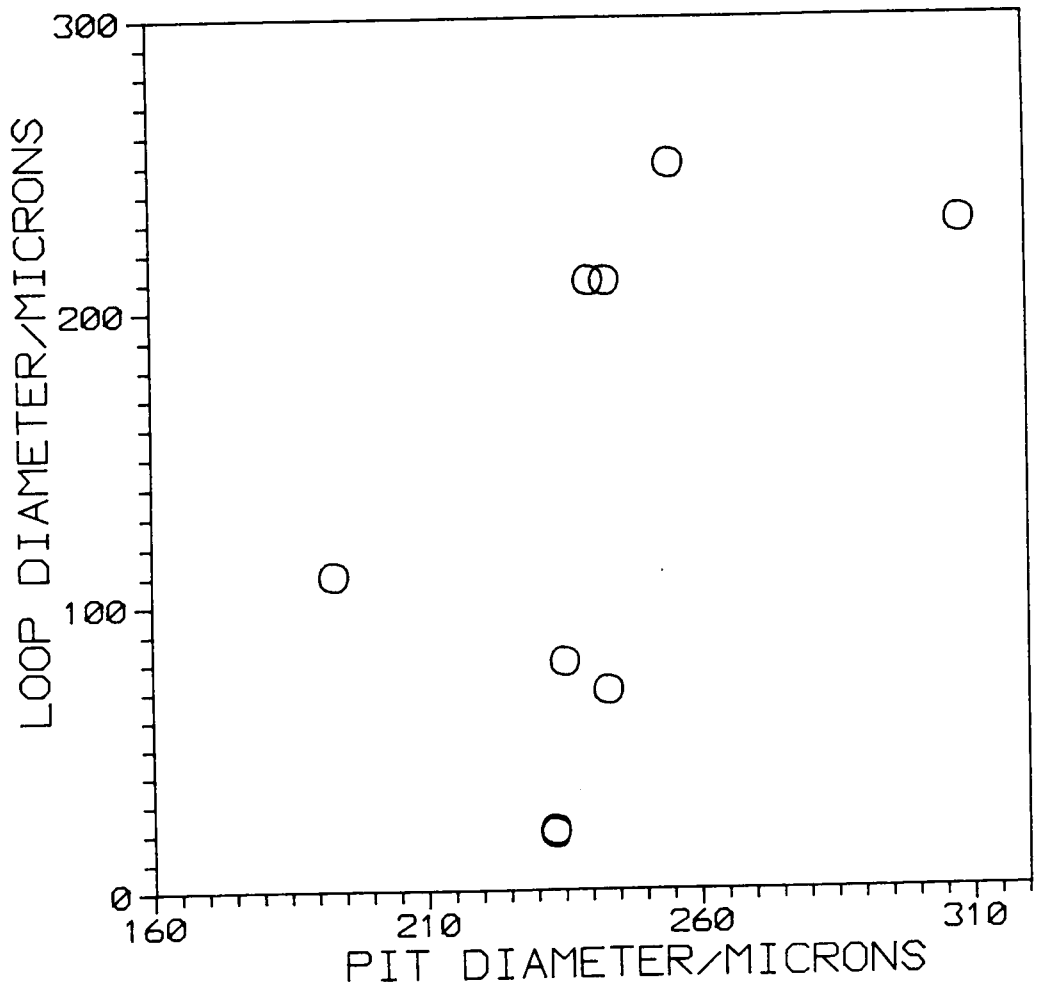


Figure 6.10. The relationship between loop diameter and pit diameter.

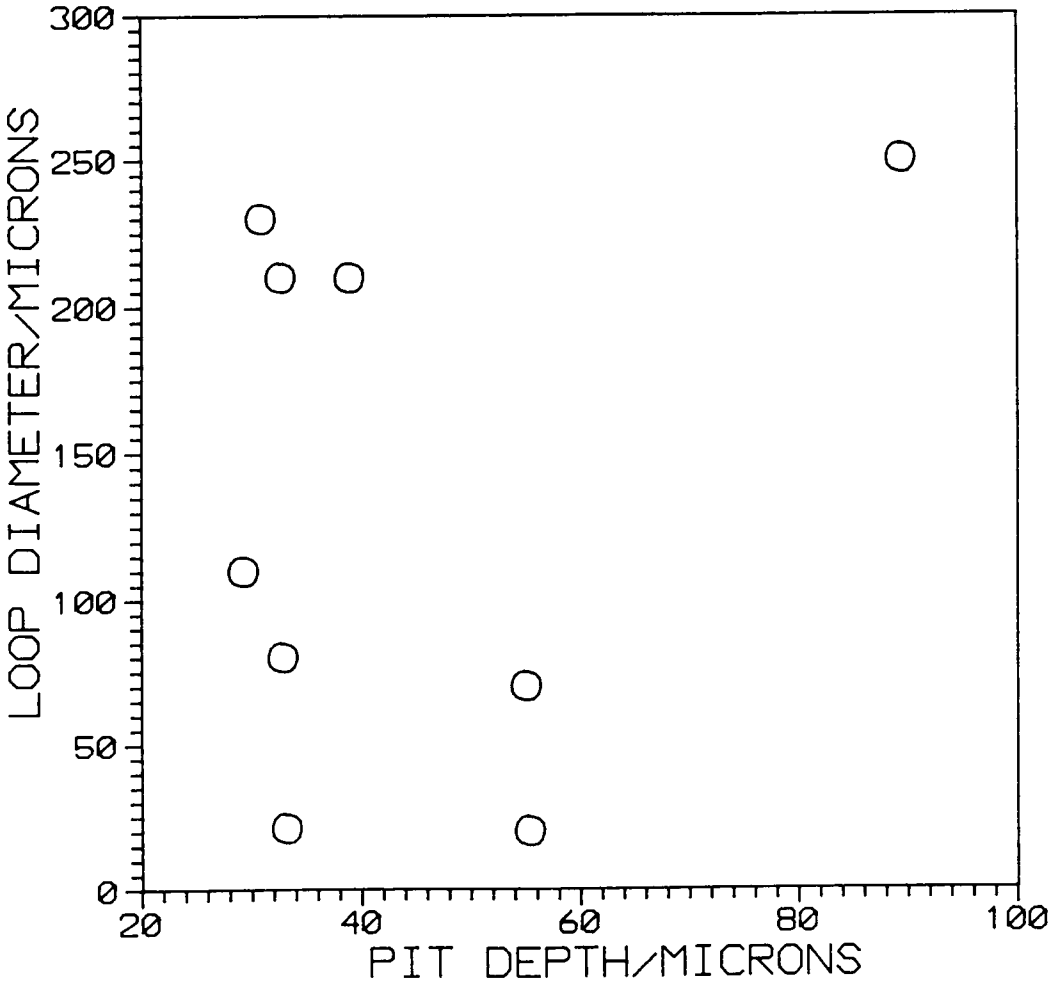


Figure 6.11. The relationship between loop diameter and pit depth.

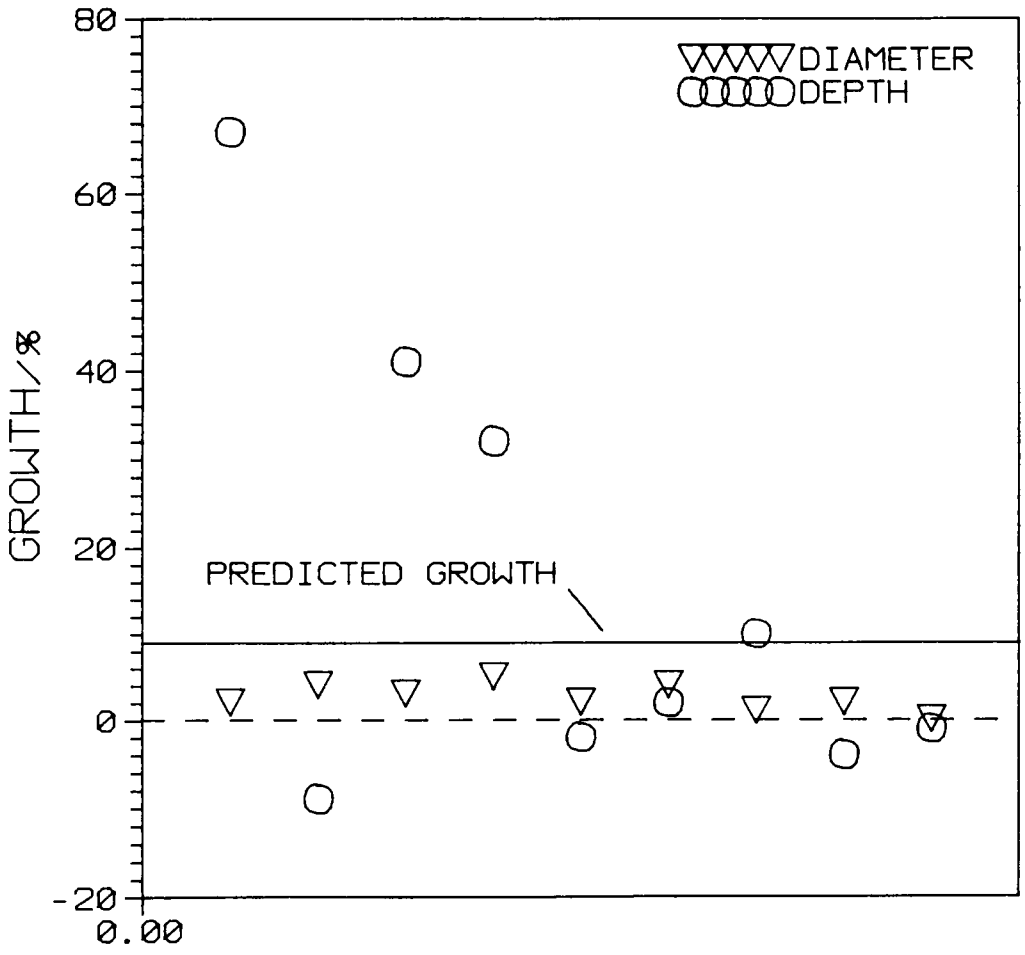


Figure 6.12. The relative changes in pit dimensions after 15 days immersion on solution C.

Analysis

No direct acoustic model relating the size of the dislocation loops to the dimensions of the pit producing them could be found. But, by consideration of the normalization of the problem, a theory could be constructed relating the relative size of the dislocation loop to the size of the pit under the assumption that its shape remains constant.

Consider a transducer being scanned a distance, Z, above a pit of constant shape whose size is represented by r (as the shape of the pit is constant the actual dimension r represents is immaterial). The wavelength is λ, and a dislocation loop of diameter, D, is observed. D is a function of λ, Z and r.

$$D = D(\lambda,Z,r) \qquad 6.1$$

If these four quantities were all multiplied by a scalar factor, ρ, then the diffraction problem will be exactly the same but expanded by this factor. As we are dealing with a linear problem, this implies that the function, $D(\lambda,Z,r)$, has the property:

$$D(\rho\lambda,\rho Z,\rho r) = \rho D(\lambda,Z,r) \qquad 6.2$$

Let the initial values of the parameters be λ_0, Z_0 and r_0. λ and Z will remain constant as r varies as a function of time. After time:

$$D = D(\lambda_0,Z_0,r) \qquad 6.3$$

applying equation 6.2:

$$D = \frac{r}{r_0} \cdot D\left(\frac{\lambda_0 r_0}{r}, \frac{z_0 r_0}{r}, r_0 \right) \qquad 6.4$$

let $\frac{r}{r_0} \equiv \rho$

$$D = \rho \cdot D\left(\frac{\lambda_0}{\rho}, \frac{Z_0}{\rho}, r_0 \right) \qquad 6.5$$

Performing a first order Taylor expansion on D:

$$D(\lambda_0+\delta\lambda, Z_0+\delta Z, r_0) = D(\lambda_0, Z_0, r_0) + \delta\lambda \cdot \frac{\partial D}{\partial \lambda} + \delta Z \cdot \frac{\partial D}{\partial Z} \qquad 6.6$$

Here:

$$\delta\lambda = \lambda - \lambda_0$$

and the differentials are evaluated at, $\lambda=\lambda_0$ and $Z=Z_0$.

But, in equation 6.5:

$$\lambda = \frac{\lambda_0}{\rho} \qquad 6.7$$

$$\Rightarrow \delta\lambda = \lambda_0 \cdot \left(\frac{1}{\rho} - 1 \right) \qquad 6.8$$

Substituting into 6.6:

$$D - D_0 = \left(\frac{1}{\rho} - 1 \right) \left(\lambda_0 \cdot \frac{\partial D}{\partial \lambda} + Z_0 \cdot \frac{\partial D}{\partial Z} \right) \qquad 6.9$$

where:

$$D_0 = D(\lambda_0, Z_0, r_0) \qquad 6.10$$

and

$$D = D(\lambda, Z, r_0) \qquad 6.11$$

Let:

$$\kappa = \left(\lambda_0 \cdot \frac{\partial D}{\partial \lambda} + Z_0 \cdot \frac{\partial D}{\partial Z}\right) \qquad 6.12$$

Equation 6.9 can be rearranged to yield an expression for ρ:

$$\rho = \frac{\kappa}{D - D_0 + \kappa} \qquad 6.13$$

The expansion of the pit is now known in terms of the first derivatives of the loop diameter with respect to its distance from the specimen and the wavelength, both of which can be experimentally determined.

The derivative with respect to wavelength was calculated from the slope of the data presented in figure 6.3:

$$\lambda_0 \cdot \frac{\partial D}{\partial \lambda} = -3500 \ (\pm 800) \ \mu m \qquad 6.14$$

From the data presented in figure 6.9, the derivative with respect to distance was determined:

$$Z_0 \cdot \frac{\partial D}{\partial Z} = 160 \ \mu m \qquad 6.15$$

Thus, the value of κ was found to -3300 ($\pm$800) μm. The rate of change of loop diameter with sound velocity dominates the expression for κ. Because the second term is relatively small, no estimate of its precision was necessary.

As κ is much larger than any observed change in D, equation 6.13 can be simplified using a first order binomial expansion:

$$\rho = 1 - \frac{D - D_0}{\kappa} \qquad 6.16$$

As this model is only required to be valid over relatively small time intervals the loop can be assumed to expand linearly, D can be written:

$$D = D_0 + Rt \qquad 6.17$$

where R is a constant representing the expansion rate and, t, is the time.

$$\Rightarrow \rho = 1 - \frac{Rt}{\kappa} \qquad 6.18$$

$$\Rightarrow \frac{d\rho}{dt} = \frac{R}{\kappa} \qquad 6.19$$

Substituting in the numerical value of κ the final expression for the fraction growth rate of the pit is:

$$\frac{d\rho}{dt} = R \times 3.0(\pm 0.7) \times 10^{-4} \text{ (hours)}^{-1} \qquad 6.20$$

Where, R, is expressed in μm per hour. A more convenient unit is percent growth per week. Scaling equation 6.20:

$$\frac{d\rho}{dt} = R \times 5.0(\pm 1.2)\ \%\ \text{per week} \qquad 6.21$$

The growth rate predicted by this theory for the experimental data is given by the right hand Y-axis of figure 6.8. The maximum growth rate observed was 4.3(±1.0) % per week.

Discussion

The results establish that there is a link between the rate of change of dislocation loop diameter and the concentration of electrolyte. This is most clearly illustrated by figure 6.7 where the growth rate found in the most concentrated solution is clearly larger than that found in the other two. The rise in growth rate with concentration seen between the two more dilute solutions is close to the experimental error but still significant. The non-linear appearance of the data in figure 6.7 may be due to a transition to a less passive corrosion behavior occurring at a concentration in between three and five percent chloride.

A possible alternative explanation for the results is that the ultrasonic transducer was attacked by the electrolyte during the test causing its characteristics, and thus, the dislocation loop diameter to change. This is unlikely because the transducer only spent a small fraction of the total duration of each test immersed in the electrolyte. This possibility could be eliminated in future

experiments by insulating the transducer from the electrolyte by some form of protective barrier.

The scatter graphs, figures 6.10 and 6.11, illustrate the difficulty in creating a model of the acoustic field generated by pits of various shapes and dimensions. Any search for such a theory will be further hampered by the large concentration gradients, and thus, sound velocity gradients near the pit.

The semi-empirical analysis based of the assumption that the pit remains the same shape as it grows was able to find a connection between the dislocation and the pit. Although the scatter of the data in figure 6.12 is vast, the growth rate is of the correct order of magnitude. The dubious nature of the assumption of constant shape is illustrated by the fact that, for most of the pits, the change in depth is much larger than the change in width.

The constant shape theory predicts that a one percent change in the dimensions of the dislocation will result in a readily observable, 34 μm change in the loop diameter. The root of this sensitivity can be thought of as being the is the steep dependence of the loop diameter on the speed of sound (figure 6.3).

The experiments presented in this chapter confirm the utility of wave field dislocations as markers in the wave field that can detect small changes in that field.

CHAPTER 7

CAUSTICS AND ULTRASONIC IMAGING

Introduction

The fact that caustics are surfaces of high wave intensity can be exploited in an ultrasonic imaging system.

In order to see how this can be achieved consider a point source of sound rays at the edge of a cylindrical reflecting dish the whole system being immersed in water or some other acoustic coupling medium. As shown in figure 7.1, after reflection from the surface of the cylinder the rays converge to form a caustic. The sound rays are concentrated at this caustic implying that the intensity of the field near it should be high. Consider that the transducer is a coincident source and receiver. If a pulse is emitted the relative intensity of the echoes received will be large if emanating from an object near the caustic. If, as shown schematically in figure 7.2, the caustic intersects a specimen and the echoes returning to the transducer observed as a function of time, all the signals can be assumed to come from the section of the specimen lying on the caustic. As the locus of the caustic and the time taken for the pulse of sound to reach each point on it can be calculated, the coordinates of the piece of the specimen responsible for the echo can be determined. If the object is moved across the caustic its image can be built up from the amplitudes and times of flight of the various reflected signals. (The component of an object

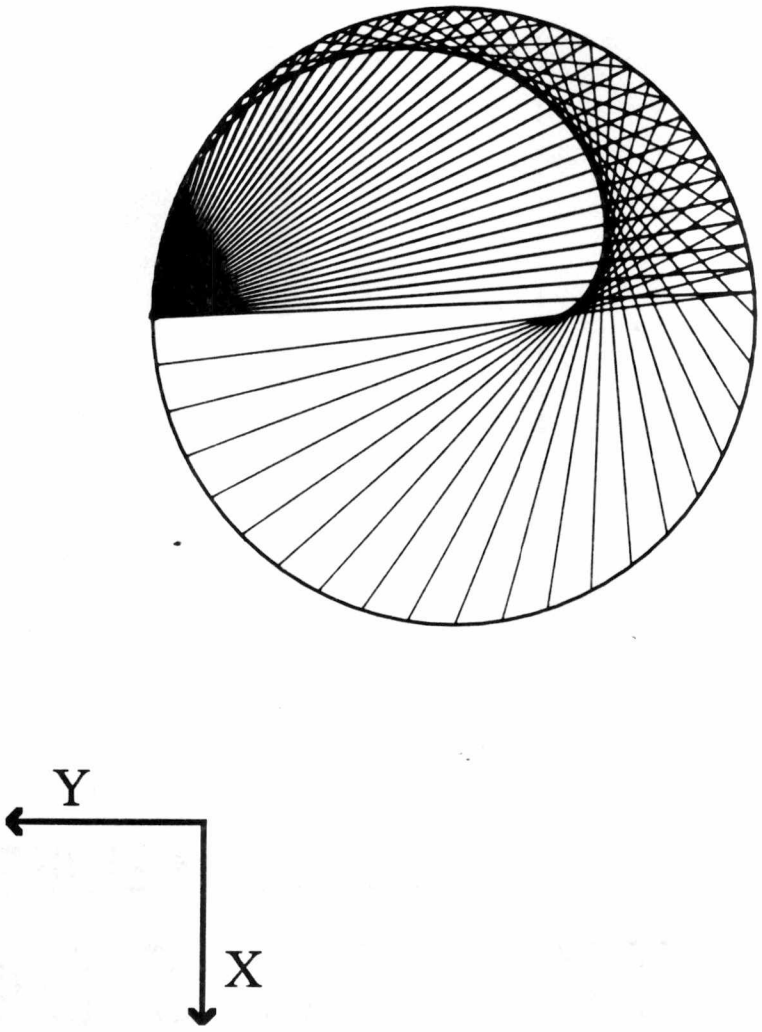


Figure 7.1. Ray diagram showing the formation of a caustic by reflection from a cylindrical dish.

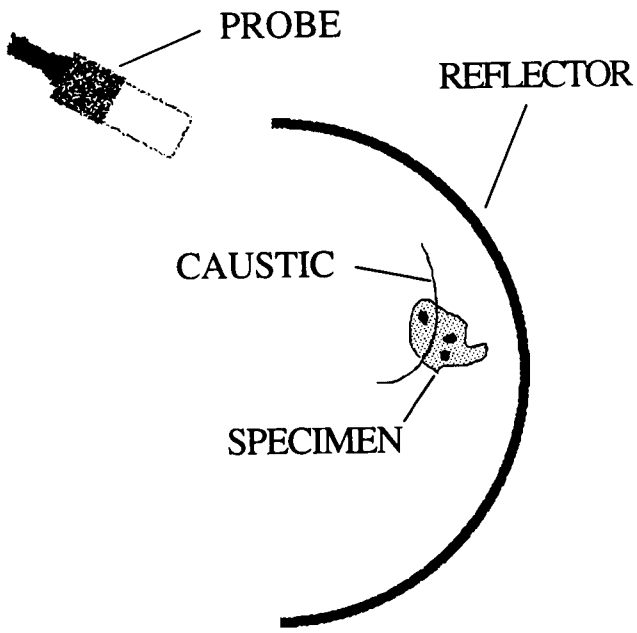


Figure 7.2. Schematic diagram of the imaging system.

point parallel to the axis of the reflector can not be determined implying that the image formed will be of the same plan view depicted in figure 7.2.)

This imaging technique has been demonstrated qualitatively [BREWSTER 1989] and the work described below constitutes a more quantitative study of the system. This consists of mapping the wave field in the vicinity of the caustic in order to measure the dimensions of the diffraction field around it. This permits calculation of the resolution and depth of field of the system. Rather than attempting the form images of relatively complex objects, the emphasis is on imaging simple arrays of points and planes with a view to obtaining quantitative information on the spatial and temporal resolution of the system and any false images that may occur.

Experimental Procedure

The arrangement described above was realized experimentally using 90 degree section of a cylindrical stainless steel pipe with a nominal inner radius of 30 mm as the reflecting dish and the focal point of the 20 MHz, ultrasonic transducer described in previous chapters as the source of sound. To ensure specular reflection of the sound the inner surface of the pipe was polished to a 600 grit finish. The combination reflector and transducer were immersed in water.

The sound field was explored using a steel wire, of nominal diameter 0.13 mm, held taught by a spring and aligned parallel to the axis of the cylinder to approximate a point object. The wire was translated about the image plane and its position measured using the X-Y translation stage described in chapter four. The ultrasonic signals were generated and the returning signals amplified by the pulser/receiver. The echoes were observed on the oscilloscope.

Three model objects were made to evaluate image formation capability. Object "A" consisted of four wires of different lengths one end of each being set in epoxy resin. The task of the imaging system was to determine the relative positions of the ends of the wires. To improve the strength of reflection the ends of the wires were bent double. Object "B" consisted of similar wires but with both ends set in epoxy. The ends of the wires to be imaged were about 2 mm below a smooth flat surface of the resin. Object "C" consisted of three, approximately parallel metal plates set in epoxy, again a few millimeters from a flat surface. Objects "B" and "C" were designed to demonstrate the ability to image features within the bulk of a specimen.

In order to form an image the specimen was mounted on the translation stage and moved to a position near the most strongly illuminated part of the caustic. In the cases of objects "B" and "C" the object was oriented such that its surface is normal to the incident direction of the rays on the caustic. This was done by manipulating the object until the amplitude of the signal from the

front face was a maximum. The specimen was then translated in the direction normal to the caustic and the signals on the oscilloscope screen were recorded as a function of position. To facilitate the manual digitization of the reflected signal it was divided up according to each of the distinct peaks that were visible. The time of flight corresponding to the maximum amplitude of each, along with its width were recorded. The imaging software (listed in appendix B) was designed to reconstruct the rest of the signal given this information. The contour maps of the images were generated using "SAS/GRAPH".

Results

As the test wire was scanned across the caustic from the shadow side to the illuminated side a distinct signal was seen to sharply appear on the oscilloscope screen. This could be distinguished from the echo due to sound being reflected directly from the wire, without reflection from the dish, by reference to its time of flight.

Let the directions "X" and "Y" be, respectively, defined as those vertical and horizontal in figure 7.1. The origin of the coordinate system defining the position of the test wire is arbitrary but fixed throughout the subsequent measurements. For a fixed value of X the Y-position of the wire is varied as it crosses the caustic. The Y-value at the location where the amplitude of the reflected signal is a maximum and the places where it is half this

maximum is shown for various values of X in figure 7.3. (Here the amplitude is defined as the voltage difference between the highest peak and the lowest trough of the oscilloscope signal.) The curve of the caustic is visible on this graph. Note that the X-scale is compressed relative to the Y-scale. The curvature of the caustic is quite small which suggests that it be approximated by a straight line greatly simplifying the imaging algorithm. Qualitatively, it can be seen that the caustic is very long relative to its width.

The Y-component of the width at half maximum of the caustic as a function of X is shown in figure 7.4. It can be seen to be quite constant along the length of the scan at a value of 0.42 mm. If we assume that two objects can be resolved when the maximum of one coincides with the half maximum of the other then the resolution of this system is half the width of the caustic. Therefore the measured resolution on the order of 0.2 mm.

At a value of X around 6 mm the width of the caustic greatly increases. This is because the beam of the transducer no longer illuminates the caustic and the increase in amplitude is solely due to the wire crossing into the beam.

The length of the section of caustic illuminated can be measured by plotting the maximum amplitude as a function of X (figure 7.5). The width at half maximum of this profile is 10.5 mm, which gives a value of the length to width ratio of the caustic of 25.

Figure 7.6 gives a more detailed picture of the amplitude profile across the caustic. The amplitude varies smoothly on the

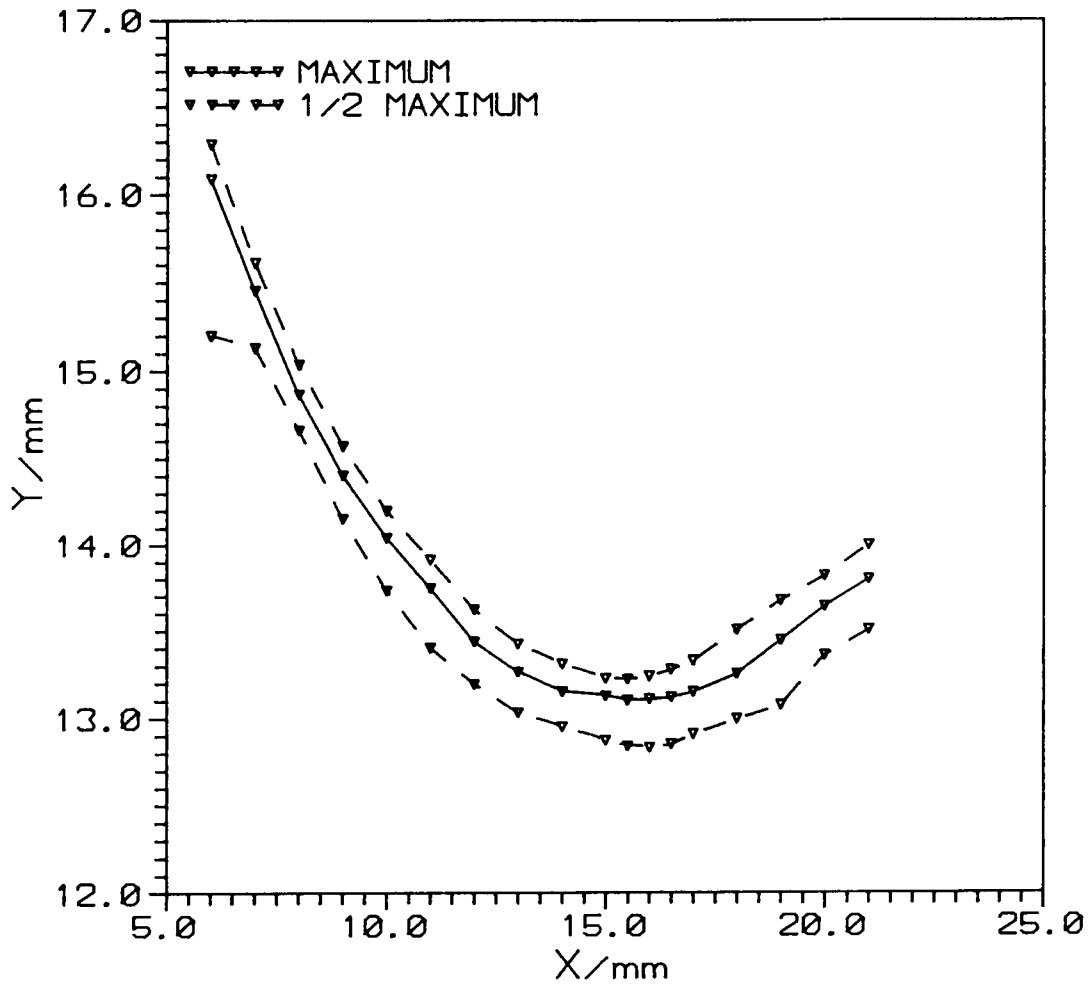


Figure 7.3. Loci of the maxima and half-maxima in the signal from the caustic.

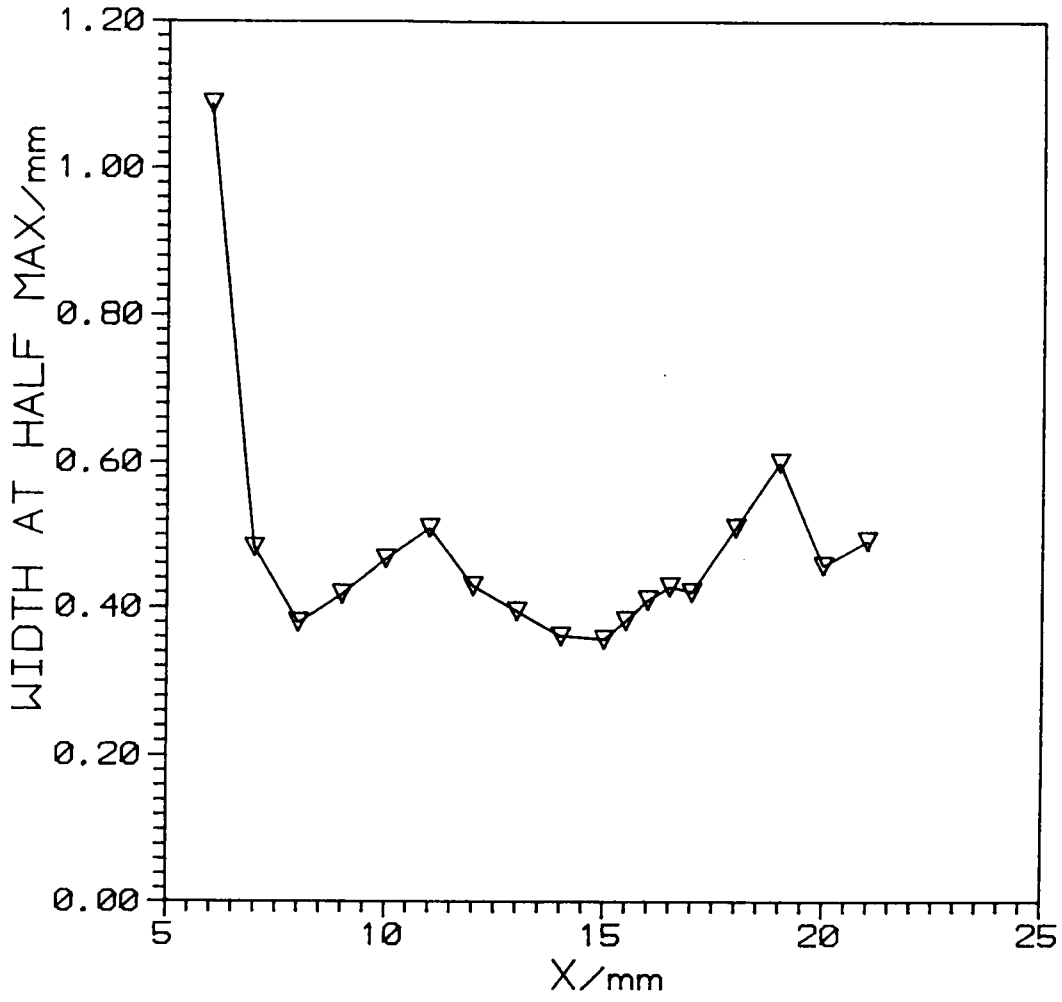


Figure 7.4. The variation in the width of the caustic along its length.

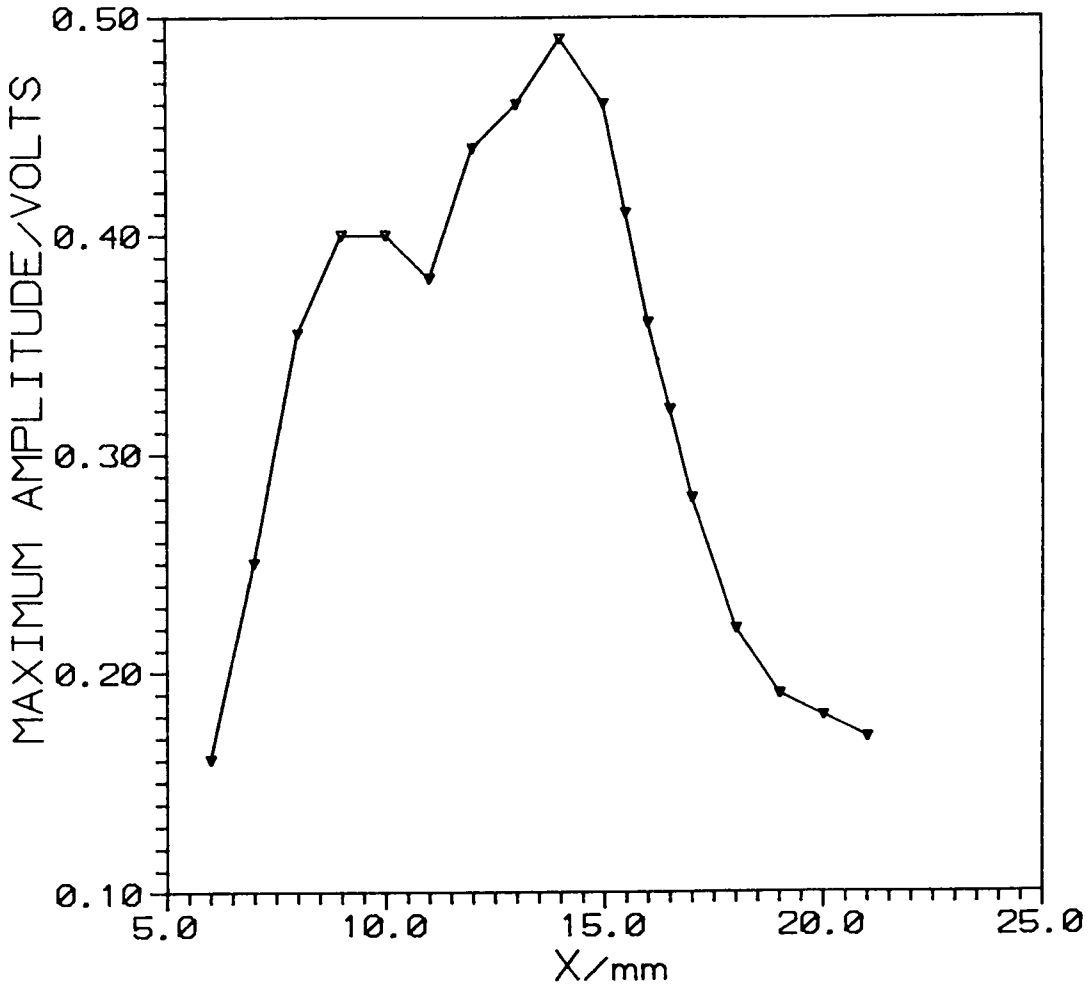


Figure 7.5. The variation of the peak signal amplitude along the length of the caustic.

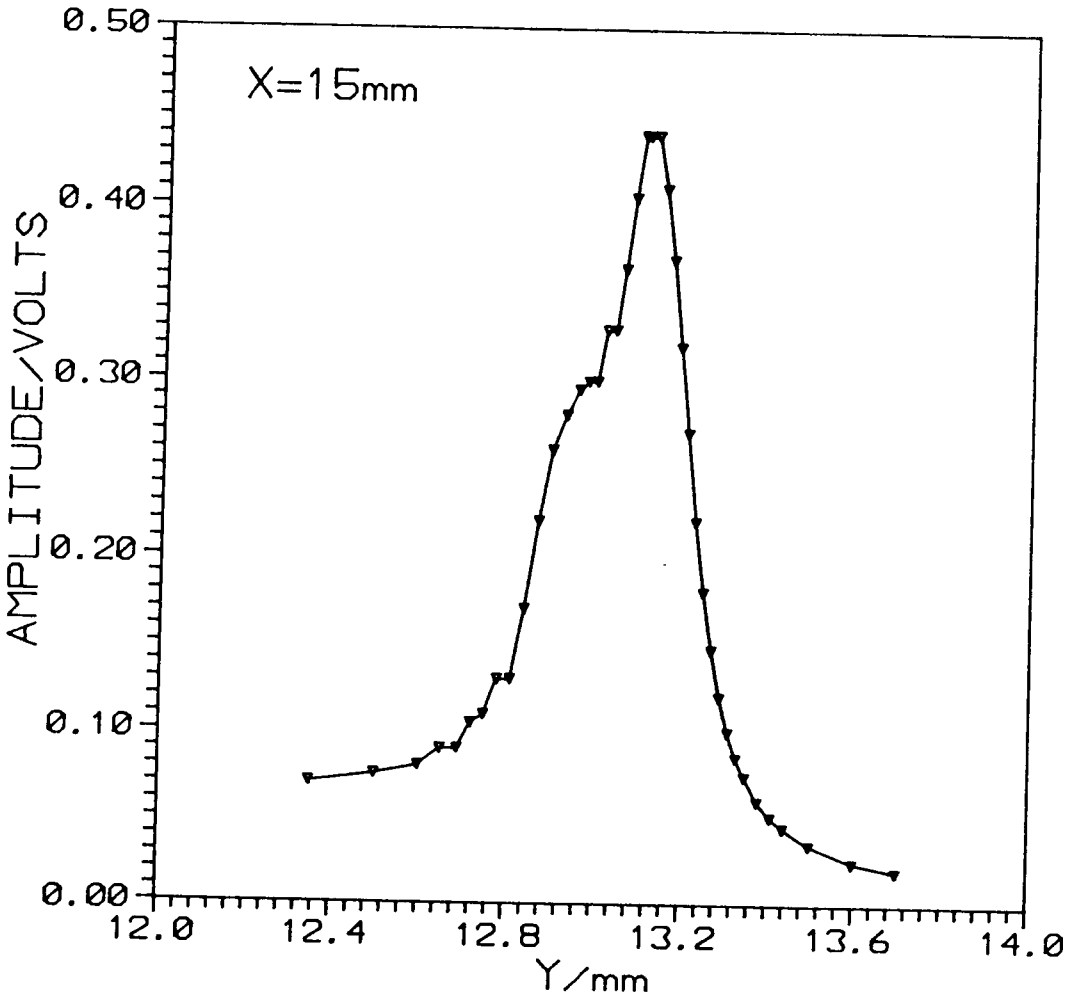


Figure 7.6. The amplitude profile across the caustic.

shadow side (higher Y) but shows more complicated behavior and decays more slowly on the illuminated side. For small Y the amplitude assumes a relatively constant value with an amplitude one sixth of that at the maximum. Note that only the first maximum of the Airy diffraction pattern shown in figure 3.3 appears. This is most probably due to the fact that here we have pulsed radiation rather than the continuous wave that Airy derived his formula for. It is this fact more than any other that makes this imaging system possible.

A final calibration of the imaging system is achieved by measuring the time of flight of the signal at its maximum as function of X. the time of flight is taken at the largest peak of the signal. As can be seen in figure 7.7 the two quantities are linearly related. The slope of the dependence is 0.75 mm/μs which, as would be expected, is one half of the speed of sound in water.

The inversion of the echo data to form an image is greatly simplified by the assumptions, justified above, that the caustic is a straight line and that the time of flight is proportional to the depth of the object point. The image, therefore, was constructed by dividing the time of flight of each signal by twice the speed of sound and plotting the amplitude of the signal against this coordinate and the Y-position of the object.

Ultrasonic images of the three test objects are now presented along side photographs of them. The amplitude contours were drawn from the data after it was processed in the manner

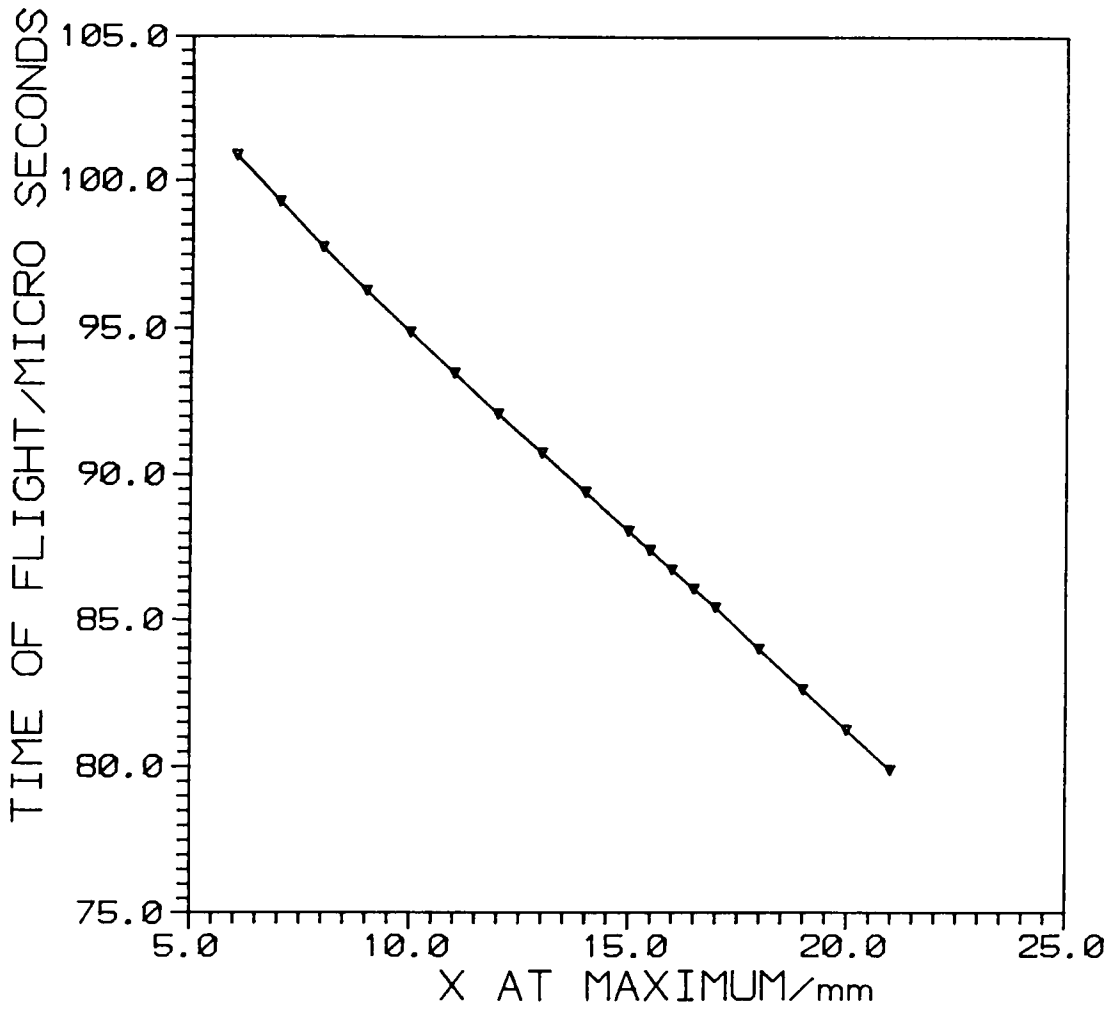


Figure 7.7. The time of flight as a function of x.

described above. The actual height of the contour lines is not as important as their relative number and density. The relative height of each peak can, unambiguously, be determined from the number of contour lines encircling it. In all diagrams there is an arbitrary cut-off voltage that removes the tops of the largest peaks. The axes of all the graphs are labeled in mm.

Figures 7.8 and 7.9, and the corresponding photographs, figures 7.10 and 7.11 show object A viewed from two directions perpendicular to each other. Figure 7.12 is a plan view of object A; photograph 7.10 is taken looking from right to left and photograph 7.11 is taken looking from top to bottom on that view. Localized peaks corresponding to reflections from the ends of the wires can be seen to the left of the large and complicated signal from the face of the epoxy. Four distinct and correctly placed peaks, corresponding to each of the wires can clearly seen in figure 7.8. The image in figure 7.9 is confused by presence of false peaks in addition to the, correctly placed, signals from the wires. These were most probably caused by sound, scattered from one of the wire, reaching the receiver via a reflection from one of the other wires rather than a direct route. Such signals could be identified in a real time imaging system by rotating the specimen. The movement of these false image spots would not be tied to the motion of the object. Note that in both cases, as might be expected, the broader wire generated a signal of higher amplitude that did the others.

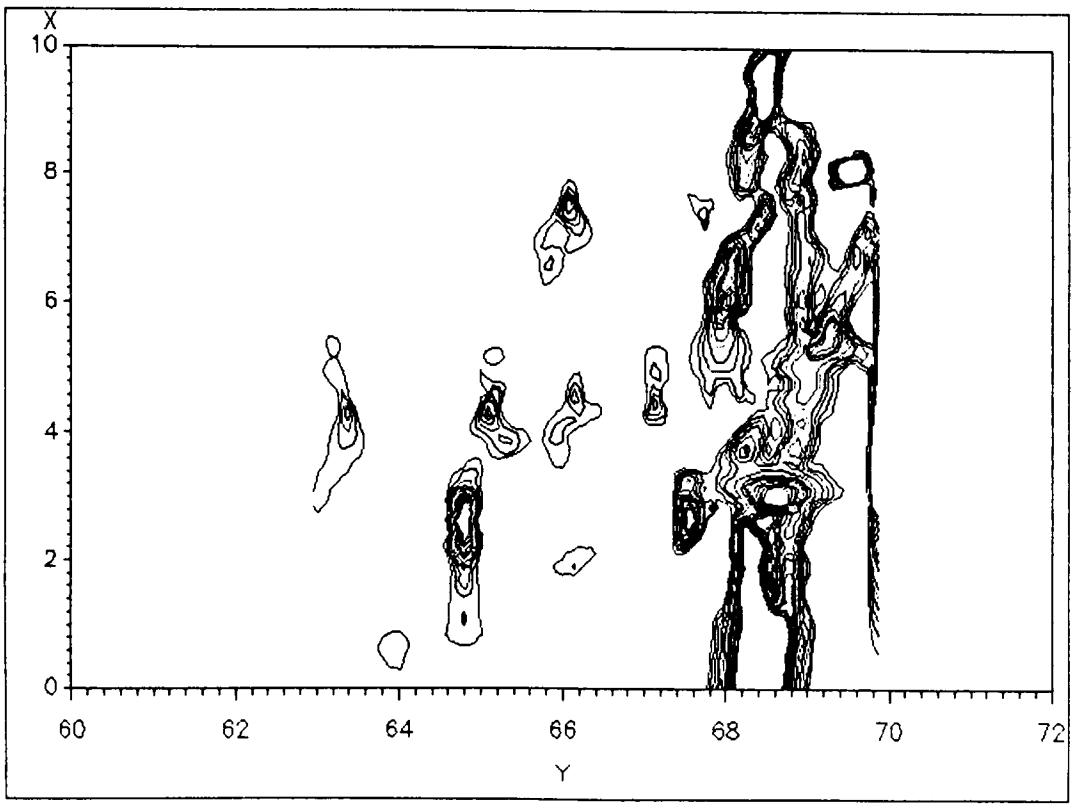


Figure 7.8. Ultrasonic image of object A.

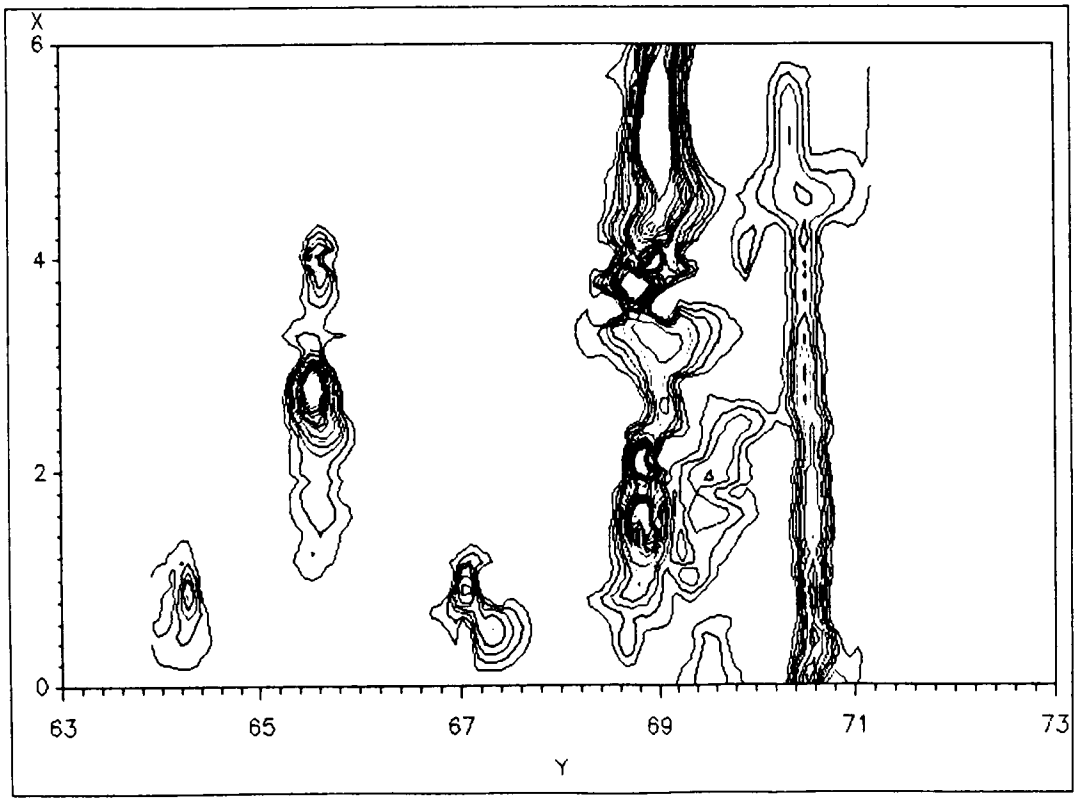


Figure 7.9. Ultrasonic image of object A from a perpendicular elevation

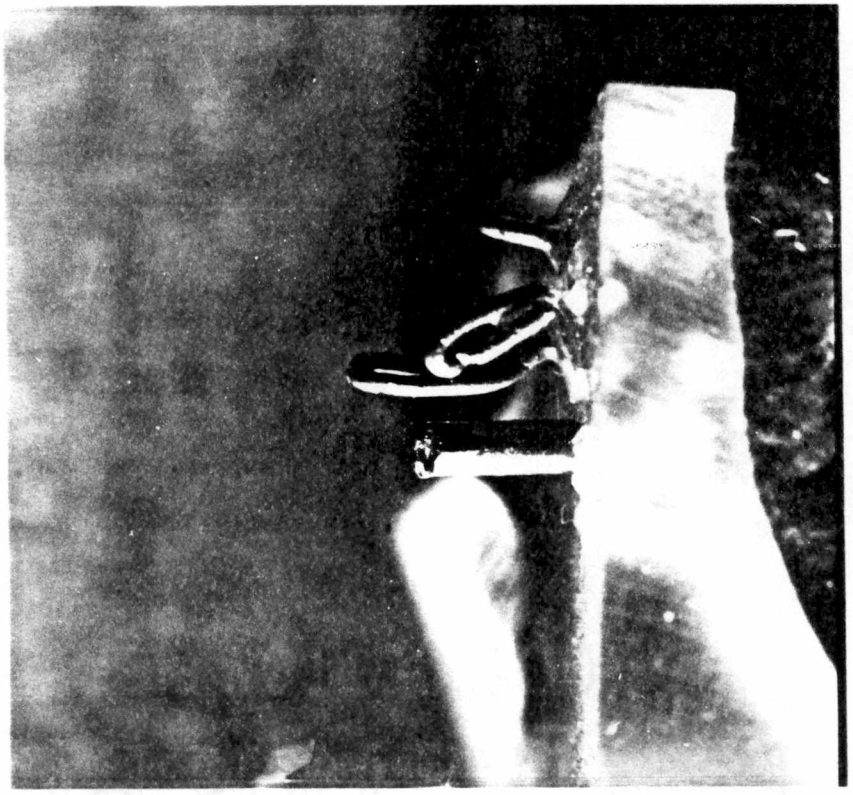


Figure 7.10. Object A.

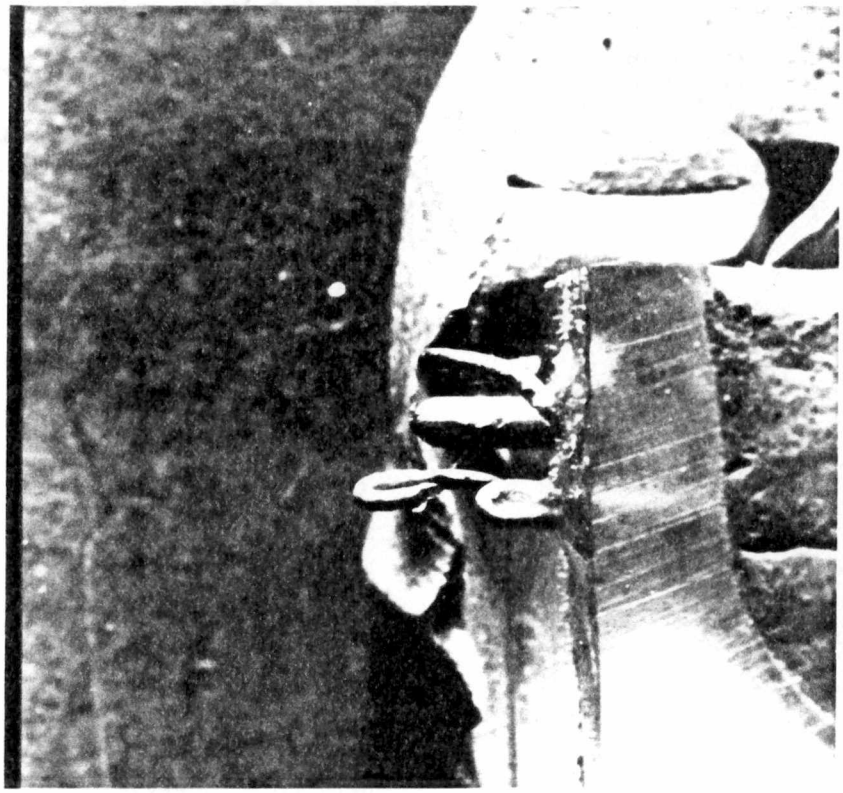


Figure 7.11. Object A viewed from a perpendicular elevation.

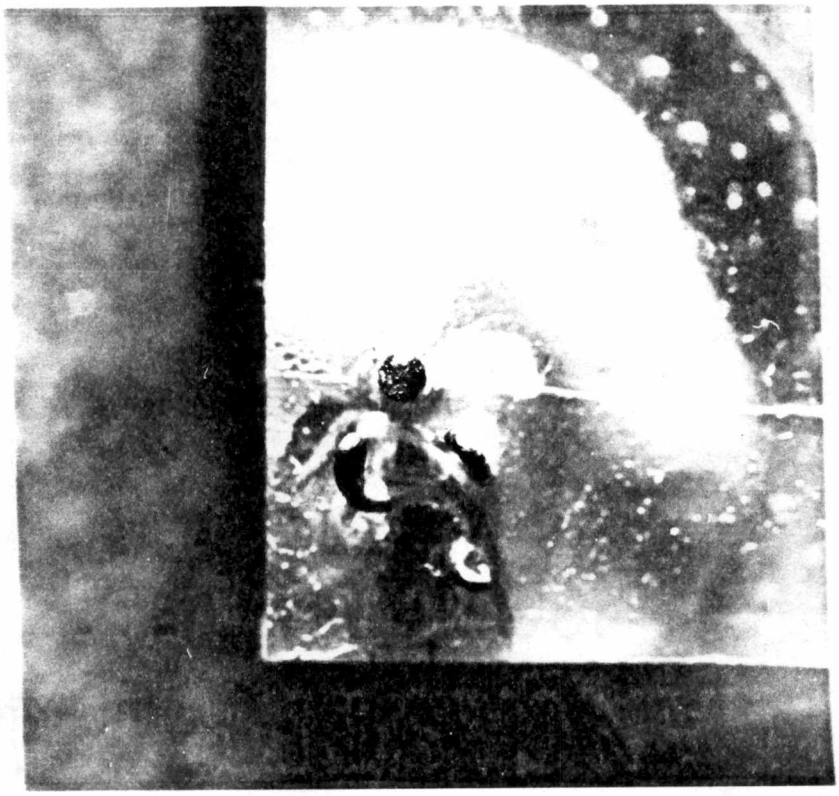


Figure 7.12. Plan view of object A.

Each signal is steeper on its high X side than on its low X side and, most of the peaks extend quite far in the direction of decreasing X. This is because, as X is decreased, the object point passes from the shadow side to the illuminated side of the caustic. On the illuminated side of the caustic, for a point object, the echo intensity is determined by the Airy diffraction profile. But, if an extended object is inside the illuminated zone, a signal of higher magnitude that that predicted by the diffraction theory will be received if the orientation on the object favours sending back one of the sound rays incident upon it. This has the effect of "smearing out" the object points into the negative X-direction. Towards the shadow side the width of the image points is close to the 0.2 mm predicted by the preliminary measurements.

An ultrasonic image of object B and its photographic counter part are given in figures 7.13 and 7.14 respectively. The Y-coordinate has been calculated on the assumption that all sound traveled in free water. As sound travels faster in epoxy than in water, the scale has been compressed. Four regions of high intensity can be seen behind the large signal from the from face. Only three of the wire tips can be seen on the photograph, the fourth, corresponding to the peak at coordinates (67.3, 2.5), was too deeply buried to be seen. Although it is difficult to resolve two of the points, both on the contour diagram and the photograph, the three signals appear in the correct relative locations. The smearing into the illuminated zone explained above can be plainly seen.

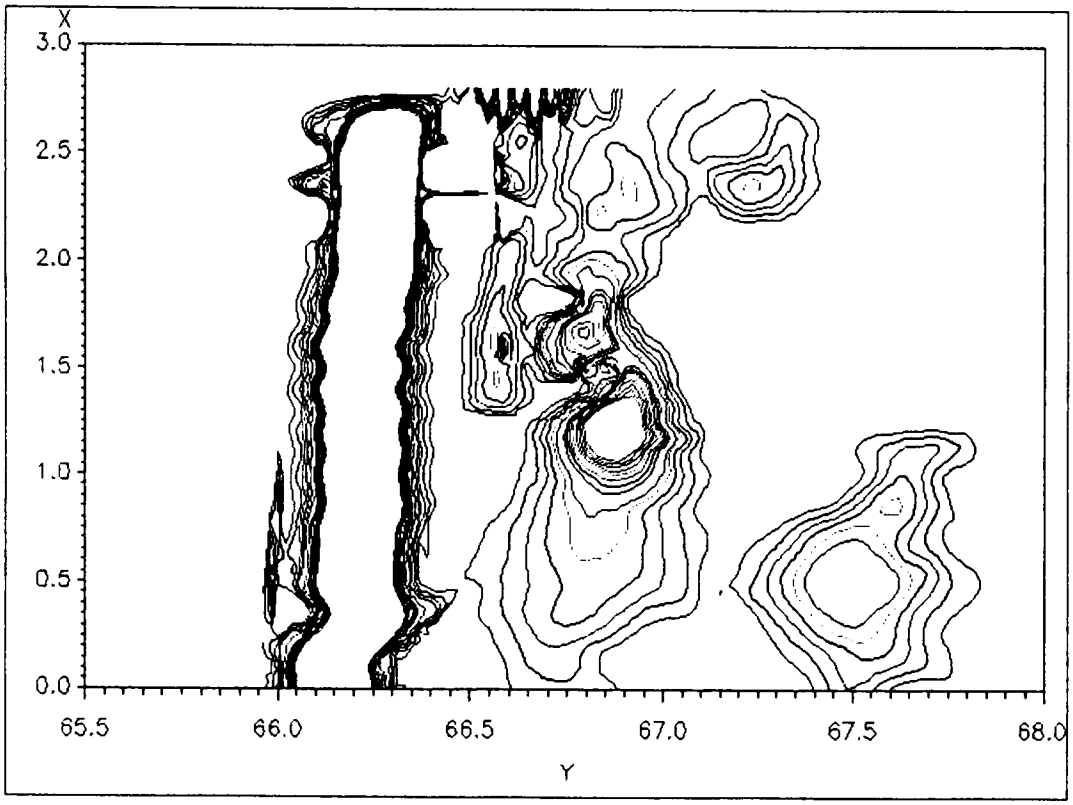


Figure 7.13. Ultrasonic image of object B.

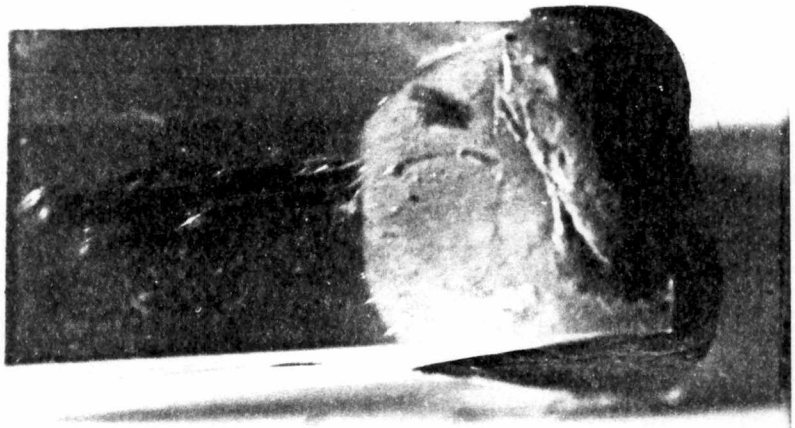


Figure 7.14. Object B.

A similar comparison is presented for object C in figures 7.15 and 7.16. Four of the planes could be detected within the epoxy and their relative position and orientation reproduced. The beaded appearance of ridges is merely an artifact of the the signal processing procedure, the manual data gathering and the contour level calculation technique employed by "SAS/GRAPH"..

Discussion

The principle advantage presented by the above imaging system is its high depth of field. For a conventional lens (or ultrasonic transducer), that forms an image via a point focus, the depth of field can be increased by stopping down its aperture. This is accompanied by a reduction in resolution, an effect quantified [BORN and WOLF 1964] by:

$$\Delta = \frac{r^2}{0.6 \cdot \lambda} \qquad 7.1$$

where, Δ, is the depth of field, r, is the resolution and λ is the wavelength. Substituting into equation 7.1 the wavelength of 20 MHz sound in water and the 0.2 mm resolution measured above yield a theoretical value of Δ of 0.9 mm. Here, the depth of field, which can be taken to be the length of the caustic before it broadens, was found to be 10.5 mm. The field of view is deeper by a factor of 11.7 than it would be for a conventional lens set up to have the same resolution. In the above experiment the length of

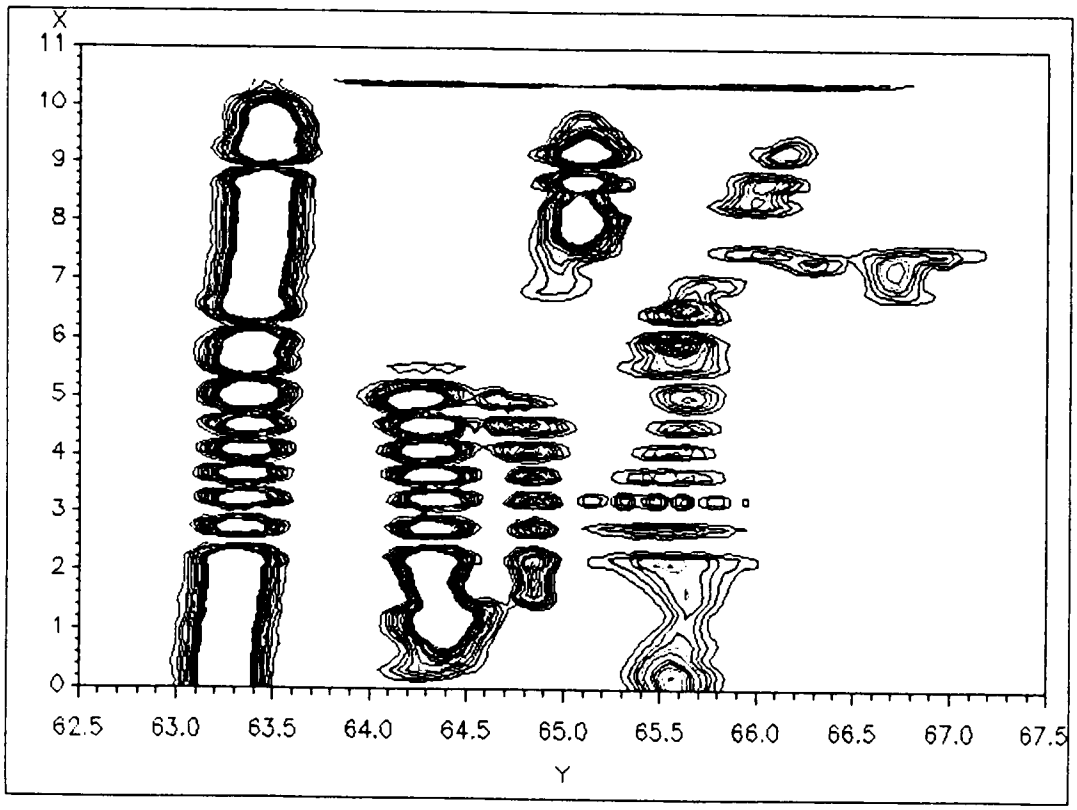


Figure 7.15. Ultrasonic image of object C.

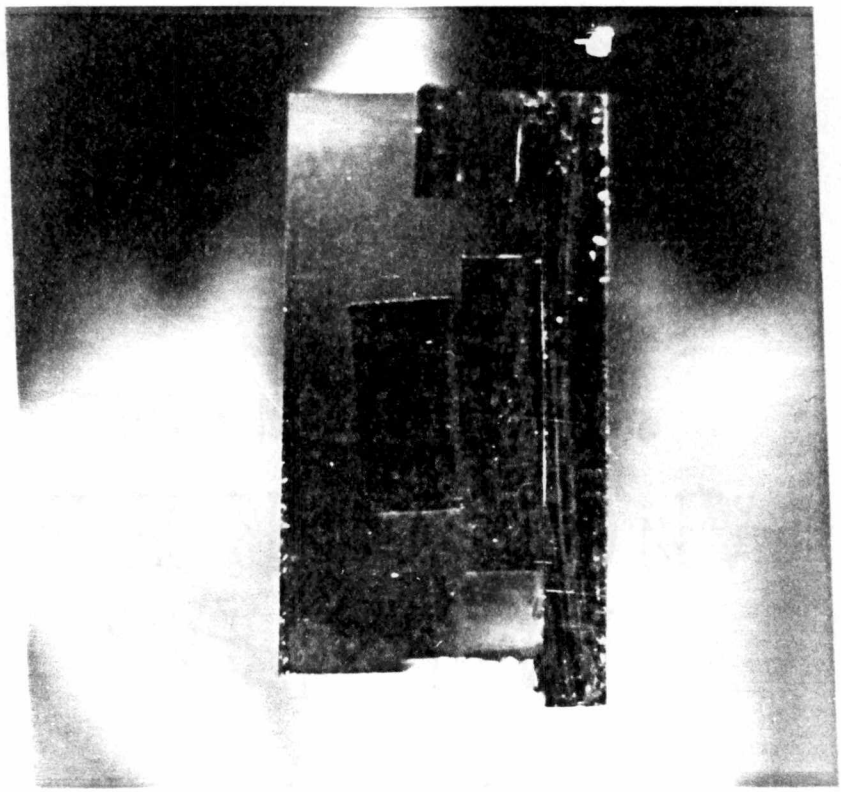


Figure 7.16. Object C.

the caustic was governed only by the geometry of the reflecting dish and the beam angle of the transducer. The fundamental limit of the ratio between depth of field and resolution is determined by relationship between the curvature of a caustic and its width (see equation 3.1). The length of caustic utilized in the imaging system is limited only by the amount of curvature one wishes to take into account and the design of the apparatus generating it.

The practical consequence of this depth of field is that the entire specimen can be inspected during one scan through the caustic. This could greatly increase the speed of operation and would be of value in non-destructive testing applications where the depth of the defects is not known prior to the test.

CHAPTER 8

THE APPLICATION OF CAUSTICS TO MICROSCOPY

Introduction

Well defined caustics are formed by ultrasound, with a wavelength on the order of millimeters, whose radii of curvature are on the order of several centimeters [BREWSTER 1989]. Given this, it can be concluded that if the wavelength is scaled down to that of light, caustics will be observable with structures on the scale on the order of hundreds of microns. These caustics have the potential to be used to obtain topological information on a microscopic scale. Before this can be done a procedure must be developed to invert the information contained within the caustics to yield the surface that caused them.

Consider a specimen prepared such that it is smooth enough to reflect light in a specular manner yet contains enough undulations to be of interest. If this is made to reflect a parallel beam of light then the reflected ray field will contain these microscopic caustics. This is illustrated by figure 8.1 which shows caustics formed by the transmission of light through a cellulose replica of an iron fracture surface. As will be discussed below, a microscope views a slice through the caustic surface which can be in front of or behind the specimen.

Each reflected ray can be shown to be tangential to two caustics. Consider a vertical ray incident upon a general surface,

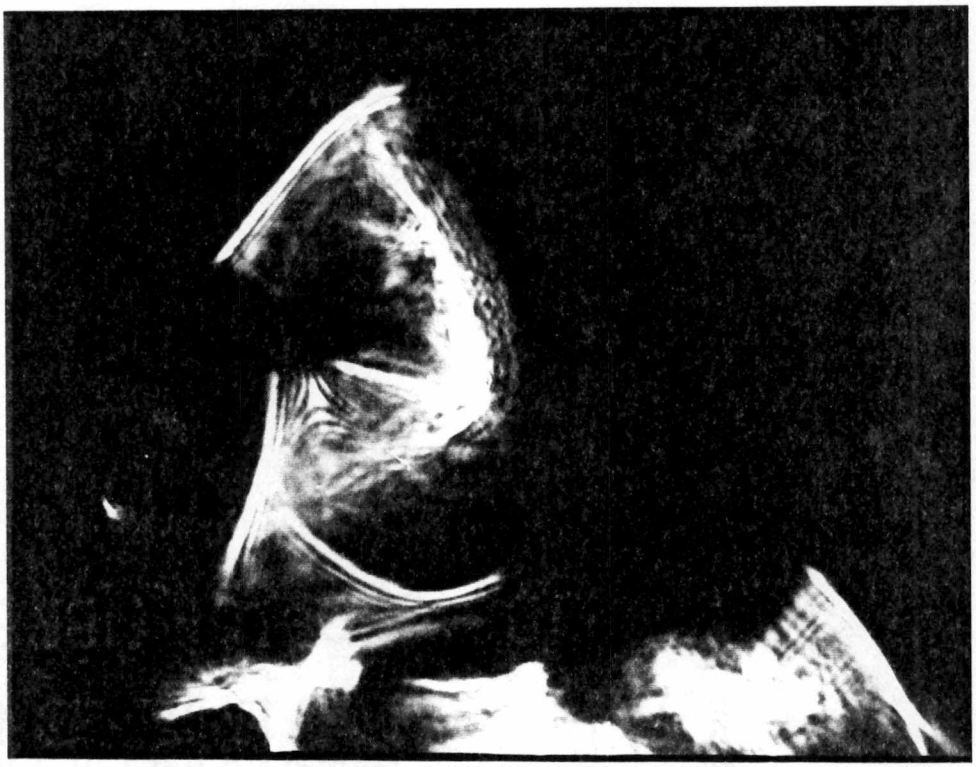


Figure 8.1. Caustics formed by the transmission of light through a replica of a fracture surface.

S(x,y), at a point (X,Y) (figure 8.2). After reflection from (or refraction by) the surface the light ray follows an oblique path meeting the plane of observation, z=Z, at point (U,V). Mathematically, the interaction between the rays and the surface is described by a map from variables (X,Y) to variables (U,V). The Jacobian of this transfer is defined by:

$$J(X,Y) = \frac{\partial U}{\partial X}\cdot\frac{\partial V}{\partial Y} - \frac{\partial U}{\partial Y}\cdot\frac{\partial V}{\partial X} \qquad 8.1$$

One property of this function is that a small area in X-Y space

$$dA = dX \cdot dY \qquad 8.2$$

maps into an area in U-V space, dA′, given by

$$dA' = J \cdot dA \qquad 8.3$$

The consequence of this is that, if the Jacobian is zero a finite area on the surface maps the rays onto zero area at the image plane resulting in an infinite wave intensity in the ray approximation. This is the caustic. The set of points on the surface which give rise to a reflected ray that is tangential to the caustic at height, Z, is given by:

$$J(X,Y) = 0 \qquad 8.4$$

The dependence of the functions U(X,Y) and V(X,Y) on Z can be expressed by writing them as:

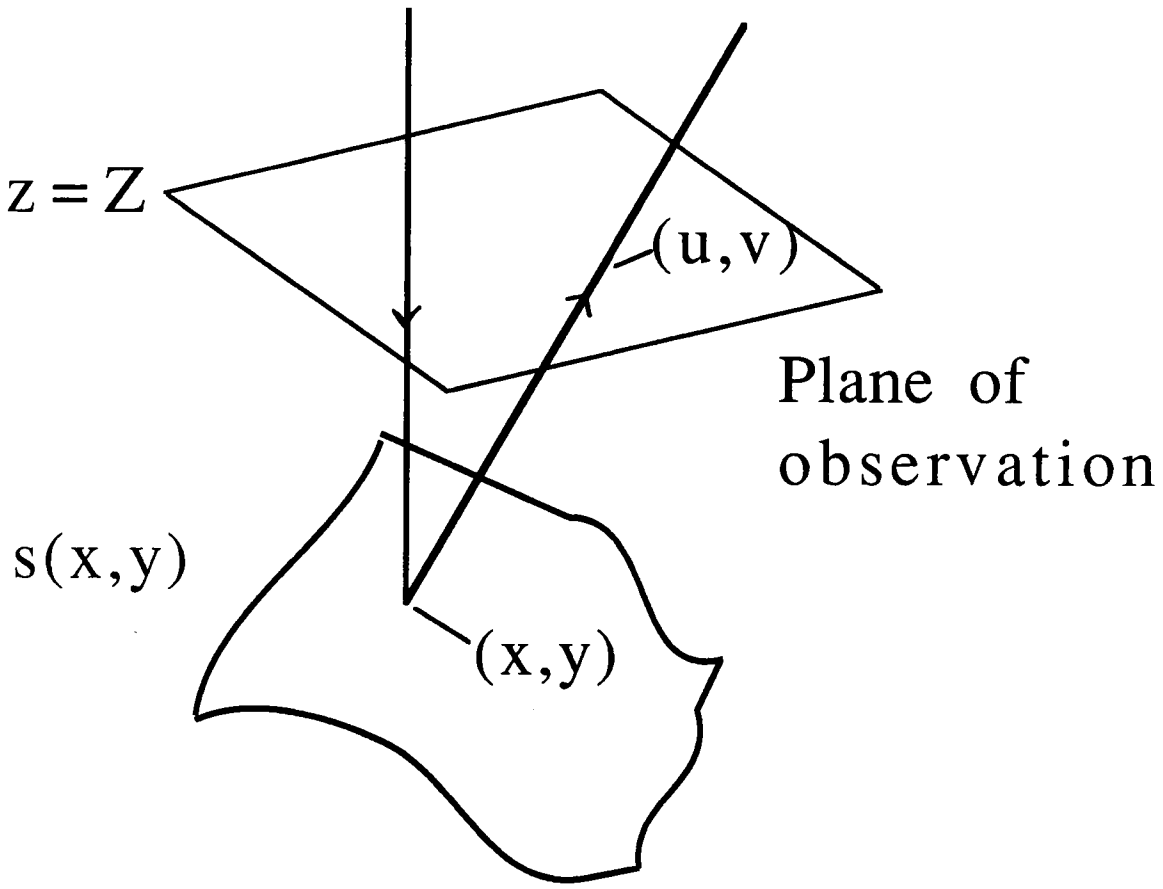


Figure 8.2. A vertical ray being reflected by a general surface.

$$U(X,Y) = X + Z \cdot a(X,Y) \qquad 8.5$$

$$V(X,Y) = Y + Z \cdot b(X,Y) \qquad 8.6$$

where a(x,y) and b(x,y) are the direction cosines between the reflected rays and the X and Y-axes respectively. Differentiating these expressions, the Jacobian can be written:

$$J = (1 + Z\frac{\partial a}{\partial X}) \cdot (1 + Z \cdot \frac{\partial b}{\partial Y}) - Z \cdot \frac{\partial a}{\partial Y} Z \cdot \frac{\partial b}{\partial X} \qquad 8.7$$

$$J = Z^2 \cdot \left(\frac{\partial a}{\partial X} \frac{\partial b}{\partial Y} - \frac{\partial a}{\partial Y} \frac{\partial b}{\partial X} \right) + Z \cdot \left(\frac{\partial a}{\partial X} + \frac{\partial b}{\partial Y} \right) + 1$$

$$= 0 \qquad 8.8$$

This a quadratic in Z therefore, there are either zero or two values of Z for which J=0 for any point on the surface. It can be shown [STAVROUDIS 1972] that for any set of rays operated on by the laws of reflection and reflection alone, equation 8.8 must have real roots. This implies that each reflected ray is tangent to the caustic surface twice, at values of Z given by the roots of equation 8.8.

The direction cosines of the reflected rays can be written as functions of the two first derivatives of the surface, S(x,y). Therefore, each first derivative a(x,y) and b(x,y) must depend, in general, on the three second derivatives of the surface in addition to its slope. If the values of Z were found experimentally, equation 8.8 could be rearranged to yield two simultaneous equations

(representing the sum and product of its roots). Thus, we have only two equations with which to deduce the values of five unknown quantities implying that one needs more information than the height at which the caustic is crossed to deduce the surface.

Based on the theorem that each ray touches the caustic surface twice, the inversion procedure for the information contained within the caustics is to search for straight lines which are simultaneously tangential to two caustic surfaces. This set of lines can then be assumed to be the loci of real reflected rays. Thus, the normal direction to each point on the specimen surface can be calculated and its shape constructed.

A well configured microscope performs the task of taking the rays emanating from a point in the object plane and mapping them onto a single point in the image plane with the desired magnification (probably at infinity, depending on the eyesight of the observer). This implies that rays meeting as they cross the object plane will also meet as they cross the image plane. A caustic observed in the image plane is, therefore, an image of the line of intersection between the caustic surface and the object plane (figure 8.3). The loci of these focal surfaces can be thus be determined by using the focus adjustment on the instrument to scan the object plane though the caustics, above and below the surface of the sample. With the object plane below the specimen surface the caustics observed will be virtual caustics representing the surface on which rays would meet their neighbors if traced

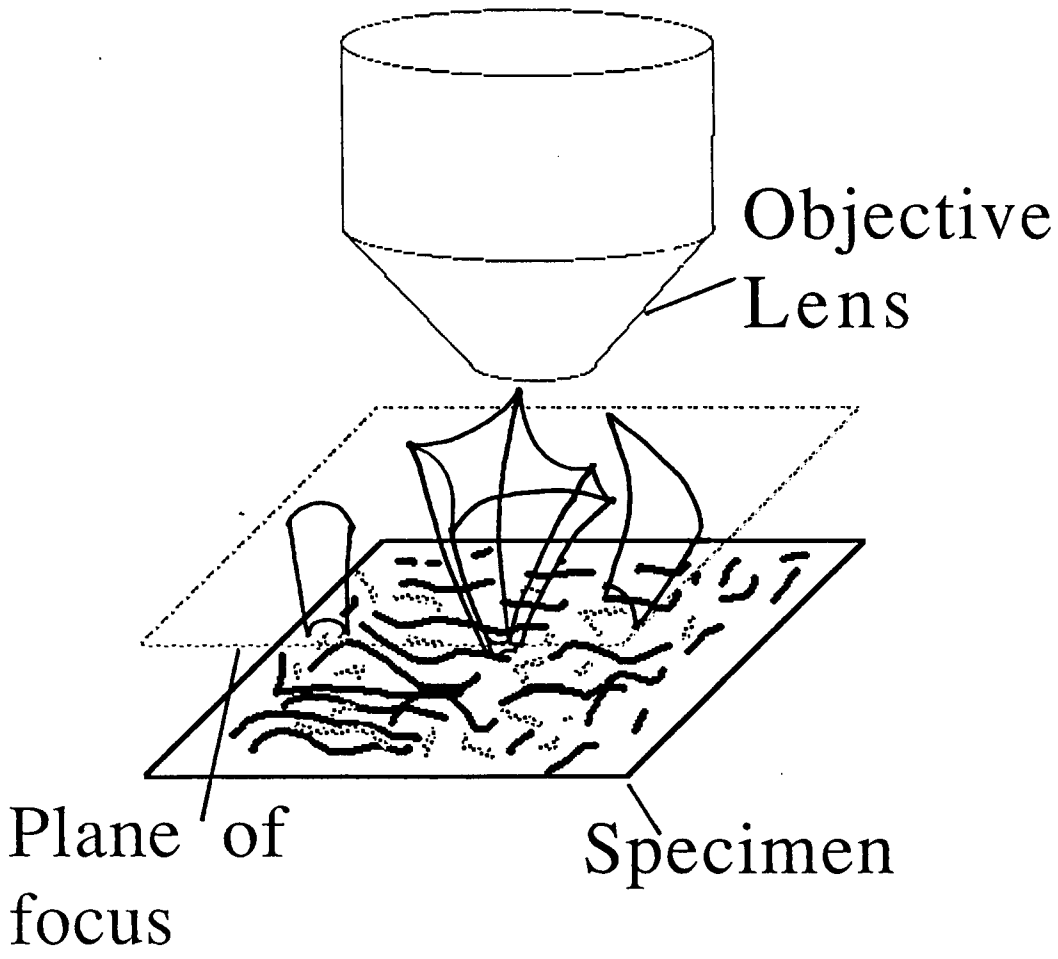


Figure 8.3. A caustic surface being sectioned by the image plane of a microscope.

back behind the sample. For the purpose of solving the inversion problem real and virtual caustics are equally valid.

The algorithm necessary to invert the information contained within these foci was developed using a computer model. A computer program will calculate the loci of the caustics formed by parallel rays reflected from an arbitrary surface. This data will be stored in the form of sets of coordinates representing the section of this system of foci at various heights. A second program will then take this data, search for common tangent lines between the caustics and attempt to reconstruct the original surface without any *a priori* knowledge of its topology.

The aim of these studies is to lay the foundation for the development of automated, 3-dimensional imaging systems utilizing these caustics.

All the calculations described below were executed by the computer programs listed in appendix C.

The Inversion Algorithm

The fact, proved above, that each ray is twice tangential to the caustic surface also implies that two sections through the caustic, taken at different heights, will have an even number of rays linking them. To prove this, consider a section through the caustic taken at height, $z=Z_1$. Let σ be the set of points on the surface that are the points of reflection of the rays which go on to touch the caustic at Z_1. As the section through the caustic observed

in the plane takes the form of a finite number of closed loops, σ, consists of a finite number of closed loops. We wish to find rays, which, in addition to touching the caustic at Z_1, are also tangential to it at a second height, Z_2. Let, ζ, be the value of the other root of equation 8.4 for a particular point in σ. As each loop in σ is rounded, ζ will vary and, as a consequence of periodicity, will be equal to Z_2 an even number of times (including the possibility of zero roots).

Therefore, the inversion procedure is to take sections through the caustic at two different heights and search for lines that are tangential to it at both. These common tangents will assumed to be the paths of rays. The two fundamental limitations to this method are that there may be common tangents which do not represent rays and the finite precision of any practical method makes the exact definition of tangentcy impossible.

A closely analogous mathematical situation occurs in thermodynamics. At a fixed temperature, one can derive an isothermal phase diagram for a three component system by considering the Gibbs free energy as a function of composition [LUPIS 1983]. As two parameters are required to specify the Gibbs free energy, it is represented by surfaces in a three dimensional space. In order to find the boundaries to the various two phase regions, one must search for common tangents between the various branches of the Gibbs free energy surface. The projections of these lines onto the phase diagram are called "tie lines" and inform its user of the composition of the two phases present.

Given an arbitrary reflecting surface, the caustic surface was calculated by numerical solution of equation 8.4. The program that did this stored sets of points representing the surface in data files, each corresponding to a different value of z. So that the tangent planes could be calculated the values of z were chosen in closely spaced pairs.

The inversion procedure is initiated by opening four data files corresponding to sections through the caustic at two pairs of values of z, Z_1 and Z_2. The tangent at one point, P_0, on one of the lines at level Z_1, was found by finding the straight line that passes through that point and one of its neighbors. The other member of this pair of sections through the caustic was then searched for places that have a tangent parallel to that particular line. The closest of these parallel tangents and the original tangent line are assumed to both lye in the tangent plane to the caustic at P_0. The tangent plane was therefore known and the line of its intersection with the plane, $z=Z_2$, calculated.

One of the data sets, corresponding to the section through the caustic at height Z_2, was then searched for minima in its distance from this line of intersection with the tangent plane. Let this minimum distance be D_1. When a minimum was found, the tangent plane to the caustic at this point was calculated by the same method as above. The line of intersection of this plane with the original plane, $z=Z_1$, was calculated and its perpendicular distance from P_0, D_2, found. In order to evaluate how close the to line

calculated was to being a common tangent, the arithmetic mean of D_1 and D_2, D, was recorded. D was converted into an angle by dividing by, Z_1-Z_2.

The above procedure was repeated for every data point in the initial section through the caustic. The four lowest values of D that could be found were assumed to be genuine common tangents and therefore, represent rays.

The above algorithm was repeated for every pair of Z-values.

The surface used to test this theory was:

$$s(x,y) = \alpha \cdot x^3 + \beta \cdot x^2 y + \chi \cdot x y^2 + \delta \cdot y^3 + \varepsilon \cdot x^2 + \phi \cdot xy + \gamma \cdot y^2 \qquad 8.9$$

with the parameters set at;

$$\alpha = \beta = \delta = \varepsilon = \phi = \gamma = 2/3$$

and $\chi = 200/3$

The surface was confined to the area:

$$-0.1 < x < 0.1$$

and $$-0.1 < y < 0.1$$

and is plotted in figure 8.4, in which the spacing of the contour lines is 0.005. The sections through the caustic were calculated at 20 different levels ranging from -10 to +10. Some of these are shown in figure 8.5 and at a higher magnification in figure 8.6.

The point of intersection with the plane, z=0, of each potential ray was found. The angle between this ray and the expected

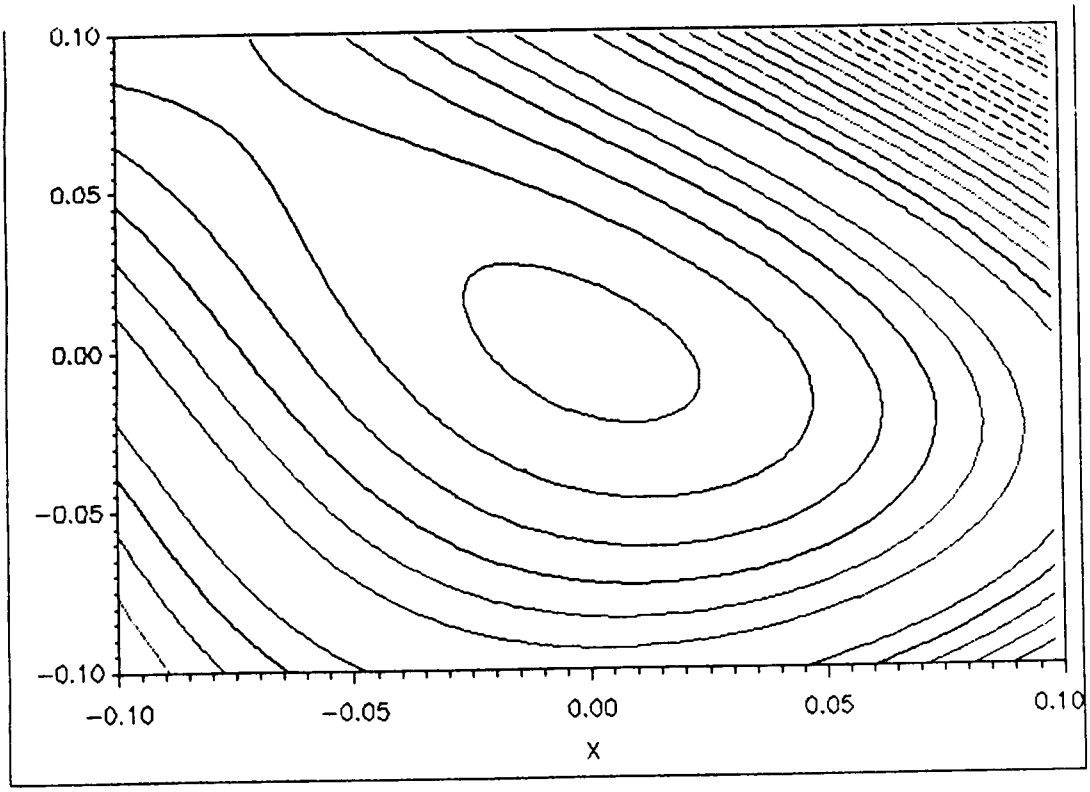


Figure 8.4. The surface used to test the inversion algorithm.

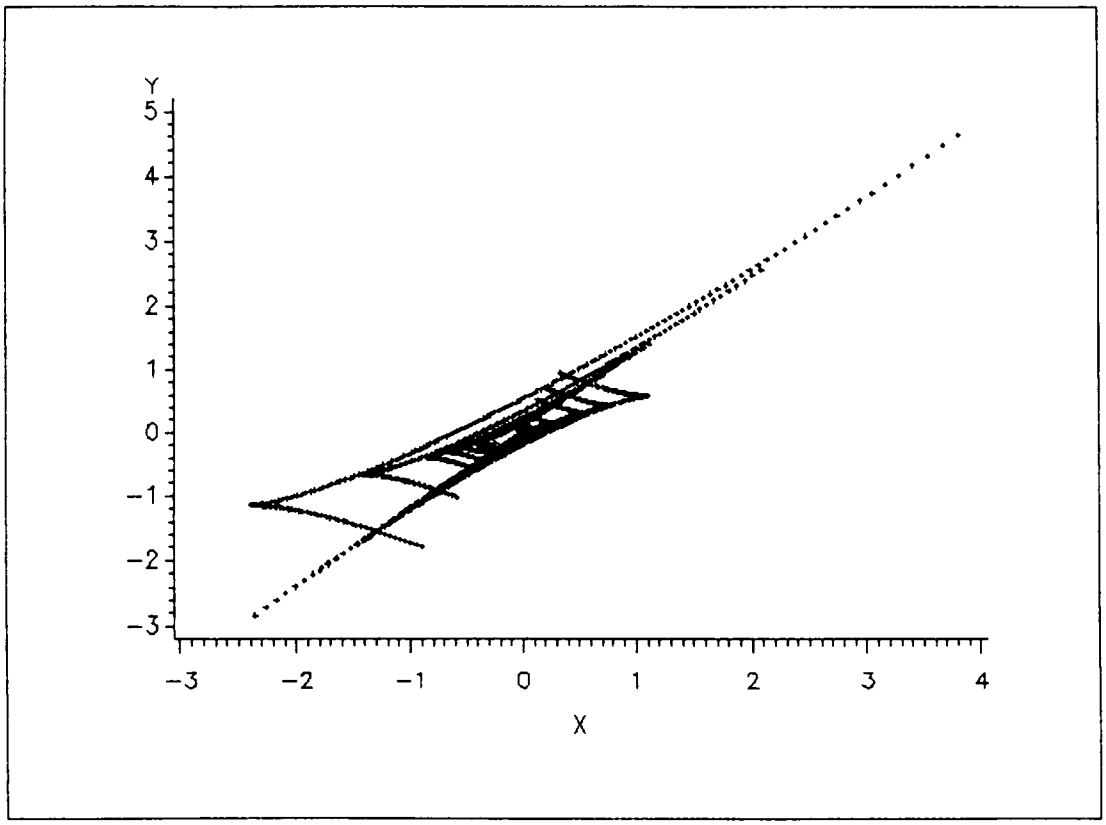


Figure 8.5. Sections through the caustic surface.

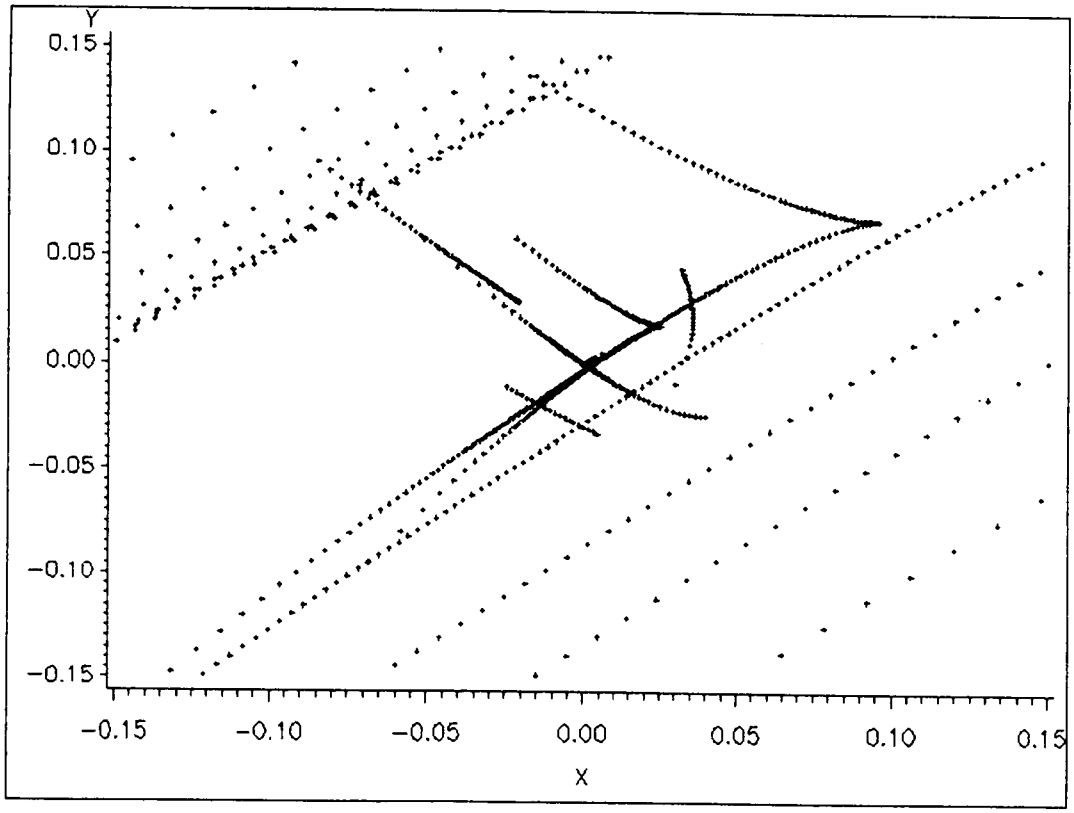


Figure 8.6. Sections through the caustic surface.

reflected ray at this point, Δ, was calculated. Figure 8.7 shows the relationship between D and Δ. It can be seen that there are some rays that deviate from that expected by as much as 30°. These could be removed by excluding all the rays with a value of D higher than a certain cut-off value, say, 0.5°. This would remove all the bad rays but would also remove many of the accurate rays as well.

Another way of checking the rays is to make use of the smoothness of the surface. The orientation of each ray is expressed by a unit vector parallel to it, $\mathbf{r}_i$. For each ray, the rays with the 50 nearest points of intersection with the surface to its own, $\mathbf{s}_i$, are found. Let the vector, $\mathbf{A}$, be defined by:

$$\mathbf{A} = \frac{1}{N}\sum_{i=1}^{N}(\mathbf{r}_i - \mathbf{s}_i) \qquad 8.11$$

Here N=50. The scalar, A, is given by:

$$A = |\mathbf{A}| \qquad 8.12$$

The dependance of Δ on A is plotted in figure 8.8. The more wayward rays stand out from their neighbors and so have a higher value of A. Rays having a value of, A, higher than 0.6 were excluded and their A-values were recalculated. This was repeated until no rays exceeded this condition. Figure 8.9 shows the distribution of the accuracy of the rays after this elimination process.

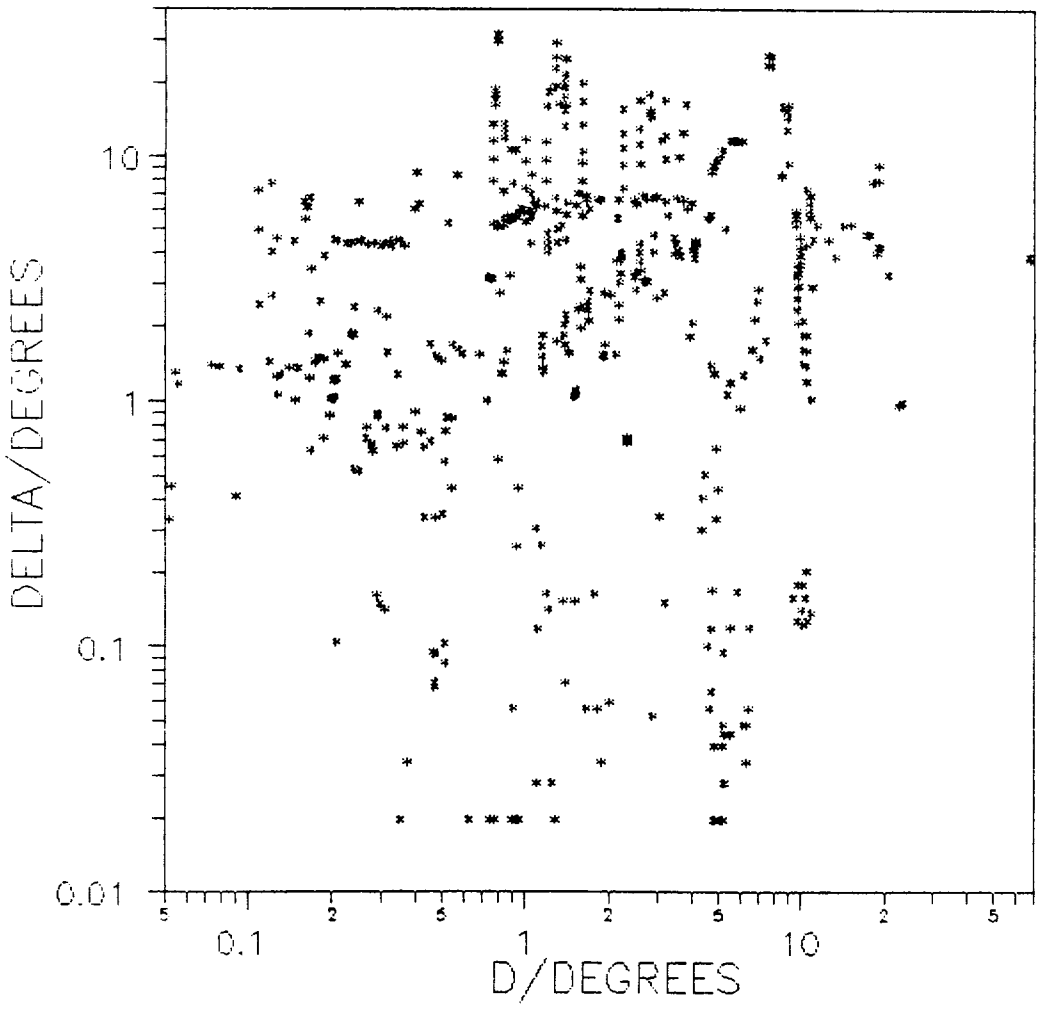


Figure 8.7. The accuracy of the rays as a function of the goodness of fit.

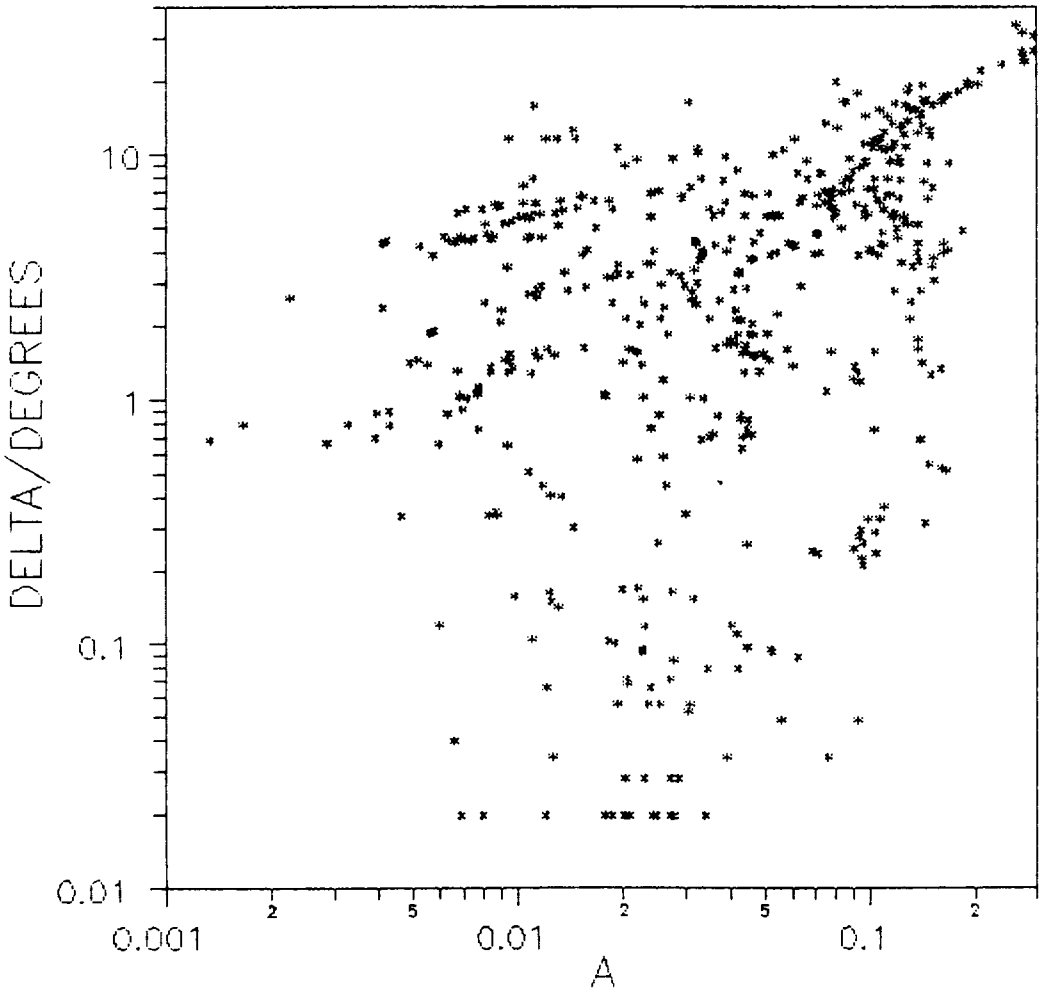


Figure 8.8. The accuracy of the rays as a function of A.

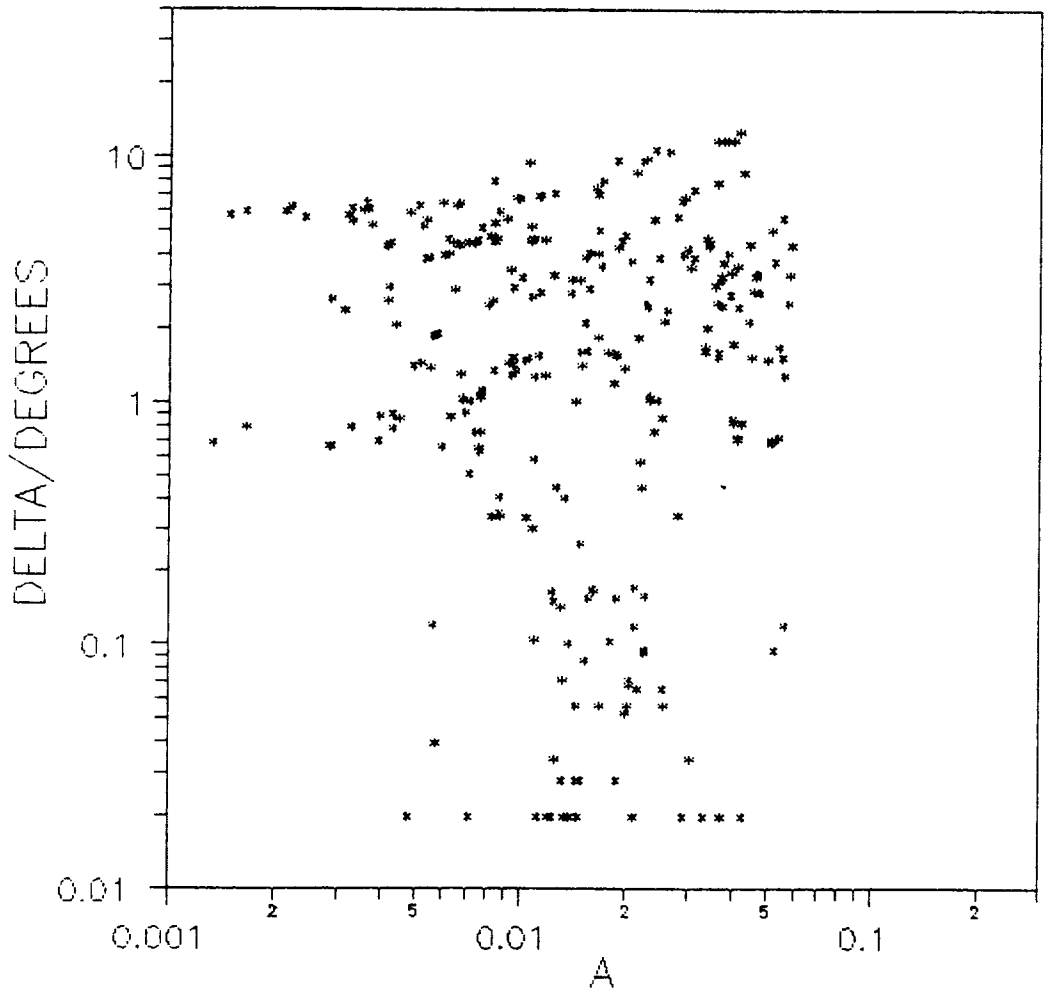


Figure 8.9. The accuracy of the rays as a function of A after the elimination process.

It can be shown that, for a reflection process, an error in the orientation of the ray of, Δ, results in an error in the calculation in the slope of the surface of $\Delta/2$. In figure 8.10 this error is plotted as a function of the angle between the surface normal and the vertical direction. The straight line represents the equality of these two quantities. It can be seen that some data points exhibit a very high degree of accuracy but, others reproduce the slope of the surface no better than would the assumption that it is horizontal.

Figure 8.11 shows the distribution of these data points on the specimen surface. The large circles represent locations where the accuracy was better than the slope of the surface and the smaller crosses represent locations where this was not true. Although there is some clustering, the data points are reasonably well spread out across the surface.

Discussion

The number of less accurate points seen in figure 8.10 is an indication that the algorithm has only had limited success in separating genuine common tangents between parts of the caustic surface from lines that appear to be. If the program is not able to

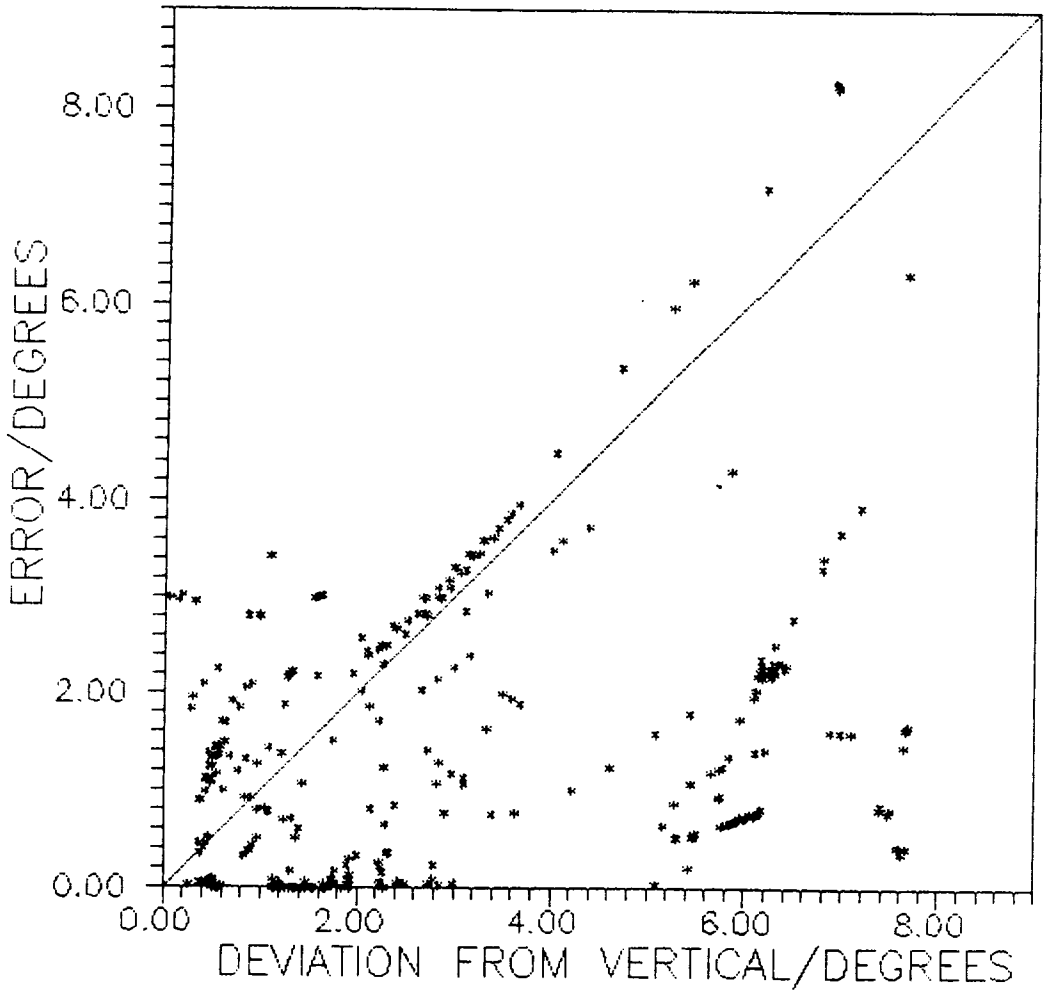


Figure 8.10. The error in the predicted slope as a function of the predicted gradient.

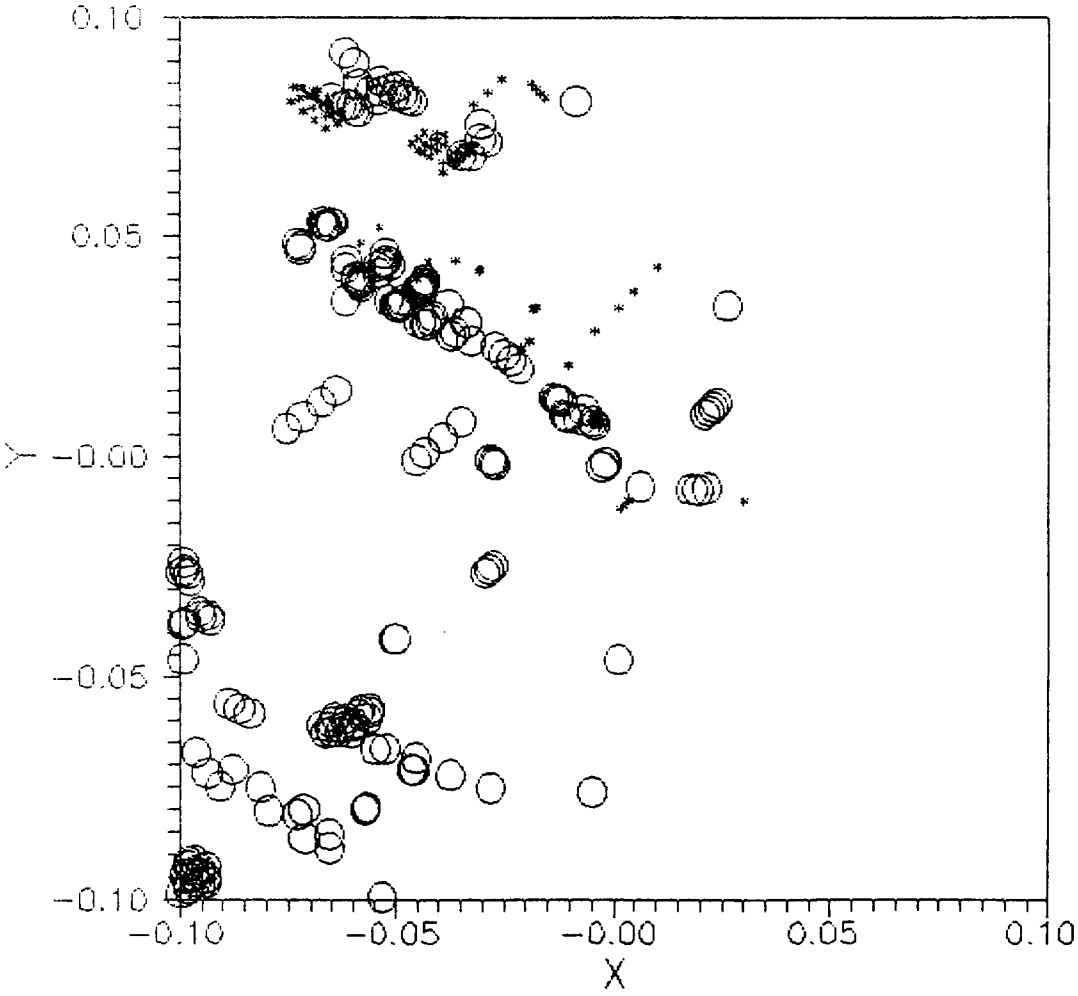


Figure 8.11. The distribution of the points at which the slope has been determined.

perform under these idealized conditions it will have no chance of inverting real experimental data.

Improvements need to be made to the inversion algorithm before caustics can be applied to three dimensional microscopy in the proposed manner.

CHAPTER 9

OPTICAL CAUSTICS AND THE MEASUREMENT OF SMALL DISPLACEMENTS

Introduction

In situations where the ray approximation applies, a caustic constitutes a very well defined boundary in a wave field. But, in addition to this, the diffraction pattern that decorates the singularity due to the wave character of light has the form calculated by Airy. This implies that even though the caustic determined by the ray geometry is not observable, its position can be calculated relative to the observed diffraction bands. This permits precise determination of the location of caustics and from this the measurement of small changes in the surfaces creating them.

The work presented in this chapter is an attempt to obtain precise, quantitative information about a deformed surface from caustics observed in light reflected from it. This is in contrast to the work of Theocaris which involves using the qualitative form of the caustics to confirm the theoretically expected surface deformation, albeit for far more complicated geometries.

Initially confining ourselves to two dimensions, consider a beam of rays, parallel to the z-axis, reflected from a smooth line described by S(x) (figure 9.1). The angle of incidence, θ, is given by:

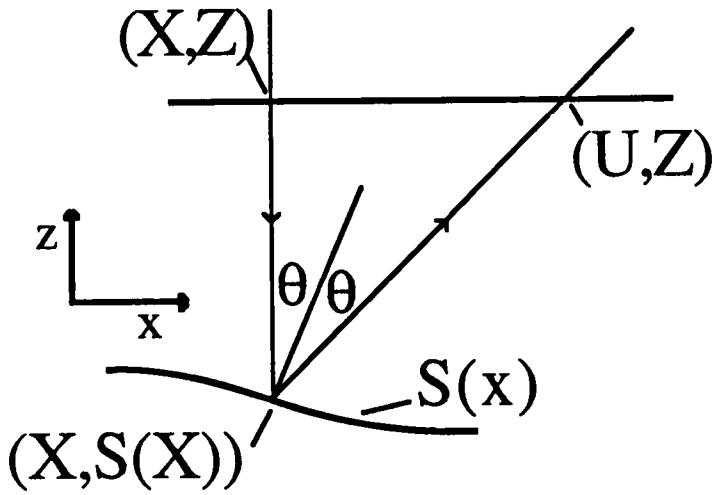


Figure 9.1. A ray being reflected from a surface, s(x).

$$\tan(\theta) = -\frac{dS(x)}{dx} \qquad 9.1$$

Where, X, is the original x-coordinate of the ray. If the reflected rays are observed by their intersection with a screen whose z-coordinate is Z, then the point, U, where a ray crosses the screen is given by:

$$U = X+(Z-S(X))\cdot\tan(2\theta) \qquad 9.2$$

As $\frac{dS(x)}{dx}$ and therefore, θ, are small, we can use the approximations:

$$\tan(2\theta) = 2\theta \qquad 9.3$$

and

$$\theta = -\frac{dS(x)}{dx} \qquad 9.4$$

Equation 9.2 now becomes:

$$U = X-(Z-S(X))\cdot 2\frac{dS(x)}{dx} \qquad 9.5$$

Differentiating with respect to X:

$$\frac{dU}{dX} = 1-2\cdot\left[(Z-S(x))\frac{d^2S(x)}{dx^2}-\left\{\frac{dS(x)}{dx}\right\}^2\right] \qquad 9.6$$

$$\left\{\frac{dS(x)}{dx}\right\}^2 \approx 0 \qquad 9.7$$

At a caustic U is stationary with respect to X. Therefore:

$$\frac{dU}{dX} = 0 \qquad 9.8$$

and

$$1 = 2\cdot(Z-S(x))\cdot\frac{d^2S(x)}{dx^2} \qquad 9.9$$

thus:

$$Z-S(x) = \frac{1}{2\cdot\frac{d^2S(x)}{dx^2}} \qquad 9.10$$

It can be seen that the distance between the screen and the reflector leads to a direct measurement of the second differential of the surface at the point of reflection of the critical ray that touches the caustic and the screen simultaneously. The above derivation will hold if the surface is 3-dimensional yet possesses complete rotational
symmetry the derivatives being taken along the radial direction. In this case the caustics will have the same rotational symmetry.

Consider the apparatus shown in figure 9.2. The "telescope" refers to a combination of lenses and a camera such that their object plane is at infinity. The specimen is a glass microscope cover slip pressed against a circular aperture by a sharp point with a force measured by a load cell. If care is taken that the point load is

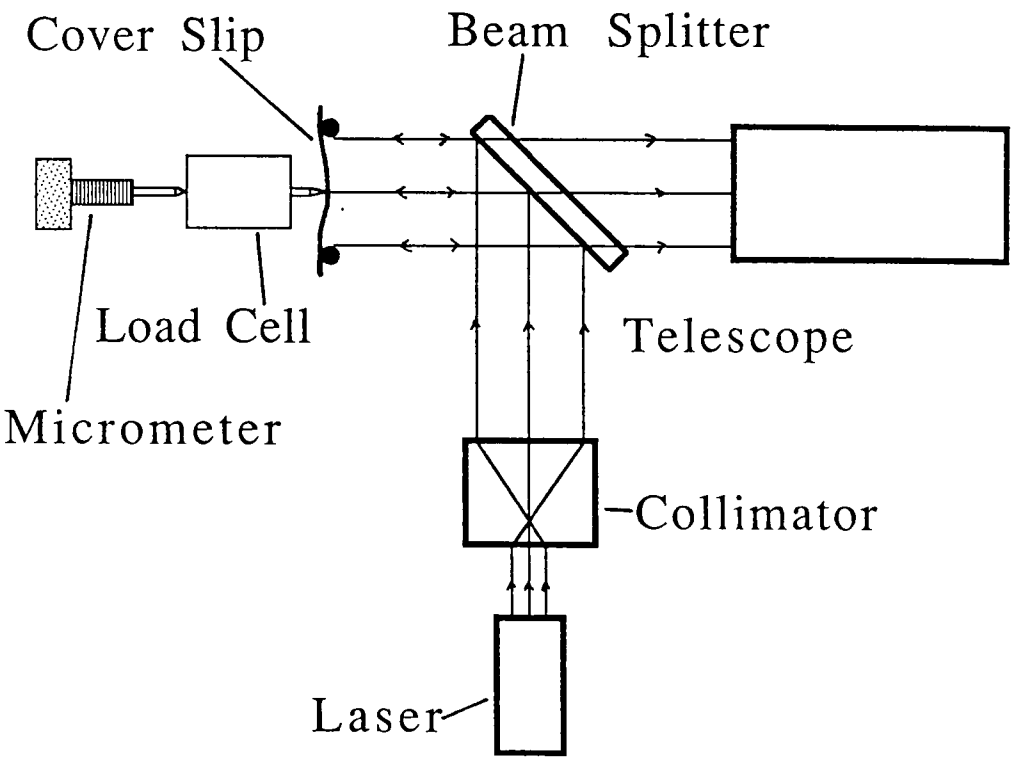


Figure 9.2. Schematic diagram of the optical system employed.

in the center of the aperture and that the force is applied normal to the surface the deformation of the cover slip will be cylindrically symmetric. In this case the sections of caustic surfaces observed will be circles. Because the caustics are being observed through a telescope the value of Z in equation 9.10 is infinity. This implies that the diameter of the caustics seen represents the slope of the surface at points on the circle where its second differential is zero.

If the load is sufficiently small that Hooke's law is obeyed the magnitude of the displacement of each point on the surface will be proportional to the applied force yet the shape of the surface can be assumed to remain constant. That is:

$$S(x) = F(x) \cdot P \qquad 9.11$$

where F(x) is a function describing the shape of the surface and P is the applied load. Under these conditions, the angular diameter of the caustic observed at infinity will be proportional to the applied force.

In order to evaluate the precision of this technique as a means of measuring small displacements the diameter of the observed caustic will be plotted as function of load. The magnitude of scatter of these points about the best fit straight line will be the random experimental error. In order to relate this measurement to actual displacement of the glass, the position of the glass as function of load will be measured by independent mechanical means. This

calibration will allow the precision of the system to be stated in terms of the displacement of the center of the cover slip.

The diffraction pattern decorating the caustic will be taken into account in two ways. The first order approximation that can be made is that the geometric caustic corresponds to either the first bright or first dark bands, whichever is sharpest. This contains a systematic error due to the change in the width of the diffraction pattern as the
diameter of the caustic changes, but could still yield a precise measurement of displacement. A more complete way of treating the data would be to fit the locations of several of the peaks and troughs of the diffraction profile to that expected and thus, by extrapolation, determine the location of the ray caustic.

Experimental Procedure

The arrangement of apparatus, shown schematically in figure 9.2 was set up on an optical bench.

The light source was a 0.95 mW, He-Ne laser of wave length 633 nm. The beam was expanded by a combination of a low power microscope objective lens and a lens of focal length 70 mm configured to yield a columnar beam 10 mm in diameter. The viewing telescope consisted of 140 mm focal length lens as the objective the image being viewed using a Nikon Micro-Nikkor 55 mm, f/2.8 lens in front of either a 35 mm camera or a video camera. The beam splitter was of the cubic prism type. Fine

adjustments of the lens-camera combination were made by focussing the image of a distant object. Unless otherwise specified, the optical equipment, and sundry bench accessories, were manufactured by Oriel corporation.

The object under investigation was a glass microscope coverslip of nominal thickness 0.15 mm manufactured by Fischer Scientific. It was pressed up against a washer by the force of a pin point located at its center and aligned perpendicular to its surface. The washer was, in turn pressed against a parallel sided vertical aperture of adjustable width. The washer and cover slip were held in place by the friction of the applied load. This force could be measured to the nearest gramme equivalent using a peizo-electric load cell. Washers of inner diameter 3.5 mm and 2 mm were used.

Once the circular section through the caustic could be observed the magnification of the telescope was adjusted, by changing the focal length of the camera, such that it was possible to photograph its entire disk for loads up to about half the failing load of the glass. The diffraction pattern surrounding the caustic was photographed for various loads in this range. The diameters of the various diffraction fringes were measured off of the 35 mm negatives using a travelling microscope arrangement. This was repeated using both sizes of washer.

An alternative method of measuring the diameter of the caustic was to move the objective lens of the telescope sideways using a micro-positioner (figure 9.3). Because the lens-camera

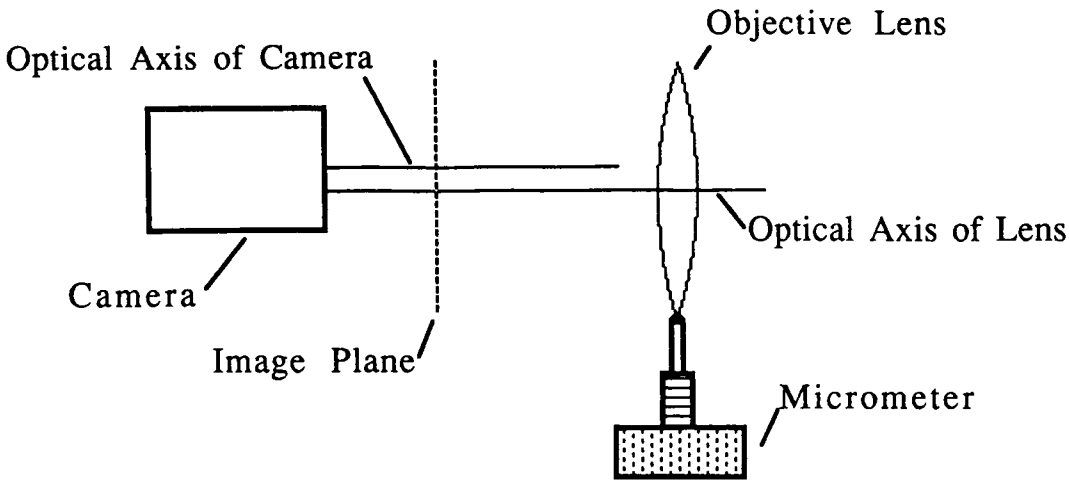


Figure 9.3. Measurement of the diameter of the caustic by transverse movement of the objective lens of the telescope.

combination was focussed to infinity the motion of the lens relative to the object is negligible. This allows direct measurement of the size the image as it exists at the focal plane of the objective. When using this method it is not necessary to simultaneously view the entire caustic eliminating any restrictions on the magnification employed. This technique allows the dimensions of the caustic to be measured in real time using the video camera and was employed using the 3.5 mm washer.

In order to relate the observed changes in the caustics to actual central displacement of the cover slip it was necessary to make an independent measure of this as a function of force. This was done by using the X-Y translation stage to scan a second pin point, held perpendicular to the cover slip, on the opposite side of the glass to the loading point. The moment at which this touches the surface could be found by observing the accompanying increase in the force registered on the load cell. The locus of coordinates at which this occurs was plotted for various values of load and the central displacement per unit force, that is, the elastic constant found.

Results

Figure 9.4 is a photograph of a typical observed section though the caustic. The first few Airy diffraction bands are visible, spun into circles by the symmetry of the situation. From this, the diameter of the underlying geometric caustic was found by plotting

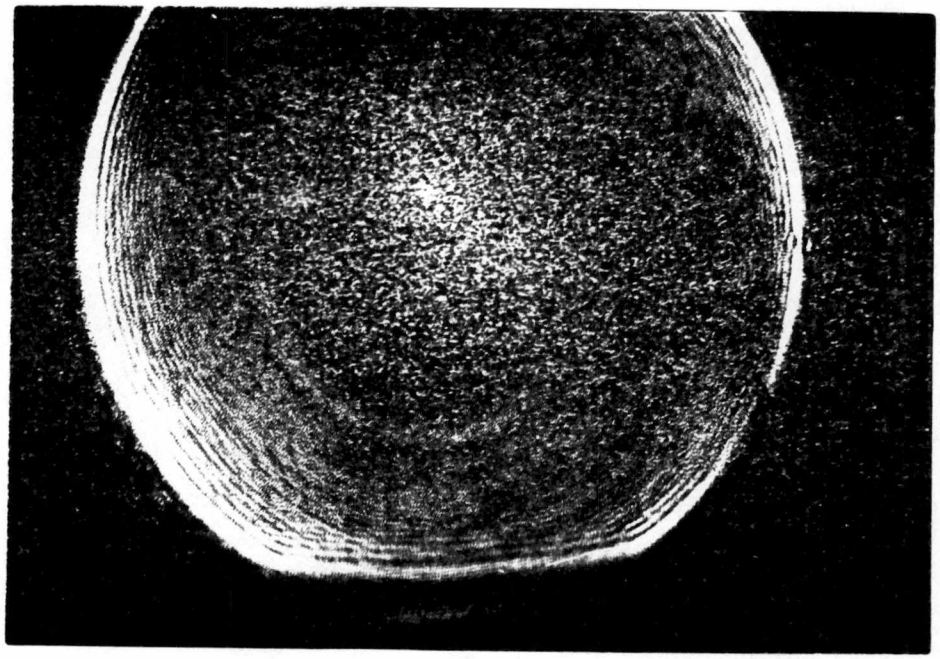


Figure 9.4. A typical section through a caustic.

the diameter of the center of each diffraction band against the value of the parameter, t, in the Airy function, $\Phi(t)$, predicted at that point of the diffraction pattern (figure 9.5). If the diffraction profile is that predicted by Airy, points plotted on such a graph should lie on a straight line. At the geometric caustic, t=0, therefore the diameter of the ray caustic can be read off as the intercept of the data line with the Y-axis. A straight line was fitted to the data and the diameter of the geometric caustic found in this manner.

The sequence of photographs of caustics formed using the 3.5 mm washer were analyzed in this way and the results are plotted in figure 9.6. The straight line predicted by Hooke's law was fitted to this data. Its slope was 0.0364 mm per gram. The residuals between this fit and the data are graphed in figure 9.7. By inspection it can be seen that the average spread of this data is 60 μm.

In order to relate this precision in the measurement of the caustic size to the equivalent precision in the measurement of displacement one needs to make use of the previously measured elastic constant of the system. For the 3.5 mm diameter washer the elastic constant was found to be 0.060 μm per gram. If the slope of the line in figure 9.6 is divided by this quantity the result is 0.61 mm per μm. That is, a 0.61 mm change in the diameter of the caustic represents a 1 μm displacement of the center of the cover slip. Given this information, the residuals plotted in figure 9.7 can

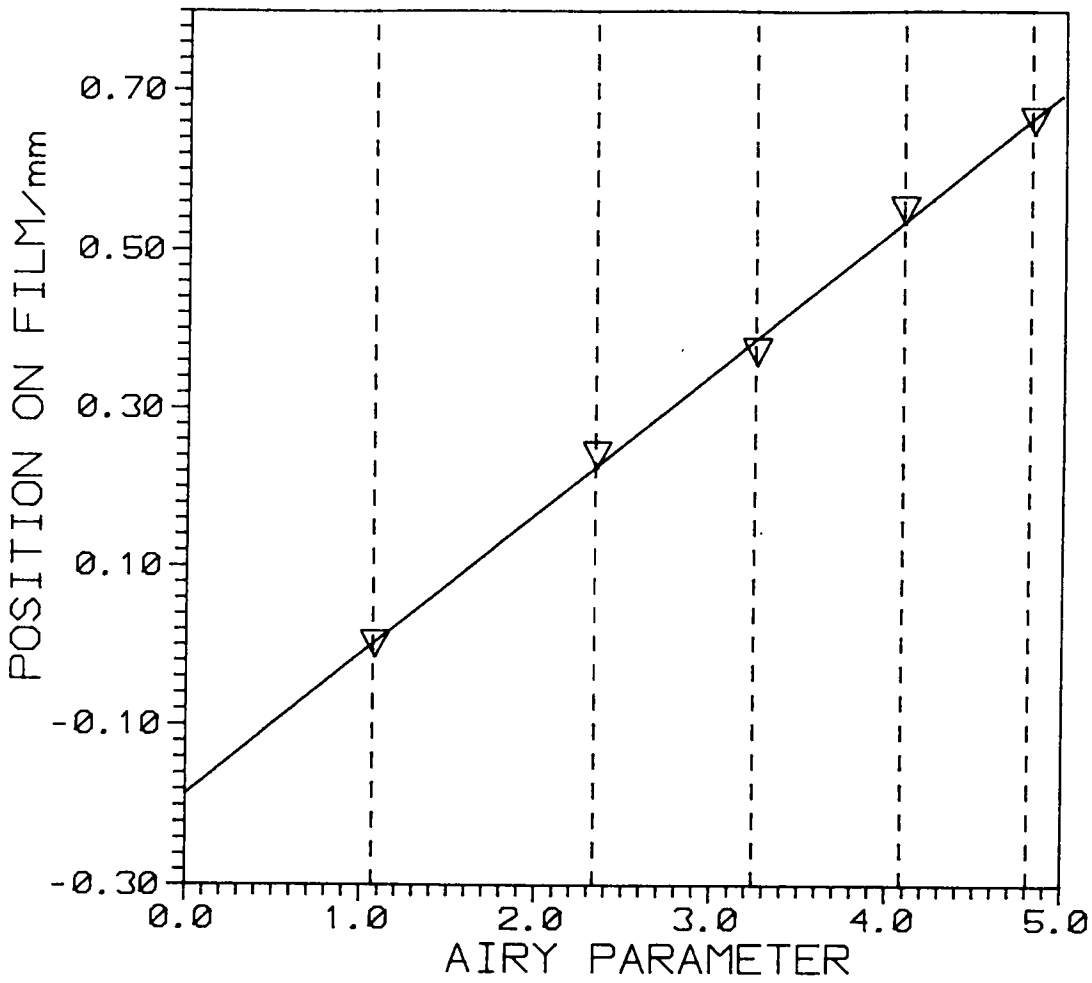


Figure 9.5. Location of the geometric caustic by extrapolating from the locations of the peaks and troughs of the diffraction pattern

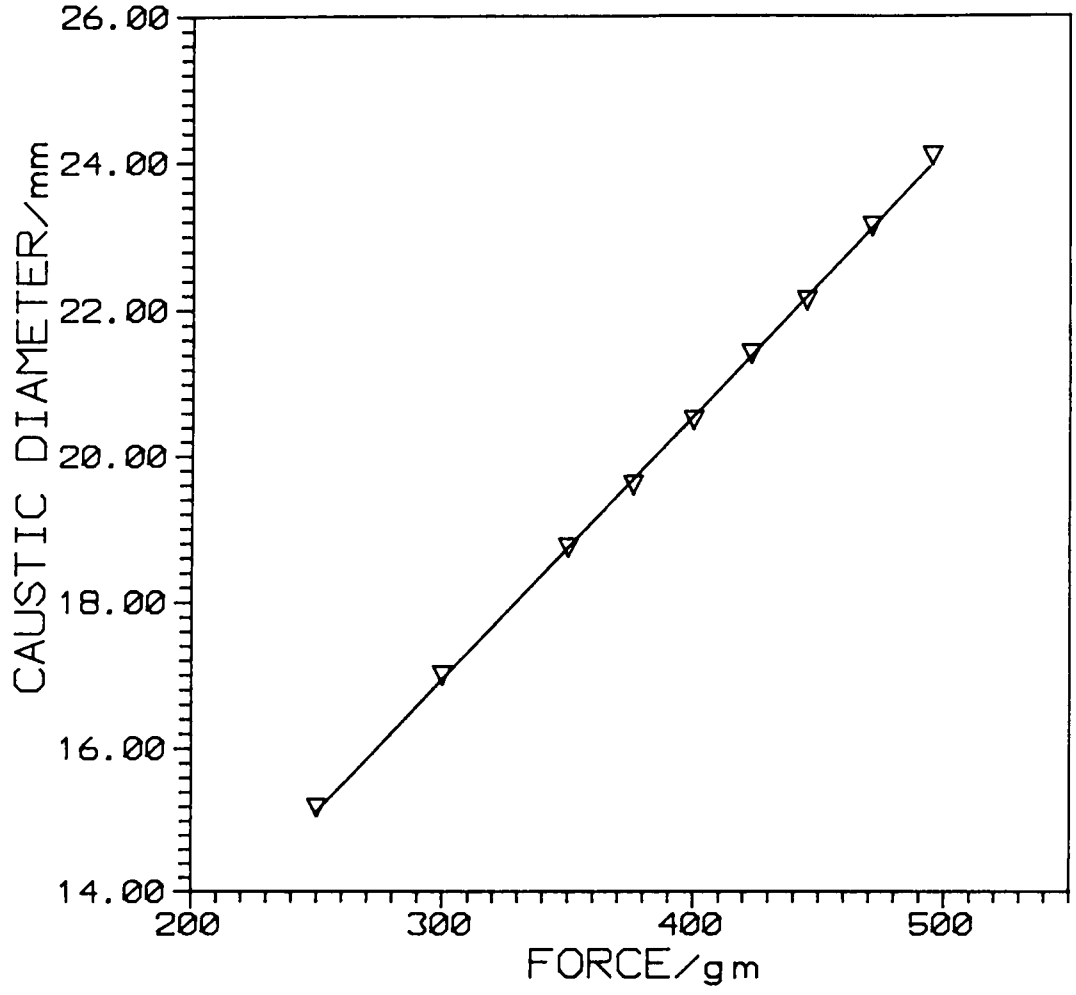


Figure 9.6. The diameter of the caustic as a function of the applied force.

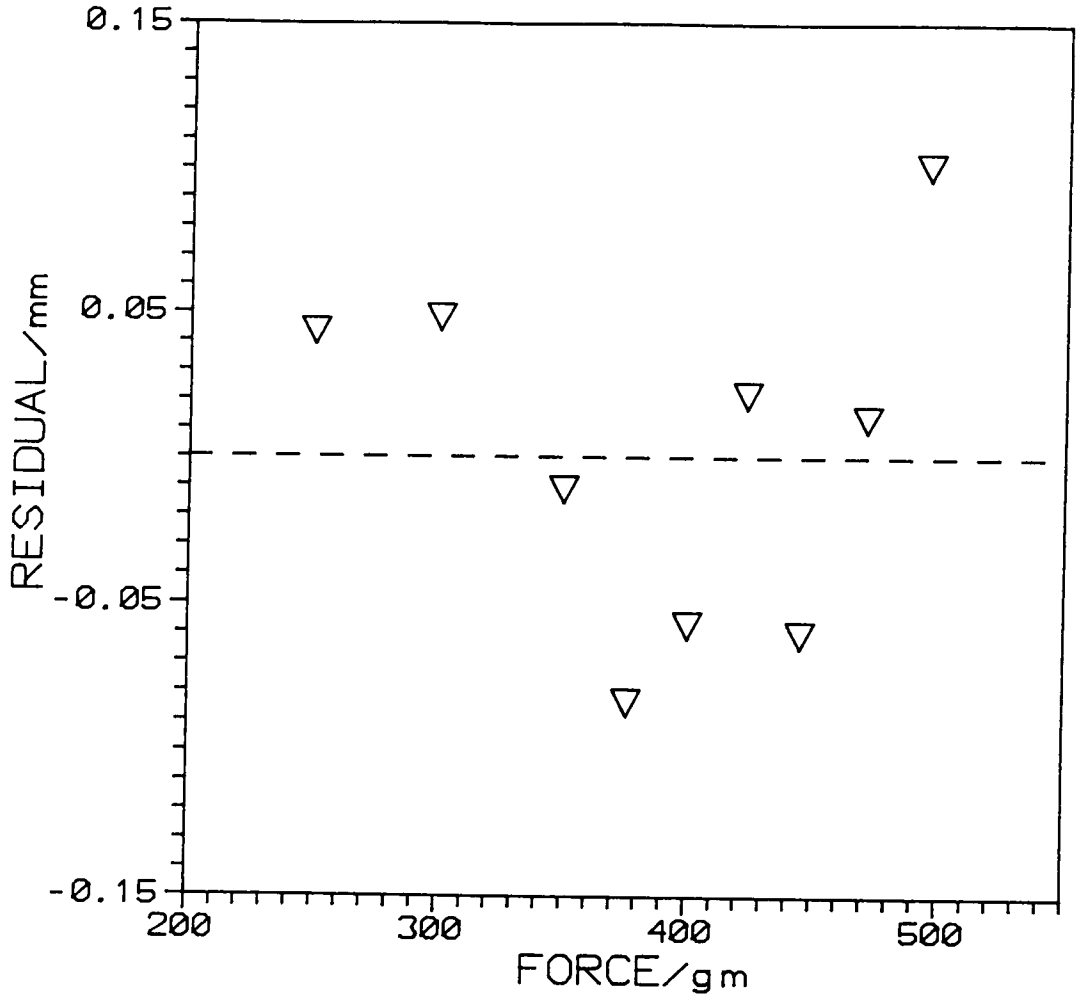


Figure 9.7. Residual plot.

be expressed in terms of nanometers of central displacement (figure 9.8). The spread of the data is approximately 100 nm.

From the slope of the data in figure 9.6, it can be deduced that the 60 μm spread in the data is equivalent to a 1.6 gram precision in the measurement of force. As this is close to the 1 gram sensitivity of the load cell a stiffer dependence of the displacement on the load is required. This is achieved by connecting the pin point to a separate member which is, in turn, loaded by the load cell (figure 9.9).

The dependance of caustic size on force for this amended system is shown in figure 9.10. Here the diameter of the caustic was taken to be that of the first dark band as measured by translating the telescope objective lens. The slope of fitted to this data is 0.0028 mm per gram. Calculating by the same method as above, this implies a measurement factor of 0.047 mm change in diameter per μm displacement. Given this, the residuals from the fit can be plotted (figure 9.11). The data appear to fit a parabolic curve so an extra, quadratic term was added to the fitting function. The residual displacements from this curve are shown in figure 9.12. The majority of the points fall within 40 nm of their mean value.

In a search for a greater degree of precision the above was repeated using the smaller, 2 mm hole diameter, washer. The caustic was photographed and its diameter measured by extrapolating the diameters of the diffraction bands. The variation of caustic diameter as a function of force was fitted to a straight

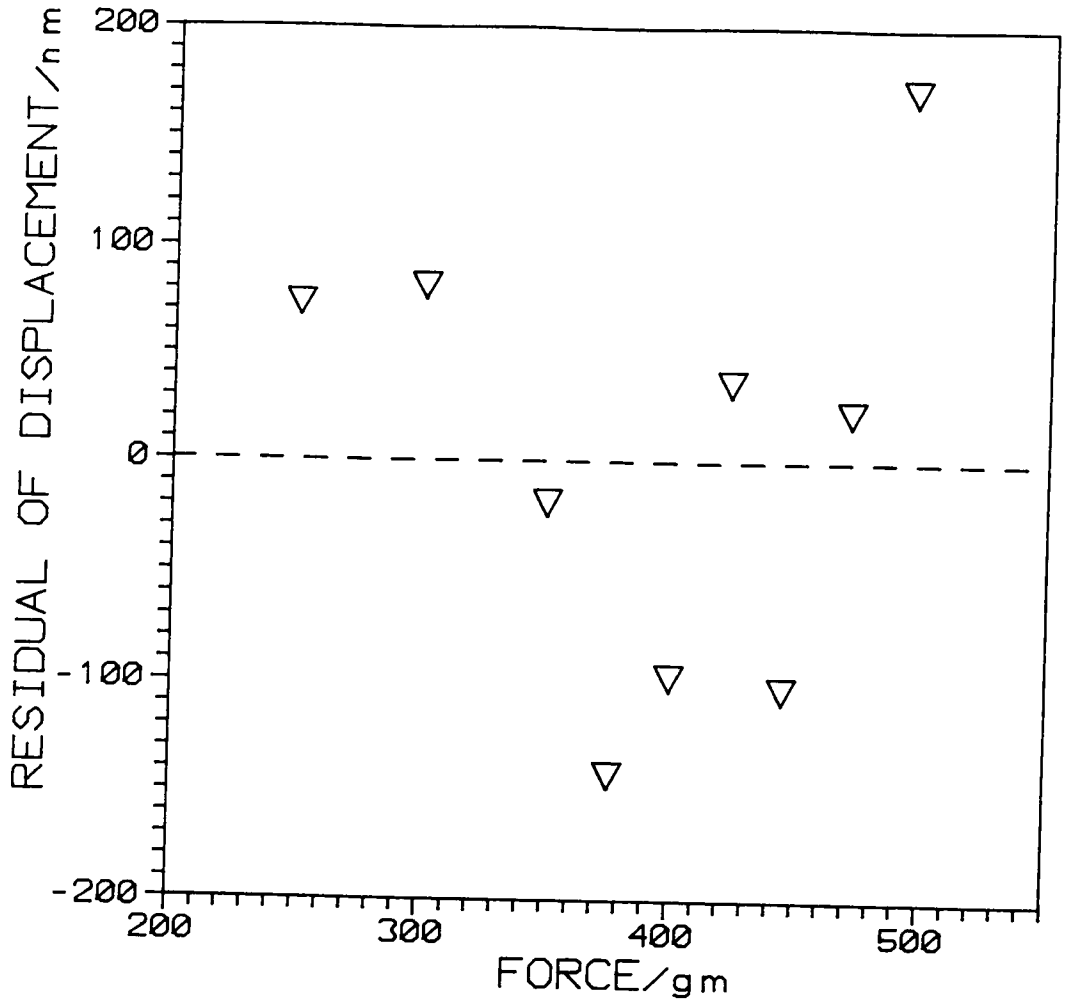


Figure 9.8. Plot of the residuals expressed in terms of the central displacement.

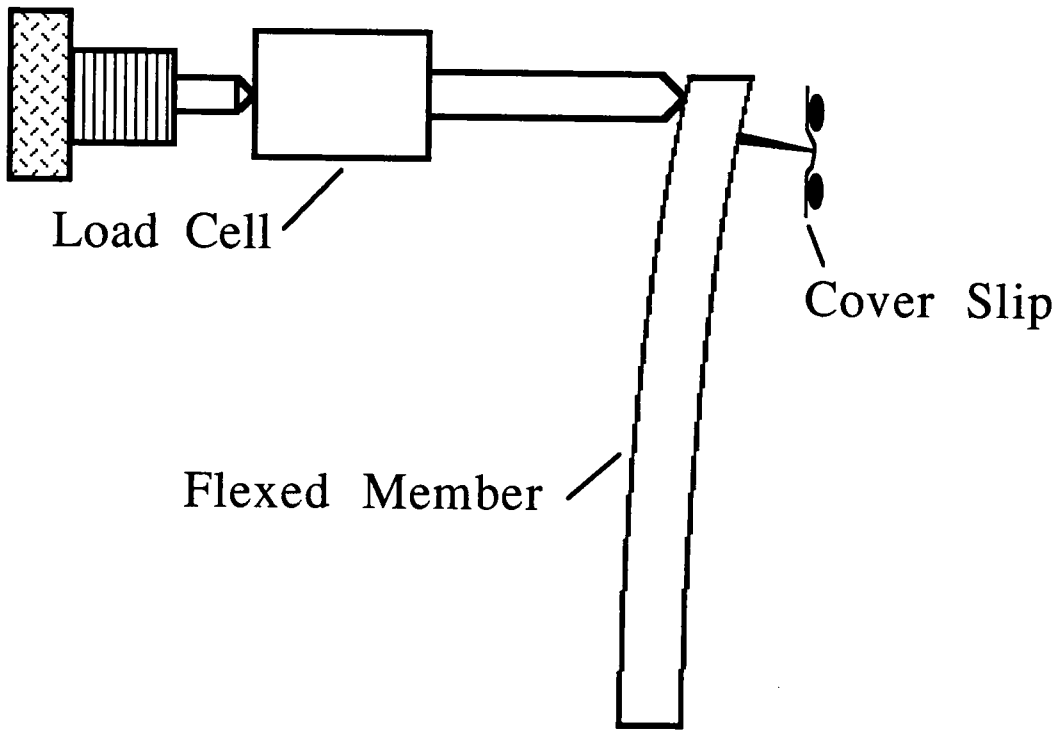


Figure 9.9. Increasing the precision by introducing an extra member between the load cell and the specimen.

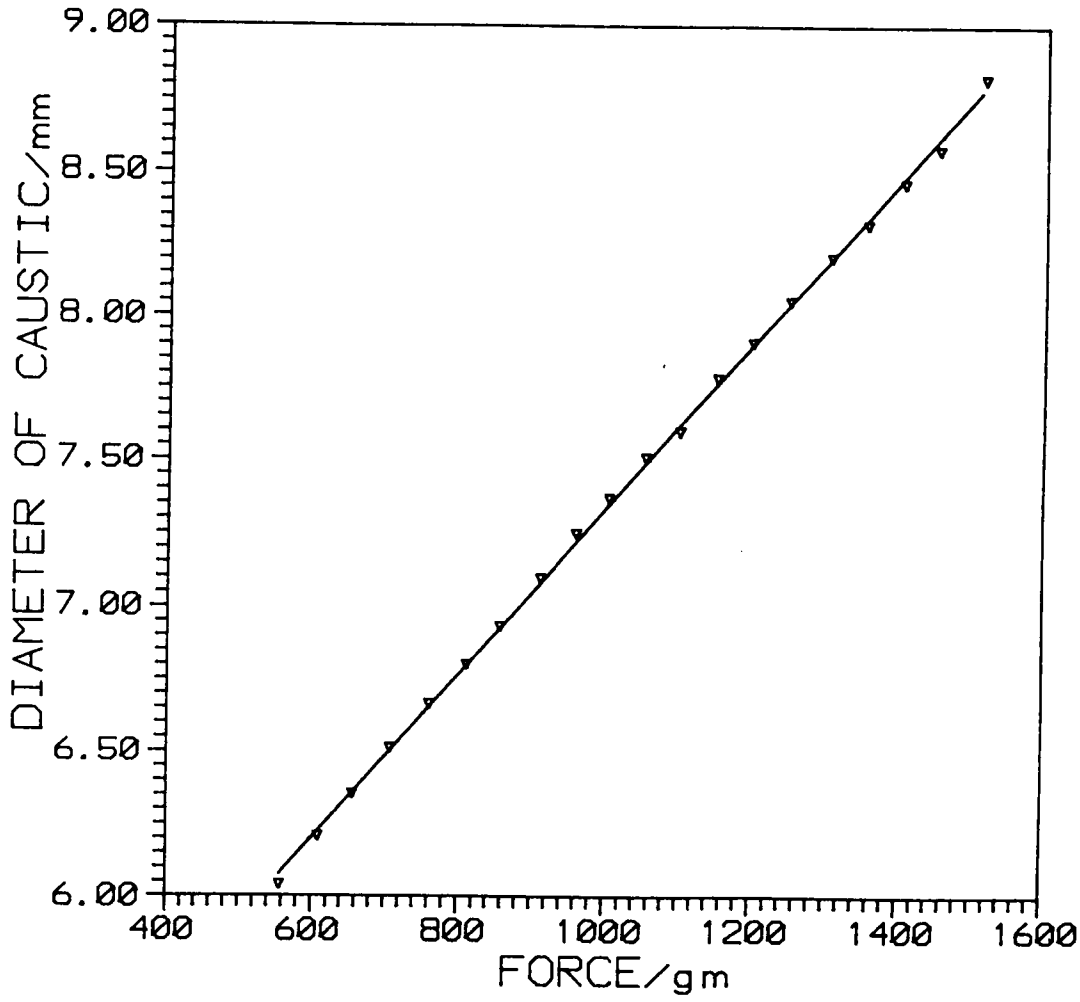


Figure 9.10. Diameter of the caustic as a function of the applied force when using the stiffened system.

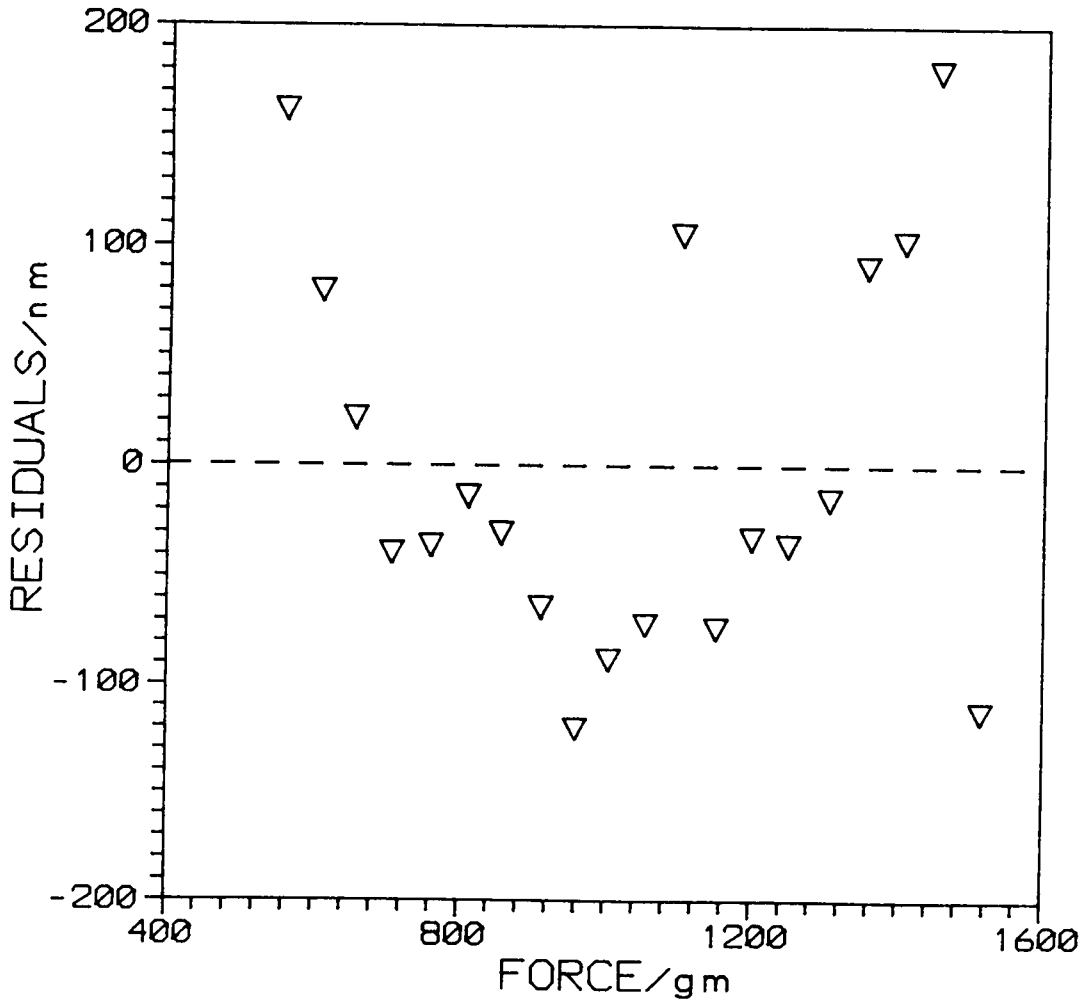


Figure 9.11. Residual plot expressed in terms of the central displacement for the stiffened system.

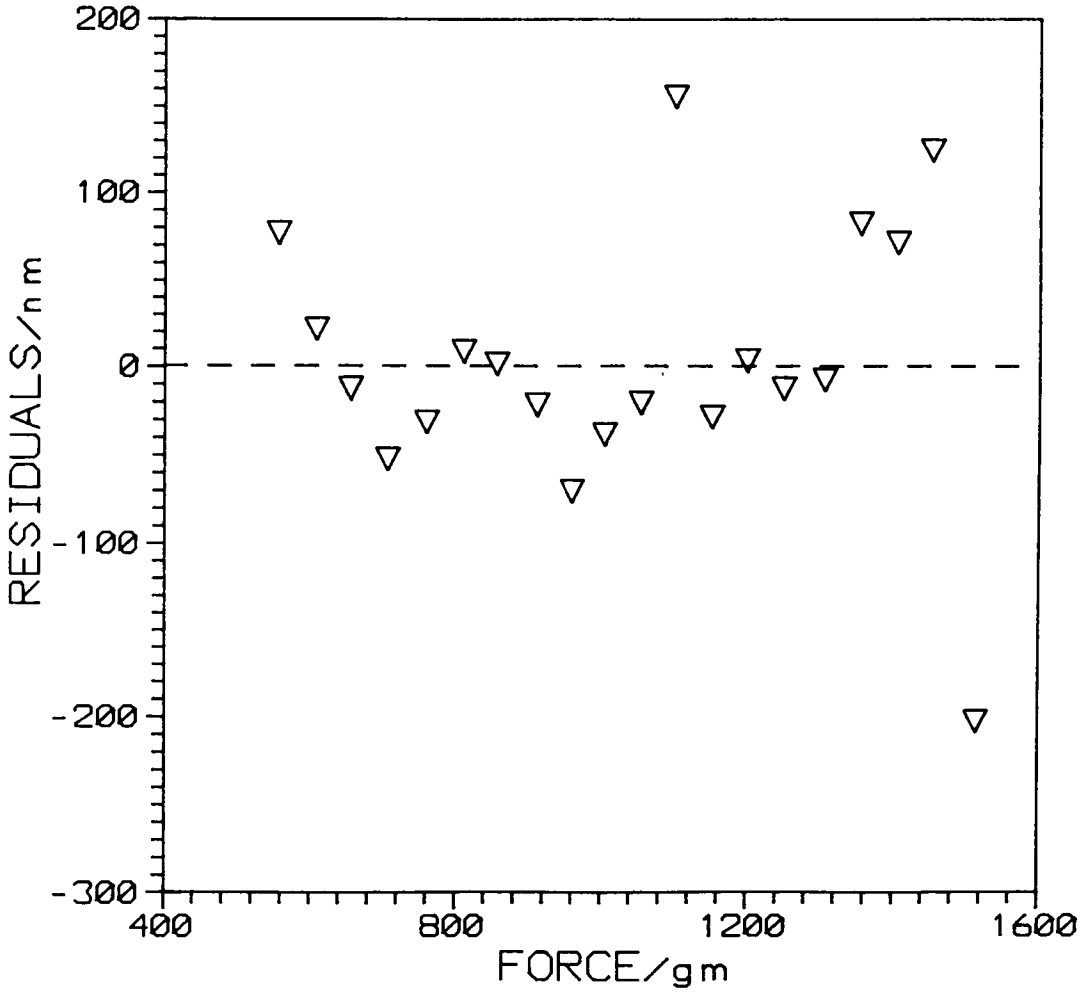


Figure 9.12. Residuals from a parabolic fit to the data.

line of gradient 0.019 mm per gram (figure 9.13). The measured elastic constant of the specimen was 0.022 μm per gram equivalent force. Dividing the gradient of the fit in figure 9.13 by this figure yields a magnification of 0.86 mm per μm of central displacement. Plotting the residuals, converted to central displacement according to this relationship, shows a precision of 120 nm in the measurement figure 9.14.

Discussion

The above experiments demonstrate that it is possible to obtain a precision in displacement measurement using caustics that is less than the wave length. The best precision of about 40 nm was achieved laterally translating the objective lens and measuring the positions of the fringes in real time. This precision is one sixteenth of the wavelength which is almost twice that which can be achieved, on a similar specimen, by interferometric techniques.

Even though, when the smaller washer was employed, a given caustic diameter represents a smaller displacement the measurement was less precise. This was because the diffraction pattern in this case was broader and the centers of the bands were harder to identify. If the broadening was due to aperture diffraction, this may be evidence of a limit in the extent to which the precision may be increased by making the sample smaller.

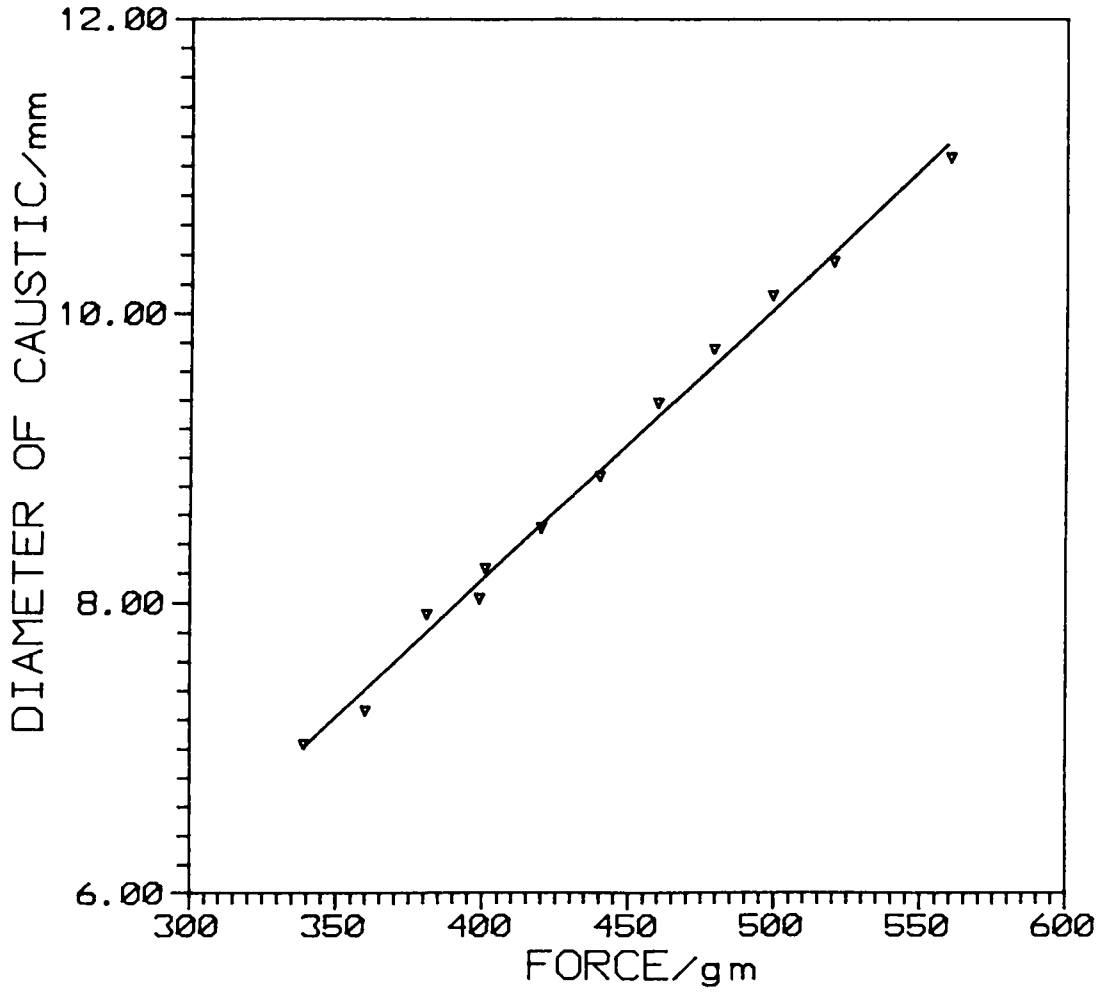


Figure 9.13. Diameter of the caustic as a function of the applied force when using the 2mm hole.

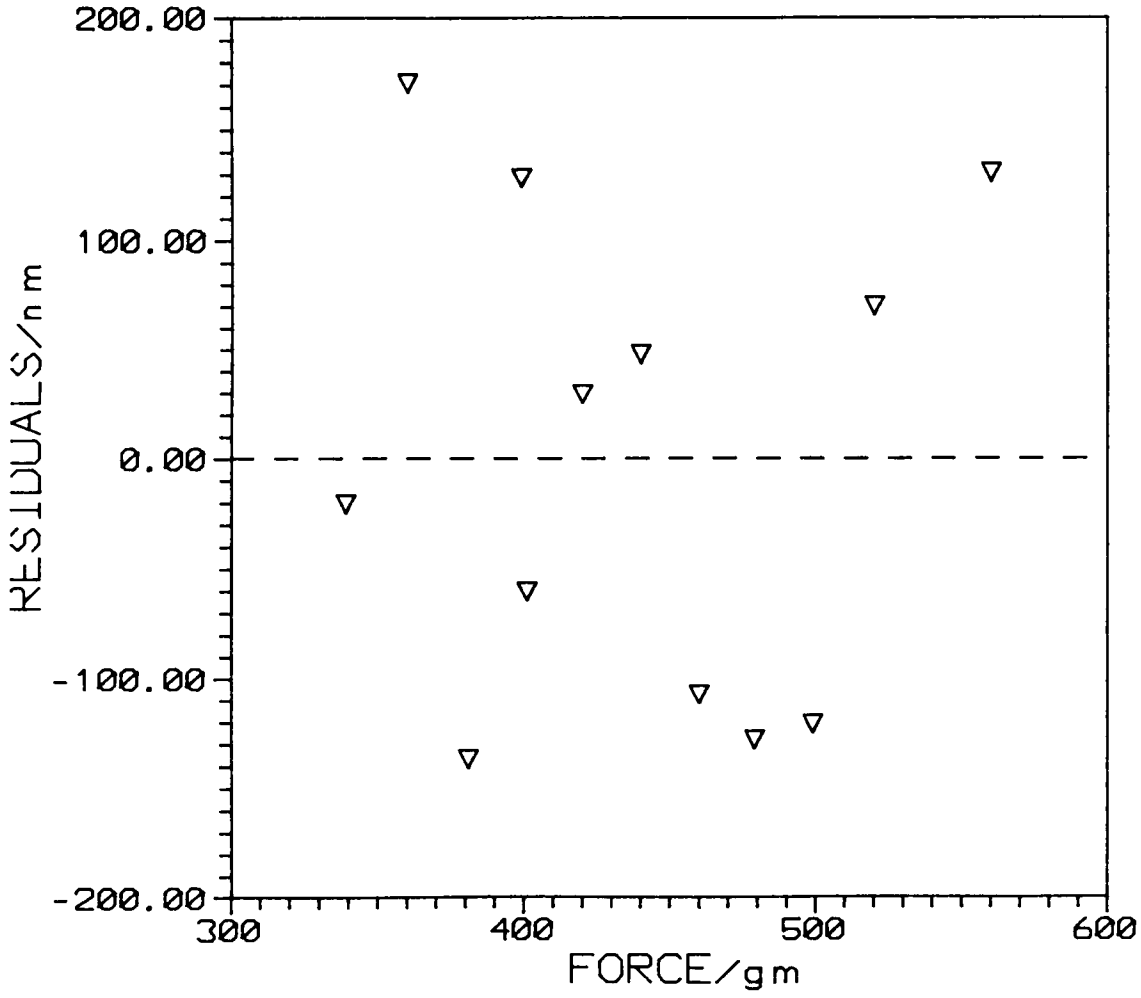


Figure 9.14. Residual plot expressed in terms of the central displacement for the 2mm hole.

Here the precision is limited by the crude method by which the diffraction pattern was evaluated. Its true limit will only be found by taking the actual diffraction profile and fitting the Airy function to it; not just at the maxima and minima but across the whole profile. Given this, the work presented here demonstrates to precision possible without this extra analysis.

The system employed here is an optical lever in which the reflecting mirrors are intrinsic to the specimen and within a few millimeters of each other. This has the advantage of making the measurement relatively immune to vibrations compared to other techniques of similar precision.

CHAPTER 10

CONCLUSIONS

The value of wave field dislocations and caustics to materials characterization has been demonstrated.

The experiments presented in chapters four and five showed how dislocations can serve to quantify the level of complexity of a wave field, and thus, yield information about the interaction between the wave and the specimen. In chapter six, the fact that the dislocations constitute precisely defined markers in the wave field was successfully applied to the measurement of changes in a corroding system that occur over a period of days. If would be of great interest to apply this property of dislocations to the measurement of small changes in surface characteristics or metallic microstructure.

The region of high wave amplitude near a caustic surface was successfully employed in a high depth of field acoustic imaging system.

Although caustics offer a means of measuring the shape of a microscopic reflecting surface, the inversion algorithm investigated was not sufficiently sophisticated to distinguish real ray paths from artifacts.

As markers in the wave field, caustics could be exploited to measure the displacement of a surface to within 40 nm.

LIST OF REFERENCES

LIST OF REFERENCES

Abramowitz M., Stegun I.A. Handbook of Mathematical Functions, National Bureau of Standards Applied Mathematics Series 55, Washington D.C., 1964.

Airy G.B. Trans. Cambridge Philos. Soc., vol. 6, 379-403, 1838.

A.S.M. "Metals Handbook", American, Society of Metals, Metals Park, Ohio,1988.

Berry M.V. "Singularities in Waves and Rays" in "Les Houches Summer School 1980- Physics of Defects" ed. Balian R., Kleman M., Poirier J.P., vol. XXXV, pp. 453-543, North Holland, Amsterdam, 1981.

Berry M.V., Upstill, C. "Catastrophe Optics: Morphologies of Caustics and their Diffraction Patterns" in "Progress in Optics" ed. Wolf E., vol. XVIII, North Holland, Amsterdam, pp. 257-346, 1980.

Born M., Wolf E. "Principles of Optics", 3rd. ed., Pergamon Press, New York, 1964.

Braunbek, Laukien Optik, vol. 9, p. 174, 1952.

Brewster J.R. "Some Applications of Caustic Foci to Non-Destructive Evaluation", M.S. Thesis, University of Tennessee, Knoxville, 1989.

Descartes R. Meteorology, 1637.

Fitting D.W., Adler L. "Ultrasonic Spectral Analysis for Non-Destructive Evaluation", Plenum Press, New York, 1981.

Hatch J. E. "Aluminum, Properties and Physical Metallurgy", American Society for Metals, Metals Park, Ohio, 1984.

Krautkramer J., Krautkramer H. "The Ultrasonic Testing of Materials", 3rd ed., Springer Verlag, Berlin,1983.

Kuhn T.S. "The Structure of Scientific Revolutions", University of Chicago Press, 1962.

Landau L., Lifshitz E. "The Classical Theory of Fields", 1st ed., Addison-Wesley, Cambridge Ma., 1951.

Lupis C.H.P. "Chemical Thermodynamics of Materials", North-Holland, Amsterdam, 1983.

Nye J.F., Berry M.V. Proc. Roy. Soc. Lond.,vol. 336, pp. 165-190,1974.

Papadakis E.P. "Ultrasonic Attenuation Caused by Scattering in Polycrystalline Media" in "Physical Acoustics" vol. IV, ed. Mason W.P., Academic Press, New York, 1968.

Poston T., Stewart I. "Catastrophe Theory and Its Applications", Pitman, 1978.

Stavroudis O.N. "The Optics of Rays, Wavefronts and Caustics", Academic Press, New York, 1972.

Theocaris P.S., Gdoutos E. J. Applied. Mechanics, March 1972, p. 91.

Walford M.E.R., Holdorf P.C., Oakberg R.G. J. Glaciology, vol 18, no. 79, 1977.

Weast (ed.) "C.R.C Handbook of Chemistry and Physics", 67th ed., C.R.C. Press Boca Raton, Florida, 1986.

Whetwell W. Phil. Trans. Roy. Soc. Lond., vol.123, p.289, 1836.

Wood R.W. "Physical Optics", 2nd ed., MacMillan, New York, 1911.

Wright F.J. "Wavefront Dislocations and Their Analysis Using Catastrophe Theory" in "Structural Stability in Physics", ed. Guttinger W., Eikeneier H., pp. 141-156, Springer Verlag, Berlin, 1979.

Wright F.J., Berry M.V. J. Accoust. Soc. Am., vol 75, no. 3, 1984.

APPENDICES

APPENDIX A

COMPUTER PROGRAM REFERENCED IN CHAPTER 4

Addpulse.bas

```
10 REM      MODELS THE DISLOCATIONS IN THE ULTRASONIC SOUND FIELD REFLECTED
11 REM      FROM A ROUGH SURFACE

12 REM      WRITTEN IN VAX BASIC


13 REM      VARIABLES USED:

14 REM      DCNT:  TOTAL NUMBER OF DISLOCATIONS DETECTED
15 REM      D:     DISTANCE BETWEEN THE TEST POINT AND
                   THE SPECIMEN (mm)
16 REM      RR:    RADIUS OF THE BEAM PROFILE (mm)
17 REM      VEL:   SPEED OF SOUND IN WATER (mm/MICROSECOND)
18 REM      FREQ:  CENTRAL FREQUENCY OF THE PULSE (MHz)
19 REM      LAM:   WAVELENGTH CORRESPONDING TO THE CENTRAL FREQUENCY
                   (mm)
20 REM      X,Y:   COORDINATES OF THE TEST POINT (mm)
21 REM      W:     ANGULAR FREQUENCY (MRad/s)
22 REM      TMO:   STARTING TIME OF THE SEARCH PROCEEDURE (MICROSECONDS)
23 REM      TMX:   MAXIMUM VALUE OF TIME PERMITTED IN THE SEARCH
24 REM      TMN:   MINIMUM VALUE OF TIME PERMITTED IN THE SEARCH
25 REM      MX:    MAXIMUM ABSOLUTE VALUE OF X (mm)
26 REM      STP:   STEP SIZE IN X-DIRECTION
27 REM      TSTP:  STEP SIZE IN TIME-DIRECTION
28 REM      PASS:  DISTANCE IN X TRAVERSED BEFORE RENEWAL OF THE SCATTERING
                   SURFACE (mm)
29 REM      SDX:   X-SIDE OF THE SCATTERING SURFACE (mm)
30 REM      SDY:   Y-SIDE OF THE SCATTERING SURFACE (mm)
31 REM      NM:    NUMBER OF REFLECTING POINTS ON THE SURFACE
32 REM      RHO:   DENSITY OF REFLECTING POINTS ON THE SURFACE
                   (PER SQUARE mm)
33 REM      RN:    NUMBER OF PASSES PERFORMED
34 REM      T0:    PREVIOUS VALUE OF T
35 REM      X0:    PREVIOUS VALUE OF X
36 REM      DIRN:  DIRECTION OF MOTION:
            DIRN=1, POSITIVE X-DIRECTION
            DIRN=2, POSITIVE T-DIRECTION
            DIRN=3, NEGATIVE X-DIRECTION
            DIRN=4, NEGATIVE Y-DIRECTION
37 REM      FT:    FIRST DIFFERENTIAL OF THE SIGNAL
38 REM      FTT:   SECOND DIFFERENTIAL OF THE SIGNAL


50 REM      Y(N):  Y-COORDINATE OF THE Yth REFLECTOR
52 REM      X0(N): PREVIOUS VALUES OF X
```

```
53 REM          T0(N): PREVIOUS VALUES OF T
54 REM          SN(N): CODES DIRECTION OF MOTION
55 REM          R(N):  CODES REASON WHY THE PASS FAILED


69 REM          SET THE INITIAL VALUES OF VARIABLES

70  dcnt=0\D=2.35\RR=1\VEL=1.49\FREQ=20\LAM=VEL/FREQ\RRS=RR*RR\Y=0\X=0
73 W=2*PI*FREQ\TMO=3.21\NSTP=1\DB=0

75  DIM  X(9000),Y(9000),SN(4),X0(2999),T0(2999),R(10)

78 RHO=10\DMAX=1000\PRINT "RHO=";RHO,"DMAX=";DMAX

80  PASS=50\PASS=PASS/1000
82 PRINT "SCAN DISTANCE=";PASS*1000;"MICRONS"
83  STP=0.001\MX=2.1*PASS\TSTP=STP/VEL

85 SDX=MX+2*RR\ SDY=2*RR
86 NM=INT(RHO*SDX*SDY)\PRINT "NUMBER OF REFLECTORS";NM

90 X=0\RANDOMIZE
95 TMN=3.16\TMX=3.5

120 GOSUB 5000\ REM  CREATE THE REFLECTING SURFACE.

130 RN=RN+1

200 GOSUB 7000\ REM  FIND THE FIRST ZERO OF THE SECOND DIFFERENTIAL
201 REM              BEYOND THE STARTING TIME, TMO.

210 DIRN=1


300 REM          FOLLOWING THE ZERO OF THE SECOND DIFFERENTIAL IN X-T SPACE.

308 REM          FIND THE SIGN OF THE SECOND DIFFERENTIAL AT THE SIDES
309 REM          OF A SQUARE.

310 X=X0+STP\T=T0\GOSUB 1000\SN(2)=SGN(FTT)
320 T=T0+TSTP\GOSUB 1000\SN(3)=SGN(FTT)
330 X=X0\T=T0\GOSUB 1000\SN(1)=SGN(FTT)
340 T=T0+TSTP\GOSUB 1000\SN(4)=SGN(FTT)

343 IF SN(1)=SN(3) AND SN(2)=SN(4) AND SN(1)<>SN(2) THEN 900

348 REM          FINDING THE VALUE OF THE NEW DIRECTION OF TRAVEL

350 IF DIRN=4 THEN 370
360 IF SN(2)<>SN(3) THEN X0=X0+STP\DIRN=1\T=T0+TSTP/2\X=X0\GOTO 500
370 IF DIRN=3 THEN 390
380 IF SN(4)<>SN(3) THEN T0=T0+TSTP\DIRN=2\T=T0\X=X0+.5*STP\GOTO 500
390 IF DIRN=2 THEN 410
400 IF SN(1)<>SN(2) THEN T0=T0-TSTP\DIRN=3\T=T0+TSTP\X=X0+.5*STP\GOTO 500
410 IF DIRN=1 THEN 430
```

```
420 IF SN(1)<>SN(4) THEN X0=X0-STP\DIRN=4\T=T0+.5*TSTP\X=X0+STP\GOTO 500
430 R(3)=R(3)+1\ GOTO 9000


500 REM FOUND ZERO IN SECOND DIFFERENTIAL

501 IF DIRN=4 OR DIRN=1 THEN DTOT3=DTOT3+STP
502 IF FT>0 THEN 505
503 IF DIRN=1 OR DIRN=4 THEN DTOT2=DTOT2+STP

505 IF DTOT3>PASS THEN 8500\REM    TOTAL DISTANCE TRAVELED EXCEEDS PASS.

506 IF T0<TMN OR T0>TMX THEN R(6)=R(6)+1\GOTO 9000
508 CNT=CNT+1\IF CNT>1000 OR NSTP>2500 THEN R(2)=R(2)+1\GOTO 9000
510 IF TCNT>1000000 THEN 10000

515 GOSUB 8000\ REM  CHECK IF DOUBLING BACK
516 IF DB>2 THEN DB=0\R(1)=R(1)+1\ GOTO 9000

520 IF X0>MX/2 THEN R(5)=R(5)+1\GOTO 9000
530 IF X0<-MX/2 THEN R(4)=R(4)+1\GOTO 9000

533 IF SFTO=0 THEN  SFTO=SGN(FT)\ GOTO 550
536 IF SFTO<0 AND FT>0 THEN NDIS=NDIS+1
539 SFTO=SGN(FT)

550 GOTO 300

900 REM         BYPASSING CROSSING POINTS

910 IF DIRN=1 THEN X0=X0+STP\GOTO 300
920 IF DIRN=2 THEN T0=T0+TSTP\GOTO 300
930 IF DIRN=3 THEN T0=T0-TSTP\GOTO 300
940 IF DIRN=4 THEN X0=X0-STP\GOTO 300
950 GOTO 10000



1000 REM              FOR A GIVEN X AND T RETURNS THE FIRST TWO DIFFERENTIALS
1001 REM              OF THE SIGNAL RECEIVED.

1004 FT=0\FTT=0


1010 FOR N=1 TO NM\REM              SUMMING THE CONTRIBUTIONS FROM NM
                                    SCATTERERS.

1020  R=Y(N)*Y(N)+(X-X(N))^2
1030 IF R>RRS THEN 1090\REM         REFLECTOR OUTSIDE OF THE BEAM.
1035 R=SQR(R)
1040  AMP=1-R/RR\REM        TRANSDUCER'S BEAM CHARACTERISTICS.
1050 DIST=R*R+D*D\AMP=AMP/DIST
1053 DIST=2*SQR(DIST)\REM  DISTANCE TO THE REFLECTING POINT.
1055 TAU=DIST/VEL\REM      TIME OF FLIGHT ASSOCIATED WITH THAT RAY.
1058 TMT=T-TAU\REM         "T MINUS TAU".
```

```
1060 A=-1800\IF TMT<0 THEN A=200000
1066 IF (A*TMT*TMT*TMT)<-9 THEN 1090

1067 EPN=EXP(A*TMT*TMT*TMT)
1069 CWT=COS(W*TMT)\SWT=SIN(W*TMT)
1070 FT=FT+AMP*EPN*(W*CWT+3*A*TMT*TMT*SWT)
1073 FTT=FTT+AMP*EPN*(SWT*(9*A*A*TMT*TMT*TMT*TMT+6*A*TMT-
W*W)+CWT*(6*A*TMT*TMT*W))

1090 NEXT N


1111 RETURN



5000 REM                SETS SCATTERERS IN ARRAY.
5005 SDX=MX+2*RR
5006 SDY=2*RR
5007 NM=INT(RHO*SDX*SDY)

5010 FOR P=1 TO NM
5020  X(P)=SDX*(RND-.5)
5030  Y(P)=SDY*(RND-.5)
5050 NEXT P

5052 FOR N=1 TO NSTP
5054  X0(N)=0\ T0(N)=0
5056 NEXT N

5058 NSTP=1\FIRST=0\DTOT2=0

5060 RETURN



7000 REM                FINDS STARTING TIME LEVEL.
7003 TCNT=CNT+TCNT\CNT=0
7005 T=TMO\GOSUB 1000
7010 SN=SGN(FTT)

7020 T=T+TSTP/5
7030 GOSUB 1000
7050 IF SGN(FTT)<>SN AND FT<0 THEN 7100
7060 SN=SGN(FTT)
7080 GOTO 7020

7100 T0=T-TSTP\X0=X
7110 SN=SGN(FT)
7120 TFIRST=T
7199 RETURN
```

```
8000 REM                CHECKS IF DOUBLING BACK.
8005 DB=0
8010 FOR N=1 TO NSTP
8020 IF ABS(T0-T0(N))<TSTP*.1  AND  ABS(X0-X0(N))<STP*.1 THEN DB=DB+1

8040 NEXT N

8060 NSTP=NSTP+1
8070 X0(NSTP)=X0
8080 T0(NSTP)=T0

8099 RETURN


8500 REM END OF PASS
8505 NS=NS+1
8510 DTOT=DTOT+DTOT2
8520 GOSUB 1000
8540 DCNT=DCNT+NDIS
8600 IF NDIS>0 AND DCNT=100*INT(DCNT/100) THEN PRINT
DTOT,DCNT,DCNT/DTOT,NS,NS/D,CNT
8700 DTOT3=0\DTOT2=0\NDIS=0\SFTO=0

8990 IF DCNT<DMAX THEN 90
8995 GOTO 9200



9000 IF DTOT>0 THEN PRINT DTOT,DCNT,DCNT/DTOT,NSTP,DCNT-DCNTO
9010 DCNTO=DCNT
9100 IF DCNT<DMAX THEN 90

9198 REM                IF PASS ENDS BEFORE THE TEST POINT MOVES THE
9199 REM                PREDESCRIBED DISTANCE PRINTS THE REASON WHY.

9200 PRINT R(1);" DOUBLED BACK"
9210 PRINT R(2);" COUNTED OUT"
9230 PRINT R(4);" OFF LOWER END"
9240 PRINT R(5);" OFF UPPER END"
9250 PRINT R(6);" OFF END OF TIME RANGE"

10000 END
```

APPENDIX B

COMPUTER PROGRAM REFERENCED IN CHAPTER 7

Imgen.bas

```
10 REM      TAKES THE EXPERIMENTAL DATA AND GENERATES AN IMAGE

20 REM      WRITTEN IN VAX BASIC.


30 REM      VARIABLES USED:

31 REM      X:      X-COORDINATE, AS MEASURED BY THE MICROMETER.
31 REM      T:      TIME OF FLIGHT, AS MEASURED BY THE OSCILLOSCOPE.
32 REM      Y:      Y-COORDINATE, CALCULATED FROM THE TIME OF FLIGHT.
33 REM      A:      AMPLITUDE OF THE ECHO SIGNAL.
34 REM      W:      TEMPORAL WIDTH OF THE ECHO SIGNAL AT HALF MAXIMUM.
35 REM      V:      SPEED OF SOUND IN WATER.
36 REM      THRES:          THRESHOLD AMPLITUDE BELOW WHICH ALL AMPLITUDES
37 REM                      ARE ASSUMED TO BE ZERO.
38 REM      TSTP:   TEMPORAL SEPARATION BETWEEN THE GENERATED
39 REM              DATA POINTS.

41 REM              ALL TIMES ARE IN MICROSECONDS, DISTANCES IN MILLIMETERS
42 REM              AND AMPLITUDES IN VOLTS.


45 REM              DATA FILES:

46 REM      "INPUT.DAT":  CONTAINS THE RAW EXPERIMENTAL DATA.
47 REM      OUTPUT.DAT":  DATA POINTS FROM WHICH THE IMAGE CAN BE PLOTTED.


50 V=1.49\THRES=.1

100 OPEN "INPUT.DAT" FOR INPUT AS #1
110 OPEN "OUTPUT.DAT" FOR OUTPUT AS #2

300 INPUT #1,X
310 INPUT #1,T
320 INPUT #1,A
330 INPUT #1,W

340 IF X<-100 THEN 9000\REM          LARGE NEGATIVE VALUE SIGNALS THE END OF THE
341 REM                              DATA FILE

345  W=W/2\TSTP=W/2

400 FOR TAU=T-W*3 TO T+W*3 STEP TSTP
405  AA=.6931/(W*W)
```

```
410 AMP=A*EXP(-AA*(T-TAU)^2)\REM                GAUSSIAN SIGNAL PROFILE
411 REM                                         ASSUMED.
420 IF AMP<THRES THEN 500

430 Y=TAU*V/2\REM           SIMPLE RELATIONSHIP BETWEEN Y AND T BASED ON THE
431 REM         ASSUMPTION OF A STRAIGHT CAUSTIC.

450 PRINT #2,X
451 PRINT #2,Y
452 PRINT #2,AMP

500 NEXT TAU

600 GOTO 300

9000 PRINT #2,-999\PRINT #2,-999\PRINT #2,-999\PRINT #2,-999
9001 REM              LARGE NEGATIVE VALUES MARK THE END OF THE DATA FILE.


9999 END
```

APPENDIX C

COMPUTER PROGRAMS REFERENCED IN CHAPTER 7

Forward.bas

```
10 REM      CALCULATES THE LOCI OF SECTIONS THROUGH THE CAUSTIC SURFACE
11 REM      PRODUCED BY REFLECTION FROM A GIVEN SURFACE AT A VARIOUS
12 REM      HEIGHTS

14 REM      WRITTEN IN VAX BASIC.


16 REM      VARIABLES USED:

18 REM      Z:      HEIGHT OF THE X-Y PLANE BEING SEARCHED.
19 REM      X,Y:    POSITION IN CARTESIAN COORDINATES.
20 REM      R,THETA:        POSITION IN RADIAL COORDINATES.
21 REM      STP:    SEPARATION BETWEEN TEST VALUES OF R.
22 REM      TSTP:   SEPARATION BETWEEN TEST VALUES OF THETA.
23 REM      CX,CY:  COORDINATES OF THE CENTER POINT OF RADIAL SEARCH.
24 REM      NM:     LABELS THE WHICH ZERO OF THE JACOBIAN IS BEING SOUGHT.
25 REM      S:      FUNCTION REPRESENTING THE SURFACE.
26 REM      SX:     DIFFERENTIAL OF S WITH RESPECT TO X.
27 REM      SXY:    DIFFERENTIAL OF SX WITH RESPECT TO Y.
28 REM      U,V:    POINT AT WHICH A RAY REFLECTED FROM (X,Y) CROSSES THE
29 REM              PLANE, Z.
30 REM      J:      THE JACOBIAN OF THE MAP, U(X,Y), V(X,Y).



35 CX=-.001\CY=-.001
37  STP=.000004\TSTP=1*PI/180

40 READ F$,Z,NM\REM         OBTAINS THE NAME OF THE OUTPUT FILE, THE HEIGHT OF
41 REM      THE PLANE OF OBSERVATION AND THE ZERO TO BE FOUND FROM DATA
42 REM      STORED WITHIN THE PROGRAM.

50 IF F$="STOP" THEN 9999\REM                   END OF PROGRAM.
55 OPEN F$ FOR OUTPUT AS #1


100 REM     SEARCH OUTWARD FROM (CX,CY) FOR ZEROS IN THE JACOBIAN.

105 THETA=TSTP\CNT=1
110 R=STP\REM PRINT THETA*180/PI
120 X=CX+R*COS(THETA)\Y=CY+R*SIN(THETA)
130 GOSUB 5000\PS=SGN(J)
140 R=R+STP
150 X=CX+R*COS(THETA)\Y=CY+R*SIN(THETA)
160 IF X>.1 OR X<-.1 THEN 240\REM       SETS LIMIT TO SIZE OF SURFACE.
```

```
170 IF Y>.1 OR Y<-.1 THEN 240
200 GOSUB 5000
210 IF SGN(J)=PS THEN 140
230 IF CNT=NM THEN GOSUB 500\ELSE CNT=CNT+1\PS=PS*-1\GOTO 140
240 CNT=1\THETA=THETA+TSTP\IF THETA>2*PI THEN CLOSE #1\GOTO 40
250 GOTO 110


500 REM        CALCULATES AND OUTPUTS (U,V)

510 U=X+(Z-S)*STT*CA
520 V=Y+(Z-S)*STT*SA
530 PRINT #1,U\PRINT #1,V

599 RETURN



5000 REM              GIVEN X,Y RETURNS J

5001 GOSUB 9000\REM     GETS VALUE OF THE SURFACE HEIGHT AND ITS
DIFFERENTIALS
5002 SS=SX*SX+SY*SY\RSS=SQR(SS)

5004 CA=-SX/RSS\REM          CA="COSINE ALPHA"
5005 SA=-SY/RSS\REM          SA="SINE ALPHA"
5006 STT=2*RSS/(SS+1)\REM  STT="SINE TWO THETA"


5010 XCA=-(SXX-SX*(SX*SXX+SY*SXY)/SS)/RSS\REM          XCA="D COS ALPHA BY D X"
5020 YCA=-(SXY-SX*(SX*SXY+SY*SYY)/SS)/RSS\REM          YCA="D COS ALPHA BY D Y"
5030 XSA=-(SXY-SY*(SX*SXX+SY*SXY)/SS)/RSS\REM          XSA="D SIN ALPHA BY D X"
5040 YSA=-(SYY-SY*(SX*SXY+SY*SYY)/SS)/RSS\REM          TSA="D SIN ALPHA BY D Y"

5050 XSTT=2*((SX*SXX+SY*SXY)/((SS+1)^2))*(((SS+1)/RSS)-2*RSS)
5060 YSTT=XSTT*(SX*SXY+SY*SYY)/(SX*SXX+SY*SXY)

5100 UX=1+(Z-S)*STT*XCA+(Z-S)*XSTT*CA-SX*STT*CA
5110 UY=(Z-S)*STT*YCA+(Z-S)*YSTT*CA-SY*STT*CA
5120 VY=1+(Z-S)*STT*YSA+(Z-S)*YSTT*SA-SY*STT*SA
5130 VX=(Z-S)*STT*XSA+(Z-S)*XSTT*SA-SX*STT*SA

5200 J=UX*VY-UY*VX

5999 RETURN



9000 REM              THE SURFACE FUNCTION AND ITS DIFFERENTIALS
9005 REM              AN ARBITARY CUBIC SURFACE.

9010 A=.000661\B=1000\C=10000\D=1000\E=1000\F=1000\G=1000\H=1000
9020 S=A*( H*X*X*X+ B*X*X*Y +C*X*Y*Y +D*Y*Y*Y +E*X*X +F*X*Y +G*Y*Y )
9030 SX=A*( 3*H*X*X+ 2*B*X*Y +C*Y*Y +2*E*X +F*Y )
```

```
9040 SY=A*( B*X*X+ 2*C*X*Y +3*D*Y*Y +F*X +2*G*Y )
9050 SXX=A*( 6*H*X+ 2*B*Y+ 2*E )
9060 SXY=A*( 2*B*X+ 2*C*Y +F )
9070 SYY=A*( 2*C*X+ 6*D*Y +2*G )
9099 RETURN

9200 DATA "SM9999N1.DAT",-9.999,1
9220 DATA "SP9999N1.DAT",9.999,1
9230 DATA "SM9979N1.DAT",-9.979,1
9235 DATA "SP9979N1.DAT",9.979,1


9240 DATA "SM3200N1.DAT",-3.200,1
9260 DATA "SP3200N1.DAT",3.200,1
9270 DATA "SM3220N1.DAT",-3.220,1
9275 DATA "SP3220N1.DAT",3.220,1

9280 DATA "SM1000N1.DAT",-1,1
9300 DATA "SP1000N1.DAT",1,1
9310 DATA "SM1010N1.DAT",-1.01,1
9320 DATA "SP1010N1.DAT",1.01,1


9360 DATA "SM5657N1.DAT",-5.657,1
9380 DATA "SP5657N1.DAT",5.657,1
9390 DATA "SM5667N1.DAT",-5.667,1
9395 DATA "SP5667N1.DAT",5.667,1

9400 DATA "SM1789N1.DAT",-1.789,1
9420 DATA "SP1789N1.DAT",1.789,1
9430 DATA "SM1799N1.DAT",-1.799,1
9435 DATA "SP1799N1.DAT",1.799,1

9440 DATA "SM566N1.DAT",-.566,1
9460 DATA "SP566N1.DAT",.566,1
9470 DATA "SP566N2.DAT",.566,2
9475 DATA "SM576N1.DAT",-.576,1
9477 DATA "SP576N1.DAT",.576,1
9478 DATA "SP576N2.DAT",.576,2


9480 DATA "SP179N1.DAT",.179,1
9495 DATA "SP170N1.DAT",.170,1


9540 DATA "SP4255N1.DAT",4.255,1
9550 DATA "SP4235N1.DAT",4.235,1

9600 DATA "SM2393N1.DAT",-2.393,1
9610 DATA "SM2373N1.DAT",-2.373,1

9640 DATA "SM1334N1.DAT",-1.334,1
9650 DATA "SM1354N1.DAT",-1.534,1

9660 DATA "SP752N1.DAT",.752,1
```

```
9690 DATA "SM752N1.DAT",-.752,1
9700 DATA "SP762N1.DAT",.762,1
9720 DATA "SM762N1.DAT",-.762,1


9740 DATA "SP239N1.DAT",.239,1
9750 DATA "SP239N2.DAT",.239,2
9760 DATA "SP249N1.DAT",.249,1
9770 DATA "SP249N2.DAT",.249,2


9900 DATA "STOP",1,1


9999 END
```

Inverse.bas

```
10 REM      CALCULATES THE SLOPE OF A SURFACE GIVEN THE LOCI OF THE RAYS
11 REM      REFLECTED BY IT AND COMPARES RESULT TO THAT EXPECTED.

13 REM      WRITTEN IN VAX BASIC.


40 REM              VARIABLES USED.

43 REM      (X1,Y1,Z1), (X2,Y2,Z2):      COORDINATES OF TWO POINTS ON A RAY.
44 REM      BEST:  GOODNESS OF FIT TO DOUBLE TANGENCY IN THE PREVIOUS
                   PROGRAM.
45 REM      (XH,YH):     POINT AT WHICH RAY CROSSED THE PLANE, Z=0.
46 REM      THETA:       ANGLE BETWEEN A RAY AND THE Z-DIRECTION.
47 REM      ALPHA:       ANGLE BETWEEN THE PROJECTION OF THE RAY ONTO THE
48 REM                   PLANE Z=0 AND THE X-DIRECTION


100 OPEN "RAYS.DAT" FOR INPUT AS #1\REM          READ COORDINATES OF RAYS.
110 OPEN "ERRORS.DAT" FOR OUTPUT AS #2\REM       WRITE ACCURACY OF THE
111 REM                                          INVERSION PROCEEDURE.


190 REM      THE COORDINATES OF TWO POINTS ON THE RAY AND A MEASURE OF THE
191 REM      GOODNESS OF FIT IN THE PREVIOUS CALCULATION ARE GIVEN.

200 INPUT #1,X1\INPUT #1,Y1\INPUT #1,Z1\INPUT #1,X2\INPUT #1,Y2
201 INPUT #1,Z2\INPUT #1,BEST


300 REM      FIND (XH,YH) AT WHICH RAY CROSSES PLANE Z=0.
310 XH=X1+(X2-X1)*Z1/(Z1-Z2)
```

```
320  YH=Y1+(Y2-Y1)*Z1/(Z1-Z2)

322 IF XH>1 OR XH<-1 THEN 200\REM   RAY DISCARDED IF POINT OF INTERSECTION
324 IF YH>1 OR YH<-1 THEN 200\REM  OUTSIDE PRESET AREA.


1000 REM                COMPARE ANGLES
1010  THETA=ABS(Z1-Z2)/(SQR((X1-X2)^2+(Y1-Y2)^2))\THETA=1/THETA
1020 THETA=ATN(THETA)\THETA=THETA*180/PI
1040   ALPHA=ATN((Y1-Y2)/(X1-X2))\ALPHA=ALPHA*180/PI
1050 IF ALPHA<0 THEN ALPHA=ALPHA+180
1060 IF Y2>Y1 AND Z1>Z2 THEN ALPHA=ALPHA+180
1070 IF Y1>Y2 AND Z2>Z1 THEN ALPHA=ALPHA+180

1093 IF ALPHA>270 AND AEX<90 THEN AEX=AEX+360\GOTO 1100
1096 IF ALPHA<90 AND AEX>270 THEN AEX=AEX-360

1100  DELTA=SQR((THETA-TT)^2+((ALPHA-AEX)*SIN(TT))^2)
1150  PRINT #2,BEST\PRINT #2,DELTA
1155 IF BEST<.01 AND DELTA>3 THEN PRINT BEST,DELTA,THETA-TT,ALPHA-AEX,TT

1200 GOTO 200



9000 REM                SURFACE FUNCTION

9010  A=5\B=2.5\C=3\D=4
9020  S=.1*EXP(-A*X*X+B*X-C*Y*Y+D*Y*Y*Y)
9030  SX=S*(-2*A*X+B)
9040   SY=S*(-2*C*Y+3*D*Y*Y)

9050 SS=SX*SX+SY*SY\RSS=SQR(SS)
9060  STT=2*RSS/(SS+1)
9070  TT=ATN(STT/(SQR(1-STT*STT)))\TT=TT*180/PI

9079 IF SX=0 THEN AEX=89.9999\GOTO 9100
9080  AEX=ATN(SY/SX)\REM     ALPHA EXACT
9090  AEX=AEX*180/PI
9100 IF AEX<0 THEN AEX=AEX+180
9110 IF SY>0 THEN AEX=AEX+180

9300 RETURN



9999 END
```

Tangent.bas

```
2 REM       SEARCHES FOR COMMON TANGENTS BETWEEN SECTIONS OF THE CAUSTIC
3 REM       SURFACE TAKEN AT DIFFERENT HEIGHTS.

4 REM       WRITTEN IN VAX BASIC.


20 REM              VARIABLES USED:

25 REM      X(N,M), (Y(N,M):    THE (X,Y)-COORDINATES OF THE Mth POINT
26 REM                          OF THE Nth SECTION THROUGH THE CAUSTIC.
27 REM      Z(N):   THE Z-COORDINATE OF ALL POINTS OF THE Nth SECTION
28 REM              THROUGH THE CAUSTIC.
29 REM      NM(N):          THE NUMBER OF POINTS IN THE Nth SECTION.
30 REM      NN(N):          THE NUMBER OF BRANCHES TO THE Nth SECTION.
31 REM      FIRST, SECOND, THIRD, FOURTH:       THE N-VALUE FOR THE FIRST,
32 REM                                          SECOND, THIRD AND FOURTH
33 REM                                          LEVEL BEING CONSIDERED.
34 REM      CNT:    THE TOTAL NUMBER OF SECTIONS BEING CONSIDERED.
35 REM      F:      THE M-VALUE OF THE POINT BEING CONSIDERED ON THE FIRST
36 REM              LEVEL.
37 REM      S:      THE M-VALUE OF THE POINT BEING CONSIDERED ON THE SECOND
38 REM              LEVEL.
39 REM      T:      THE M-VALUE OF THE POINT BEING CONSIDERED ON THE THIRD
40 REM              LEVEL.
41 REM      W:      THE M-VALUE OF THE POINT BEING CONSIDERED ON THE FORTH
42 REM              LEVEL.


90 DIM X(50,500), Y(50,500),Z(50),NM(50),NN(50)
95 DIM BEST(20),FBEST(20),TBEST(20)
97 NBEST=4

100 OPEN "RAYS.DAT" FOR OUTPUT AS #2

1000 REM            READ DATA FILES CONTAINING CROSS SECTIONS OF THE CAUSTIC
1001 REM            SURFACE INTO ARRAYS.

1035 N=N+1\Q=0
1040 READ F$,Z,NN
1045 IF F$="STOP" THEN 2000
1047 Z(N)=Z\NN(N)=NN\CNT=CNT+1

1050 OPEN F$ FOR INPUT AS #1
1057 Q=Q+1

1060 INPUT #1,X(N,Q)\INPUT #1,Y(N,Q)
1070 ON ERROR GOTO 1300\REM     ERROR TRAP DETECTS END OF FILE.
1080 GOTO 1057
```

```
1300 CLOSE #1\NM(N)=Q\RESUME 1035

2000 REM          FIND COMMON TANGENT BETWEEN LOCI "FIRST" AND "SECOND"
2001 REM          WHEN PROJECTED ONTO A COMMON PLANE.

2002 ON ERROR GOTO 0\REM          END OF ERROR TRAP.

2007 FOR FIRST=1 TO CNT-2
2009 FOR SECOND=FIRST+1 TO CNT-1
2011 IF ABS(Z(FIRST)-Z(SECOND))>.025 THEN 4010\REM      TASK ONLY PERFORMED ON
2012 REM                                                SECTIONS OF SIMILAR
2013 REM                                                HEIGHT.

2014 IF NN(FIRST)<>NN(SECOND) THEN 4010\REM     DATA SETS, "FIRST" AND "SECOND"
2015 REM                                        ARISE FROM THE SAME BRANCH OF THE
2016 REM                                        SOLUTION FOUND BY "FORWARD.BAS".

2017 FOR THIRD=1 TO CNT-1
2018 IF ABS(Z(THIRD)-Z(FIRST))<.025 THEN 4000\REM       THIRD LEVEL MUST BE A
2019 IF THIRD=FIRST OR THIRD=SECOND THEN 4000\REM       SIGNIFICANT DISTANCE
2020 REM                                                FROM THE FIRST.

2021 FOR FOURTH=THIRD+1 TO CNT
2022 IF ABS(Z(THIRD)-Z(FOURTH))>.025 THEN 3990
2023 IF FOURTH=FIRST OR FOURTH=SECOND OR NN(THIRD)<>NN(FOURTH) THEN 3990


2024 FOR NNN=1 TO NBEST+1\BEST(NNN)=10000000\FBEST(NNN)=-1\TBEST(NNN)=-
1\NEXT NNN
2025 FOR F=1 TO NM(FIRST)-1\REM   FIND HORIZONTAL TANGENT TO THE SECTION
2026 REM                          AT THE FIRST LEVEL.

2027 IF (X(FIRST,F)-X(FIRST,F+1))=0 THEN FM=100000000\GOTO 2032
2030  FM=(Y(FIRST,F)-Y(FIRST,F+1))/(X(FIRST,F)-X(FIRST,F+1))
2032  FC=Y(FIRST,F)-FM*X(FIRST,F)
2100  DIST=100000\S=1

2109 IF (X(SECOND,S)-X(SECOND,S+1))=0 THEN SM=100000000\GOTO 2120
2110 SM=(Y(SECOND,S)-Y(SECOND,S+1))/(X(SECOND,S)-X(SECOND,S+1))
2120  SIGN=SGN(SM-FM)
2200 FOR S=2 TO NM(SECOND)-1\REM          FIND CLOSEST POINT ON THE SECOND
LEVEL
2201 REM                                  TO THAT ON THE FIRST AT WHICH THE
2202 REM                                  TANGENT IS PARALLEL TO THAT TAKEN
AT
2203 REM                                  THE FIRST LEVEL.

2209 IF (X(SECOND,S)-X(SECOND,S+1))=0 THEN SM=100000000\GOTO 2220
2210 SM=(Y(SECOND,S)-Y(SECOND,S+1))/(X(SECOND,S)-X(SECOND,S+1))

2220 IF SGN(SM-FM)=SIGN THEN 2299


2230 SIGN=-SIGN\IF ABS(SM-FM)>ABS(FM*.2) THEN 2299
```

```
2237 D=(Y(SECOND,S)-Y(FIRST,F))^2+(X(SECOND,S)-X(FIRST,F))^2
2240 IF D<DIST THEN DIST=D\TGENT=S

2299 NEXT S\REM PRINT "TGENT=";TGENT
2300 SC=Y(SECOND,TGENT)-FM*X(SECOND,TGENT)
2310 ZSLOPE=(FC-SC)/(Z(FIRST)-Z(SECOND))
2314 ZINT=FC-ZSLOPE*Z(FIRST)
2320 SLOPE=FM\REM PRINT "ZSLOPE=";ZSLOPE;"FIRST INTERCEPT";FC;"SECOND";SC


3000 REM            FIND POINT OF TANGENCY WITH THE SECTION AT THE THIRD
3001 REM            LEVEL.

3010 MM=FM\CC=ZSLOPE*Z(THIRD)+ZINT\REM PRINT F;"MM=";MM,"CC=";CC
3050 DISTO=100000\DOWN=1

3100 FOR T=1 TO NM(THIRD)-1

3140  XN=(X(THIRD,T)+MM*Y(THIRD,T)-MM*CC)/(1+MM*MM)
3150 YN=MM*XN+CC
3160  DIST=SQR((XN-X(THIRD,W))^2+(YN-Y(THIRD,W))^2)
3170 IF DIST<DISTO AND DOWN=-1 THEN DOWN=1\GOSUB 6000
3180 IF DIST>DISTO AND DOWN=1 THEN DOWN=-1\GOSUB 6000


3300 DISTO=DIST
3399 NEXT T
3500 NEXT F

3510 IF FBEST(1)<0 THEN 3990

3515 REM            RECORD THE COORDINATES COORESPONDING TO THE POINTS MOST
3516 REM            LIKELY TO REPRESENT RAYS.

3520 FOR NNN=1 TO NBEST
3530 IF FBEST(NNN)<0 THEN NNN=NBEST+1\GOTO 3699

3650  PRINT  #2,X(FIRST,FBEST(NNN))
3653  PRINT  #2,Y(FIRST,FBEST(NNN))
3656  PRINT  #2,Z(FIRST)

3660  PRINT  #2,X(THIRD,TBEST(NNN))
3663  PRINT  #2,Y(THIRD,TBEST(NNN))
3666  PRINT  #2,Z(THIRD)
3670  PRINT  #2,BEST(NNN)

3699 NEXT NNN

3990 NEXT FOURTH
4000 NEXT THIRD
4010 NEXT SECOND
4020 NEXT FIRST
4050 GOTO 9999
```

```
6000 REM                FIND DISTANCE BETWEEN TANGENT PLANE OF LOWER SECTION
6001 REM                THROUGH THE CAUSTIC AND UPPER SECTION.

6010 IF DIST>BEST(NBEST)*2 THEN RETURN

6027 IF (X (THIRD,T)-X(THIRD,T+1))=0 THEN TM=100000000\GOTO 6032
6030  TM=(Y(THIRD,T)-Y(THIRD,T+1))/(X(THIRD,T)-X(THIRD,T+1))
6032 TC=Y(THIRD,T)-TM*X(THIRD,T)
6100  DIST2=100000\W=1

6109 IF (X(FOURTH,W)-X(FOURTH,W+1))=0 THEN WM=100000000\GOTO 6120
6110  WM=(Y(FOURTH,W)-Y(FOURTH,W+1))/(X(FOURTH,W)-X(FOURTH,W+1))
6120 SIGN=SGN(WM-TM)
6200 FOR W=2 TO NM(FOURTH)-1

6209 IF (X(FOURTH,W)-X(FOURTH,W+1))=0 THEN WM=100000000\GOTO 6220
6210  WM=(Y(FOURTH,W)-Y(FOURTH,W+1))/(X(FOURTH,W)-X(FOURTH,W+1))

6220 IF SGN(WM-TM)=SIGN THEN 6299


6230 SIGN=-SIGN\IF ABS(WM-TM)>ABS(TM*.2) THEN 6299
6237 D=(Y(FOURTH,W)-Y(THIRD,T))^2+(X(FOURTH,W)-X(FIRST,T))^2
6240 IF D<DIST2 THEN DIST2=D\TGENT=W

6299 NEXT W
6300 WC=Y(FOURTH,TGENT)-TM*X(FOURTH,TGENT)
6310  ZSLOPE1=(TC-WC)/(Z(THIRD)-Z(FOURTH))
6314 ZINT1=TC-ZSLOPE1*Z(THIRD)
6320 SLOPE=TM\REM PRINT "ZSLOPE=";ZSLOPE;"FIRST INTERCEPT";FC;"SECOND";SC

6350 MBACK=TM\CBACK=ZSLOPE1*Z(FIRST)+ZINT1
6360  XBACK=(X(FIRST,F)+MBACK*Y(FIRST,F)-MBACK*CBACK)/(1+MBACK*MBACK)
6370 YBACK=MBACK*XBACK+CBACK
6380  D=SQR((XBACK-X(FIRST,F))^2+(YBACK-Y(FIRST,F))^2)
6390 GOOD=.5*(D+DIST)
6410 IF BEST(NBEST)<GOOD THEN 6500
6420 BEST(NBEST)=GOOD\FBEST(NBEST)=F\TBEST(NBEST)=T\GOSUB 7000

6500 RETURN


7000 REM                SORT ARRAY, BEST USING A "BUBBLE SORT" METHOD.

7005 OK=1
7010 FOR PP=1 TO NBEST-1

7020 IF BEST(PP)=<BEST(PP+1) THEN 7100
7025 OK=0
7030 QQQ=BEST(PP)\BEST(PP)=BEST(PP+1)\BEST(PP+1)=QQQ
7040 QQQ=FBEST(PP)\FBEST(PP)=FBEST(PP+1)\FBEST(PP+1)=QQQ
7050 QQQ=TBEST(PP)\TBEST(PP)=TBEST(PP+1)\TBEST(PP+1)=QQQ

7100 NEXT PP
```

```
7110 IF OK=O THEN OK=1 \GOTO 7010

7199 RETURN


9200 DATA "SM9999N1.DAT",-9.999,1\REM
9201 REM
9220 DATA "SP9999N1.DAT",9.999,1\REM
9230 DATA "SM9979N1.DAT",-9.979,1\REM
9235 DATA "SP9979N1.DAT",9.979,1

9240 DATA "SM3200N1.DAT",-3.200,1
9260 DATA "SP3200N1.DAT",3.200,1
9270 DATA "SM3220N1.DAT",-3.220,1
9275 DATA "SP3220N1.DAT",3.220,1

9280 DATA "SM1000N1.DAT",-1,1
9300 DATA "SP1000N1.DAT",1,1
9310 DATA "SM1010N1.DAT",-1.01,1
9320 DATA "SP1010N1.DAT",1.01,1

9360 DATA "SM5657N1.DAT",-5.657,1
9380 DATA "SP5657N1.DAT",5.657,1
9390 DATA "SM5667N1.DAT",-5.667,1
9395 DATA "SP5667N1.DAT",5.667,1

9400 DATA "SM1789N1.DAT",-1.789,1
9420 DATA "SP1789N1.DAT",1.789,1
9430 DATA "SM1799N1.DAT",-1.799,1
9435 DATA "SP1799N1.DAT",1.799,1

9440 DATA "SM566N1.DAT",-.566,1
9460 DATA "SP566N1.DAT",.566,1
9470 DATA "SP566N2.DAT",.566,2
9475 DATA "SM576N1.DAT",-.576,1
9477 DATA "SP576N1.DAT",.576,1
9478 DATA "SP576N2.DAT",.576,2

9480 DATA "SP179N1.DAT",.179,1
9495 DATA "SP170N1.DAT",.170,1

9540 DATA "SP4255N1.DAT",4.255,1
9550 DATA "SP4235N1.DAT",4.235,1

9600 DATA "SM2393N1.DAT",-2.393,1
9610 DATA "SM2373N1.DAT",-2.373,1

9640 DATA "SM1334.DAT",-1.334,1
9650 DATA "SM1354.DAT",-1.534,1

9660 DATA "SP752N1.DAT",.752,1
9690 DATA "SM752N1.DAT",-.752,1
9700 DATA "SP762N1.DAT",.762,1
9720 DATA "SM762N1.DAT",-7.62,1
```

CODE NAMES OF THE DATA FILES
CONTAINING
SECTIONS THROUGH THE CAUSTIC SURFACE
AT VARIOUS HEIGHTS.

```
9740 DATA "SP239N1.DAT",.239,1
9750 DATA "SP239N2.DAT",.239,2
9760 DATA "SP249N1.DAT",.249,1
9770 DATA "SP249N2.DAT",.249,2


9900 DATA "STOP",1,1


9999 END
```

VITA

James Robert Brewster was born in May 1965 in Enfield, Middlesex, Great Britain. He was brought up in Corby, Northamptonshire, an industrial town of 50,000 people on the East Midlands region of England.

He received his secondary education at Southwood Comprehensive School, Corby, obtaining advanced level certificates of education in mathematics, physics and chemistry and also passed the special examination in physics.

He attended college at the University of Bristol, England and in 1986 graduated with a Bachelors degree in physics. The author has been in Tennessee since June 1987, was awarded a masters degree in Materials Science and has maintained a grade point average of 3.89.

In March 1991 James married Lajwanti S. Khemlani of Poona, India, a biochemist and University of Tennessee alumnus.

The author's hobbies include golf, guitar playing, running and increasing his general knowledge of science and science related issues.